

# Smoothed particle hydrodynamics (SPH) and its applications in geomechanics: From solid fracture to granular behaviour and multiphase flows in porous media



Ha H. Bui<sup>a,\*</sup>, Giang D. Nguyen<sup>b</sup>

<sup>a</sup> Monash Computational Geomechanics (MCG) Laboratory, Department of Civil Engineering, Monash University, Melbourne, VIC 3800, Australia

<sup>b</sup> School of Civil, Environmental & Mining Engineering, University of Adelaide, Adelaide, SA 5005, Australia

## ARTICLE INFO

### Keywords:

Smoothed particle hydrodynamics  
Particle methods  
Geomechanics  
Two-scale  
Post-failure  
Coupled deformation  
Porous media  
Seepage flows

## ABSTRACT

We present the fundamental concepts of SPH with particular emphasis on its state-of-the-art applications in geomechanics and geotechnical engineering. In the first part of the paper, we focus on establishing fundamental SPH equations and discussing how they are used to solve partial differential equations (PDEs) in geomechanics. Through this process, we expect to provide readers with a better understanding of SPH formulations to avoid misuse or misinterpretation of its capacity and limitation. Discussions on several outstanding issues and recommendations for further developments are also be presented. Of particular interest through this revisit of the key SPH concepts is a new and robust SPH approximation formulation for the Laplacian, which involves the second-order derivatives of a field quantity. This new formulation is proven to outperform existing SPH formulations and achieve high accuracy. The second part of the paper focuses on demonstrating the applications of SPH in the fields of geomechanics and geotechnical engineering through various examples, ranging from the most fundamental to more complex applications involving multi-phase flows. We hope that this paper will become a useful resource to provide readers with a better understanding of SPH and its potential in solving complex problems in geomechanics and geotechnical engineering.

## 1. Introduction

Robust numerical methods for solving complex problems involving multi-phase multi-physical processes are crucial and also an increasing trend in recent years in the field of computational geomechanics. The key reason is because most popular existing computational tools for field scale-applications are still heavily relied on the conventional finite element method (FEM), which is a continuum mesh-based numerical method and is well-known for suffering from mesh-distortion issues associated with large deformation of geomaterials. There exist advanced solutions to address this issue (Nazem et al., 2009, Yu et al., 2008, Cuomo et al., 2013, Moresi et al., 2003, Qiu et al., 2011), but these approaches are often complex and thus may be not appealing for field-scale applications. Alternative to mesh-based FEMs is continuum point-based methods, which offer great capacity for solving field-scale applications involving large-deformation and post-failure of geomaterials. SPH is perhaps the oldest continuum point-based method that is completely mesh-free and requires no background mesh to solve

partial differential equations (PDEs), among several existing point-based methods (Koshizuka and Oka, 1996, Liu et al., 2005, Silling, 2000), which share the same features and have been used to solve geomechanics problems (Chen et al., 2020, Yang et al., 2020b, Zhu and Zhao, 2021). The SPH method was originally developed for astrophysics applications (Gingold and Monaghan, 1977, Lucy, 1977), but soon becoming a popular method for various engineering applications (Bui et al., 2007, Bui and Nguyen, 2017, Wang and Chan, 2014, Pastor et al., 2009, Bui and Fukagawa, 2013, Xu and Deng, 2016, Nguyen et al., 2015, Fávero Neto and Borja, 2018, Peng et al., 2015, Zhao et al., 2017, Libersky and Petschek, 1991, Chen et al., 1999, Douillet-Grellier et al., 2016, Blanc and Pastor, 2012, Blanc and Pastor, 2013, Hu and Adams, 2006, Hu and Adams, 2007, Nguyen et al., 2013, Hiraoka et al., 2013, Bui et al., 2009, Bui et al., 2008a, Bui et al., 2011, Bui et al., 2014, Tran et al., 2019, Wang et al., 2019). The fundamental difference between SPH and other point-based FEM methods, such as Material Point Method – MPM (Sulsky et al., 1994, Soga et al., 2016, Wang et al., 2016b, Beuth et al., 2011) or Particle Finite Element Method – PFEM (Monforte et al.,

\* Corresponding author.

E-mail address: [ha.bui@monash.edu](mailto:ha.bui@monash.edu) (H.H. Bui).

2017, Onate et al., 2008, Zhang et al., 2013) is that SPH directly solves the governing PDEs by approximation of their strong forms, while the other point-based FEM methods solve the weak forms of PDEs. Since there is no need to go through the weak form formula, it is more straightforward to incorporate the SPH approximation of a new PDE describing a new physical phenomenon in an existing SPH framework. Furthermore, owing to the truly mesh-free nature of SPH, the method offers the great capability to address several challenging problems involving large deformation and post-failure of geomaterials in the geomechanics discipline. Nevertheless, there exist common misinterpretations in the literature on the capacity and limitation of SPH, which simply refer to SPH as a numerical method that is suffered from numerical instability and inaccuracy, without acknowledging its true capacity and potential. Interestingly, most of these interpretations came from experts in mesh-based methods or from misuses of fundamental SPH kernel approximation (Swegle et al., 1995). In this paper, we attempt to provide readers with more transparent information and a better understanding of SPH, along with its true capacity and limitation. To achieve this goal, we will first present a comprehensive review of the fundamental concepts of SPH and discuss various outstanding issues associated with the misuse or misinterpretation of SPH. Through this process, we propose a new SPH formulation to approximate the Laplacian, which involves second-order derivatives of a field quantity. We demonstrate that this new formulation outperforms any existing SPH formula for the Laplacian and is less sensitive to the random particle configuration or particles disordered. We will then focus our discussions on a range of SPH applications in geomechanics, highlighting its capability as well as limitations in solving such challenging problems. Some of the SPH applications presented in this paper are for the first time within the context of SPH. We acknowledge that there exist several excellent SPH reviews in the literature (Price, 2012, Monaghan, 2012, Monaghan, 2005b, Liu and Liu, 2010), but to the best of our knowledge, there is no comprehensive SPH review dedicated to geomechanics applications. We also note that this paper does not aim to provide a comprehensive summary of what has been done or achieved with SPH in the literature. Instead, we re-address the fundamental issues of SPH based on our own experience in working with this method and its applications for many years, with a particular focus on advancing its applications in tackling challenging problems in geomechanics. The SPH applications presented in this paper, though they might not cover all SPH applications in geomechanics, are believed to be among the most state-of-the-art SPH applications in geomechanics and geotechnical engineering. We also note that a part of this review was distributed as a lecture note to participants attending the ALERT GEOMATERIALS Doctoral School 2020 on Point-based Method in Geomechanics, for which Prof Ha H. Bui was an invited lecturer.

## 2. The fundamentals of SPH

There are several different ways to approach the fundamental of SPH in the literature, many of which simply refer to the method as an interpolation procedure, which can be used to approximate a field quantity or its spatial derivatives. In our view, SPH is more than a numerical method since the foundation of SPH as well as its governing equations can be naturally derived from considerations of several fundamental physical processes (Monaghan and Price, 2001), which makes the method more appealing for solving physical problems.

### 2.1. Basic SPH formulations from fundamental physics

Let us first establish the basic SPH formulation. Consider a continuum field represented by a collection of point masses (hereafter referring to particles), each of which occupies a certain volume of the continuum field and carries the corresponding mass of the occupied volume (Fig. 1). One of the simplest but interesting questions that would arise from this consideration is: *How do we calculate the continuous density*

*field at a particular point from this collection of particles?*

Perhaps, the most common answer to the above question is to consider a local sampling volume of mass distribution ( $V_{sp}$ ), assuming spherical volume in 3D and circular area in 2D as shown in Fig. 1a. The continuous density field at the central particle of the sampling volume can be then computed by taking the total mass of all particles located within the sampling volume and dividing by the sampling volume:

$$\rho(\mathbf{x}_i) = \frac{1}{V_{sp}} \sum_{j=1}^N m_j \quad (1)$$

where  $\rho(\mathbf{x}_i)$  is the continuous density field at the central particle of the sampling volume  $\mathbf{x}_i$ ;  $N$  is the total number of “neighbouring” particles located within the sampling volume  $V_{sp}$ ;  $m_j$  is the mass of a particle  $j$  located within the sampling volume.

The immediate issue that arises from this approach is that the estimated continuous density field would be significantly affected by the distribution of particles, i.e. clustered/spare regions of particle mass distribution. Although this issue can be fixed by adjusting the sampling volume ( $V_{sp}$ ) following a certain criterion, a small adjustment/variation of the sampling volume would significantly affect the calculation result (e.g. it can either include or exclude a particle mass from the calculation). Accordingly, the estimated continuous density field would be highly sensitive to the sampling volume and thus leading to a very noisy density field estimation. A simple solution<sup>1</sup> to improve the estimated density field is to adopt a weighted average approach (Fig. 1b), in which particles close to the centre of the sampling volume participate more in the density estimation, while those located away from the centre have less contribution. This idea can be mathematically formulated using the following equation (Monaghan, 2012, Monaghan, 2005a, Monaghan, 2005b):

$$\rho(\mathbf{x}_i) = \sum_{j=1}^N m_j W(\mathbf{x}_i - \mathbf{x}_j, h) \quad (2)$$

where  $W(\mathbf{x}_i - \mathbf{x}_j, h)$  is a weighting function, which has a dimension of inverse volume ( $V_{sp}^{-1}$ ) and is dependent on the particle distance ( $\mathbf{x}_i - \mathbf{x}_j$ ) and a scalar parameter  $h$  (to be defined later). The readers could immediately see that the accuracy of the above density estimation rests on the choice of the weighting function  $W(\mathbf{x}_i - \mathbf{x}_j, h)$ . For instance, to address the issue associated with the use of Equation (1), the weighting function  $W(\mathbf{x}_i - \mathbf{x}_j, h)$  needs to have the following properties:

1. It should be defined in such a way that its magnitude reaches a peak value at the centre of the sampling volume and gradually reduces and asymptotically approaches zero as the distance from a particle mass to the centre of the sampling volume increases (i.e. shading area in Fig. 1b). This can be achieved by defining the weighting function  $W$  as a function of particle spacing ( $\mathbf{x}_i - \mathbf{x}_j$ ) and a scalar parameter ( $h$ ) defining the rate of falling-off of  $W$ .
2. It should be positive and symmetric with respect to the particle distance. This guarantees particles with the same distance from the centre of the sampling volume will have equal contributions to the density estimation.
3. The conservation of total mass  $\int \rho dV = \sum_{j=1}^N m_j$  requires the following condition of the weighting function:

$$\int W(\mathbf{x}_i - \mathbf{x}_j, h) dV = 1 \quad (3)$$

There exists a number of weighting functions in the literature that

<sup>1</sup> There exists alternative methods (such as mesh-based methods) which can be used to estimate the continuous density field from the collection of point masses. These are however beyond the scope of this paper.

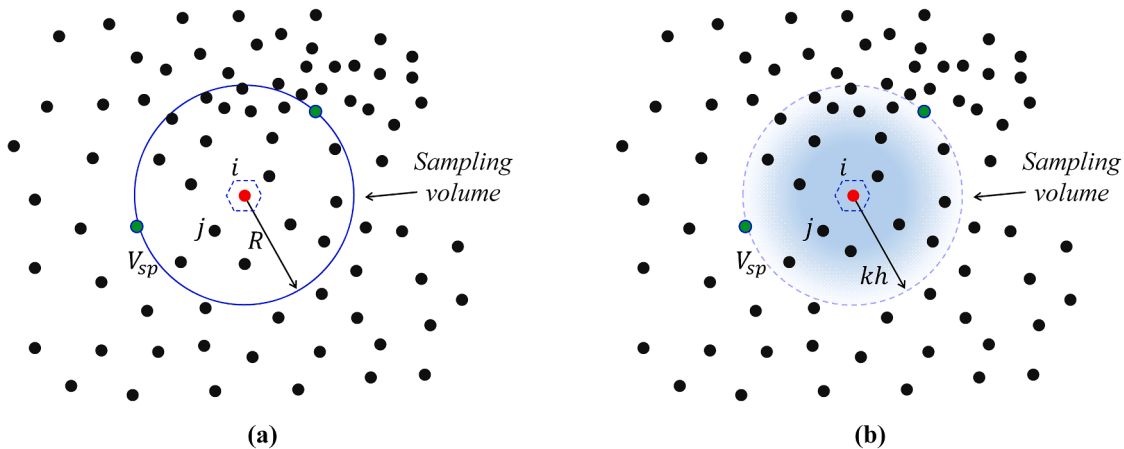


**Fig. 1.** Different approaches used to compute the continuous density field at a particular particle in a continuum field represented by a collection of point masses.

satisfies the above requirements. We will come back to this topic later with an in-depth discussion on the selection of an appropriate weighting function. Finally, if Equation (2) is rewritten as:

$$\rho(\mathbf{x}_i) = \sum_{j=1}^N \frac{m_j}{\rho_j} \rho(\mathbf{x}_j) W(\mathbf{x}_i - \mathbf{x}_j, h) \quad (4)$$

One can immediately see that the above equation can be generalised in the following form for an arbitrary function  $f(\mathbf{x}_i)$ :

$$f(\mathbf{x}_i) = \sum_{j=1}^N V_j f(\mathbf{x}_j) W(\mathbf{x}_i - \mathbf{x}_j, h) \quad (5)$$

Here, we have replaced  $\rho \equiv f$  and  $m_j/\rho_j \equiv V_j$ . Equation (5) is the basic SPH formula commonly reported in the literature. It forms the basis of all existing SPH formalisms. The readers could immediately see that, by choosing  $f \equiv \rho$ , Equation (5) will return to Equation (2) for the SPH density approximation. Alternatively, if we choose  $f$  to be a random field variable, such as temperature  $f \equiv T$ , Equation (5) can be used to estimate the temperature at the central of the sampling volume as follows:

$$T(\mathbf{x}_i) = \sum_{j=1}^N V_j T(\mathbf{x}_j) W(\mathbf{x}_i - \mathbf{x}_j, h) \quad (6)$$

This suggests that Equation (5) is a general SPH approximation equation, which can be used to estimate any field variable in the continuum space. Finally, to close this section, one would need to define the SPH approximation for the spatial derivative of a field function. This can be achieved by replacing the function  $f(\mathbf{x})$  in Equation (5) by its spatial derivative  $\partial f(\mathbf{x})/\partial \mathbf{x}$ , leading to:

$$\frac{\partial f(\mathbf{x}_i)}{\partial \mathbf{x}} = \sum_{j=1}^N \frac{m_j}{\rho_j} \frac{\partial f(\mathbf{x}_j)}{\partial \mathbf{x}_j} W(\mathbf{x}_i - \mathbf{x}_j, h) = \sum_{j=1}^N \frac{m_j}{\rho_j} \left[ \frac{\partial [f(\mathbf{x}_j) W(\mathbf{x}_i - \mathbf{x}_j, h)]}{\partial \mathbf{x}_j} - f(\mathbf{x}_j) \frac{\partial W(\mathbf{x}_i - \mathbf{x}_j, h)}{\partial \mathbf{x}_j} \right] \quad (7)$$

The first term on the right-hand side of Equation (7) is the summation approximation of the volume integral of the gradient of  $[f(\mathbf{x}_j) W(\mathbf{x}_i - \mathbf{x}_j, h)]$ , which can be rewritten as follows:

$$\sum_{j=1}^N \frac{m_j}{\rho_j} \frac{\partial [f(\mathbf{x}_j) W(\mathbf{x}_i - \mathbf{x}_j, h)]}{\partial \mathbf{x}_j} \approx \int_{\Omega} \frac{\partial [f(\mathbf{x}_j) W(\mathbf{x}_i - \mathbf{x}_j, h)]}{\partial \mathbf{x}_j} dV \quad (8)$$

where we have replaced  $dV$  with  $m_j/\rho_j$ . By applying the Gaussian the-

orem to convert the volume integral to the surface integral, we have:

$$\int_{\Omega} \frac{\partial [f(\mathbf{x}_j) W(\mathbf{x}_i - \mathbf{x}_j, h)]}{\partial \mathbf{x}_j} dV = \int_S f(\mathbf{x}_j) W(\mathbf{x}_i - \mathbf{x}_j, h) \vec{n} \cdot dS \quad (9)$$

where  $\vec{n}$  is the unit normal vector of the surface  $S$  of the volume  $\Omega$ . For a symmetric and positive weighting function, the above surface integral vanishes and thus, the SPH approximation formulation for the spatial derivative of a field function can be simplified to:

$$\frac{\partial f(\mathbf{x}_i)}{\partial \mathbf{x}_i} \approx \sum_{j=1}^N \frac{m_j}{\rho_j} f(\mathbf{x}_j) \frac{\partial W(\mathbf{x}_i - \mathbf{x}_j, h)}{\partial \mathbf{x}_i} \quad (10)$$

Here, we have used  $\partial W/\partial \mathbf{x}_i \equiv -\partial W/\partial \mathbf{x}_j$ . Equation (10) suggests that the SPH approximation of the spatial gradient of a function can be achieved without requiring to calculate the spatial derivative of the function itself, but instead through the spatial derivative of the weight function. Accordingly, an additional condition is required for choosing a suitable weighting function for SPH, that is, the weighting function must have smooth derivatives. A similar approach can be applied to derive the SPH approximation for higher-order derivatives of a function, but this will be further explored in the subsequent section in a more mathematical sense.

Upon this point, the readers should have seen that Equation (5) is the fundamental SPH formulation, which forms the basis for deriving alternative SPH formalisms. It is worth reminding that this equation was derived from the fundamental question related to *how a continuous physical quantity is estimated from the continuum field consisting of a collection of particle masses*. Therefore, Equation (5) bears more physical sense than a purely mathematical equation. This confirms our earlier

---

arguments that SPH formulations can be naturally derived from considerations of several fundamental physical processes. The readers who are interested in exploring this aspect of SPH are recommended to the excellent note by Monaghan ([Monaghan and Price, 2001](#)).

## 2.2. SPH formulations from interpolant theory

In the above section, we have taken a slightly different approach from the literature to derive the fundamental SPH formula to

demonstrate that SPH is more than a numerical method. In this section, we present the conventional way to derive fundamental SPH formulations based on the kernel interpolation theory, which was originally developed by Gingold and Monaghan (Gingold and Monaghan, 1977) and Lucy (Lucy, 1977) for astrophysical applications. This approach allows us to have a more rigorous way to evaluate and discuss the accuracy as well as numerical errors produced by the SPH formula.

### 2.2.1. Basics SPH formulation and its derivatives

The heart of SPH is based on the interpolation theory, which consists of two key steps: integral representation and particle approximation. The integral representation step involves the expression of a scalar function  $f(\mathbf{x})$  using the following identity (Monaghan, 2012, Monaghan, 2005a, Monaghan, 2005b):

$$f(\mathbf{x}) = \int_{\Omega} f(\mathbf{x}') \delta(\mathbf{x} - \mathbf{x}') d\mathbf{x}' \quad (11)$$

where  $\delta(\mathbf{x} - \mathbf{x}')$  is the Dirac delta function, which is zero everywhere except at  $\mathbf{x} = \mathbf{x}'$  where it is infinite. Equation (11) is not very useful for many engineering applications. Therefore, to make effective use of this equation, one could replace the Dirac delta function  $\delta(\mathbf{x} - \mathbf{x}')$  by a finite function, which is computable. For instance, if we replace the Dirac delta function  $\delta(\mathbf{x} - \mathbf{x}')$  by a weighting function  $W(\mathbf{x} - \mathbf{x}', h)$ , which is a function of the distance  $(\mathbf{x} - \mathbf{x}')$  and a characteristic length  $h$  such that:

$$\lim_{h \rightarrow 0} W(\mathbf{x} - \mathbf{x}', h) = \delta(\mathbf{x} - \mathbf{x}') \quad (12)$$

Equation (11) can be rewritten as follows:

$$f(\mathbf{x}) \approx \int_{\Omega} f(\mathbf{x}') W(\mathbf{x} - \mathbf{x}', h) d\mathbf{x}' \quad (13)$$

The choice of the weighting function (hereafter called kernel function) decides the accuracy of the above integral approximation. The readers could see from Equation (13) that, for a constant function, the following condition of the kernel function is required  $\int W(\mathbf{x} - \mathbf{x}', h) d\mathbf{x}' = 1$ , which is similar to the condition expressed in Equation (3) as dis-

---


$$\nabla^{\beta} f_i \approx \sum_{j=1}^N V_j f_j \nabla_i^{\beta} W_{ij} = \sum_{j=1}^N V_j \left[ f_j + \frac{\partial f_j}{\partial x^{\alpha}} (x_j - x_i)^{\alpha} + O(h^2) \right] \nabla_i^{\beta} W_{ij} \approx f_i \sum_{j=1}^N V_j \nabla_i^{\beta} W_{ij} + \frac{\partial f_i}{\partial x^{\alpha}} \sum_{j=1}^N V_j (x_j - x_i)^{\alpha} \nabla_i^{\beta} W_{ij} + O(h^2) \quad (18)$$

cussed in Section 2.1. Several other key requirements for the selection of suitable kernel function were discussed in Section 2.1, and thus are not be repeated here. To obtain the final form of SPH approximation for a function, one needs to discretise Equation (13) onto a set of particles representing a continuum field, as shown in Fig. 1 (i.e. particle approximation step). This can be achieved by replacing the integral in Equation (13) with the summation over a set of particles, each of which has a volume of  $V_j = m_j / \rho_j$ :

$$f(\mathbf{x}_i) \approx \sum_{j=1}^N V_j f_j W(\mathbf{x}_i - \mathbf{x}_j, h) \quad (14)$$

Equation (14) is commonly known as the SPH summation equation, and together with Equation (13), form the basis of all existing SPH formalisms. It states that the value of a scalar function  $f(\mathbf{x}_i)$  at a particle  $i$  can be approximated using the weighting average of its values at “neighbouring” particles located within the influence domain of the kernel function characterised by the characteristic length  $h$ . It is noted that Equation (14) is exactly similar to Equation (5), which was derived in Section 2.1, although the approaches taken to derive these equations are different. The interpolant approach presented in this section offers a more rigorous way (in the mathematical sense) to derive SPH

approximation equations for higher-order gradient terms. For instance, the gradient of function  $f(\mathbf{x})$ , hereafter referred to as  $\nabla f$ , can be straightforwardly derived by taking derivative of Equation (13), gives:

$$\nabla f(\mathbf{x}_i) \approx \sum_{j=1}^N V_j f_j (\mathbf{x}_j) \nabla_i W(\mathbf{x}_i - \mathbf{x}_j, h) \quad (15)$$

Similarly, the SPH approximation of a vector quantity  $\mathbf{f}(\mathbf{x})$  and its divergence ( $\nabla \cdot \mathbf{f}$ ) can be straightforwardly obtained using the same approach, which can be immediately written as follows, respectively:

$$\mathbf{f}(\mathbf{x}_i) \approx \sum_{j=1}^N V_j \mathbf{f}(\mathbf{x}_j) W(\mathbf{x}_i - \mathbf{x}_j, h) \quad (16)$$

$$\nabla \cdot \mathbf{f}(\mathbf{x}_i) \approx \sum_{j=1}^N V_j \mathbf{f}(\mathbf{x}_j) \cdot \nabla_i W(\mathbf{x}_i - \mathbf{x}_j, h) \quad (17)$$

Unfortunately, these SPH approximations do not always achieve satisfactory results and often results in poor approximations for a field function. For instance, the use of Equation (15) does not ensure the vanishing of gradient of a constant field function, which is troublesome when being used to estimate the strain rate or the gradient of a velocity field in computational fluid or solid mechanics. Nevertheless, an SPH formulation that guarantees the vanishing of the gradient of a constant field function is not necessarily a “good choice” in SPH simulations. These issues have led to several alternative SPH formulations in the literature, which will be discussed in the subsequent sections.

### 2.2.2. Alternative SPH formulations for its first derivatives

As discussed in the above section, the use of SPH formulations presented in Section 2.2.1 often results in poor approximations for a field function. To have a better understanding of these issues, let us have a closer look at the source of errors associated with these formulations. For instance, the errors introduced by the SPH approximation for the gradient of a scalar function in Equation (15) can be evaluated by applying the Taylor-series to expand  $f(\mathbf{x}_j)$  around  $\mathbf{x}_i$ , leading to:

$$\text{where } \alpha \text{ and } \beta \text{ indicate coordinate directions with repeated indices implying summation; } \nabla^{\beta} \equiv \partial / \partial x^{\beta}; \text{ and, to simplify our expression, we have used } f(\mathbf{x}_j) \equiv f_j \text{ and } \nabla_i W(\mathbf{x}_i - \mathbf{x}_j, h) \equiv \nabla_i W_{ij}. \quad (18)$$

Equation (18) indicates that the errors introduced by Equation (15) are controlled by the first and second terms in the second line of Equation (18), which in turn are associated with how well the SPH approximations for these terms hold:

$$\sum_{j=1}^N V_j \nabla_i^{\beta} W_{ij} \approx 0 \quad \text{and} \quad \sum_{j=1}^N V_j (x_j - x_i)^{\alpha} \nabla_i^{\beta} W_{ij} \approx \delta^{\alpha \beta} \quad (19)$$

A straightforward way to mitigate these errors is to subtract the first term in the second line of Equation (18) from Equation (15), which results in the following alternative SPH approximation for the gradient of function  $f(\mathbf{x}_i)$ :

$$\nabla f_i \approx \sum_{j=1}^N V_j (f_j - f_i) \nabla_i W_{ij} \quad (20)$$

It is noted that Equation (20) can also be derived from the following consideration:  $\nabla f = \nabla f - f(\nabla 1)$  and is commonly used in the literature. The readers could see that, although this alternative formulation exactly

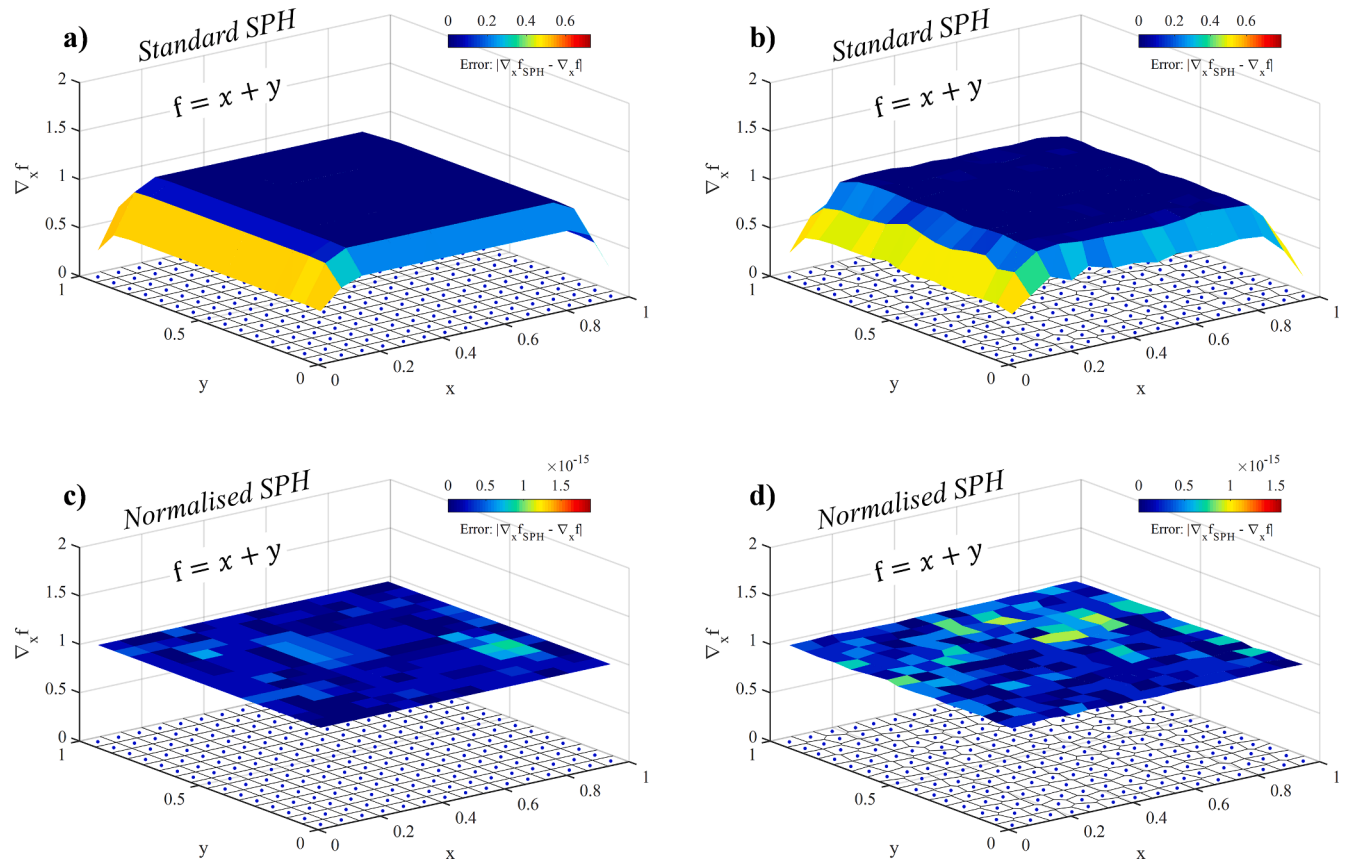


**Fig. 2.** Errors produced by SPH approximations for the gradient of a linear function  $f(x, y) = x + y$  on regular and random particle systems.

guarantees the vanishing of SPH approximation for the gradient of a constant field function, its numerical errors is still controlled by the errors associated with the second term in the second line of Equation (18). To completely eliminate these errors (i.e. up to second-order accuracy), one could normalise Equation (20) by  $\sum_{j=1}^N V_j (x_j - x_i)^\alpha \nabla^{\beta_j} W_{ij}$  in the second line of Equation (18), leading to the following normalised SPH formulation for the kernel derivative (Randles and Libersky, 1996, Chen and Beraun, 2000):

$$\nabla f_i \approx \sum_{j=1}^N V_j (f_j - f_i) \mathbf{L}_{ij} \nabla_i W_{ij} \quad (21)$$

where  $\mathbf{L}_{ij} = [\sum_{j=1}^N V_j (x_j - x_i)^\alpha \nabla^{\beta_j} W_{ij}]^{-1}$  is the normalised matrix. The accuracy of different SPH gradient operators, i.e. Equations (20) and (21), for a linear field function is illustrated in Fig. 2. Here, we have adopted the popular Cubic-spline kernel function (see Section 2.3) with a smoothing length of  $h = 1.3dx$ , where  $dx$  is the distance between two adjacent SPH particles. On structured particle arrangement, the SPH gradient operator (20) produces results that are comparable to analytical values for interior particles, but fail to maintain the same level of accuracy for particles located near the boundaries due to the well-known kernel truncation issue (Fig. 2a). This kernel truncation issue can be straightforwardly removed by either creating several extra layers of particles on the boundary domains or simply adopting the SPH gradient operator (21), which also helps to achieve better accuracy for the SPH approximation of a linear field function, as shown in Fig. 2c. The difference between the two SPH gradient operators is clearly visible on the

non-regular particle system, where the result predicted by the SPH gradient operator (20) oscillates for both boundary and interior particles (Fig. 2b). On the other hand, the SPH operator (21) maintains a stable result across the domain, and the errors are negligible (Fig. 2d).

An alternative SPH operator for the gradient of a function at a particle  $i$  can also be derived by considering the following arrangement:

$$\nabla f_i = \frac{[\nabla(\rho f) - f \nabla \rho]}{\rho} \Big|_i = \frac{1}{\rho_i} \sum_{j=1}^N m_j [f_j - f_i] \nabla_i W_{ij} \quad (22)$$

in which we have applied the SPH operator (15) to evaluate the gradient terms. This formulation again guarantees the vanishing of SPH approximation of the gradient of a constant field function and can be equally used as an alternative to Equation (20), although their accuracy is both influenced by the kernel truncation issue at the boundary domains, as illustrated in Fig. 2a and b. The readers can apply the same Taylor series expansion approach to eliminate errors associated with this equation as done for Equation (21), and we will not repeat this process here.

Finally, it is worth mentioning the following well-known SPH gradient operators, which are commonly used to evaluate the gradient of the stress (or pressure) in the momentum equation, which will be discussed later along with the general SPH governing equations. These SPH gradient operators can be derived from the following considerations:

$$\nabla f_i = \rho \left[ \frac{f}{\rho^2} \nabla \rho + \nabla \left( \frac{f}{\rho} \right) \right]_i \approx \rho_i \sum_{j=1}^N m_j \left[ \frac{f_i}{\rho_i^2} + \frac{f_j}{\rho_j^2} \right] \nabla_i W_{ij} \quad (23)$$

And

$$\nabla f|_i = \nabla f + f(\nabla 1)|_i \approx \sum_{j=1}^N m_j \left[ \frac{f_i + f_j}{\rho_j} \right] \nabla_i W_{ij} \quad (24)$$

The readers could see that the above SPH operators do not guarantee the vanishing of the gradient approximation of a constant field function. Instead, they result in an operator that produces a sort of pairwise-symmetric contribution to the gradient operator from both particles  $i$  and  $j$  for a given pair of interaction. This SPH approximation property is particularly useful in discretising the momentum equation of a continuum system, which strictly requires the conservations of both linear and angular momenta. Although we could eliminate numerical errors associated with the above SPH operators (e.g. using the Taylor series), we prefer not to do so because the exact conservation of momentum equation requires these errors, and these are one of several interesting

$$\int (f_j - f_i) \frac{\mathbf{x}_{ji} \cdot \nabla_i W_{ij}}{|\mathbf{x}_{ji}|^2} d\mathbf{x}_j = \frac{\partial f_i}{\partial x^\alpha} \int x_{ji}^\alpha \frac{\mathbf{x}_{ji} \cdot \nabla_i W_{ij}}{|\mathbf{x}_{ji}|^2} d\mathbf{x}_j + \frac{1}{2} \frac{\partial^2 f_i}{\partial x^\alpha \partial x^\beta} \int x_{ji}^\alpha x_{ji}^\beta \frac{\mathbf{x}_{ji} \cdot \nabla_i W_{ij}}{|\mathbf{x}_{ji}|^2} d\mathbf{x}_j \quad (29)$$

features of the SPH method. We will go back to this issue later. Finally, the same methodology discussed above can be applied to obtain the SPH approximation for the gradient of a vector field and thus will not be repeated.

### 2.2.3. SPH formulations for Laplacian

The SPH approximation of the Laplacian that involves second derivatives of a scalar field function or vector quantities can be obtained in a way similar to the SPH approximation for the first derivatives. By taking derivatives of Equation (14) and applying the Taylor-series to expand  $f_j$  around  $\mathbf{x}_i$  up to the first order of accuracy, one could derive the following SPH operator for the second derivatives<sup>2</sup>:

$$\nabla^2 f \approx \sum_{j=1}^N \frac{m_j}{\rho_j} (f_j - f_i) \nabla_i^2 W_{ij} \quad (25)$$

which guarantees the vanishing of gradients of both constant and linear field functions. The remaining errors associated with this SPH operator (i.e. up to the third order of accuracy) are:

$$\frac{\partial f_i}{\partial x^\alpha} \sum_{j=1}^N \frac{m_j}{\rho_j} x_{ji}^\alpha \nabla_i^2 W_{ij} + \frac{1}{2} \frac{\partial}{\partial x^\alpha} \left( \frac{\partial f_i}{\partial x^\beta} \right) \sum_{j=1}^N \frac{m_j}{\rho_j} x_{ji}^\alpha x_{ji}^\beta \nabla_i^2 W_{ij} + O(h^3) \quad (26)$$

which again relies on how well the SPH approximations for these terms hold:

$$\sum_{j=1}^N \frac{m_j}{\rho_j} \nabla_i^2 W_{ij} \approx 0 \quad \text{and} \quad \sum_{j=1}^N \frac{m_j}{\rho_j} x_{ji}^\alpha x_{ji}^\beta \nabla_i^2 W_{ij} \approx \delta^{\alpha\beta} \quad (27)$$

To completely eliminate these errors, one could adopt a similar approach, which was used to derive the SPH operators for the first derivatives (see Section 2.2.2). However, the issue associated with the above SPH operator for the Laplacian, i.e. Equation (25), is that it involves the second derivatives of the kernel function. Unfortunately, for most existing kernel functions, their second derivatives changes sign within the kernel influence domain, as shown in Fig. 3 for the two most popular Gaussian and Cubic-spline kernel functions (Monaghan, 2005a; Monaghan and Lattanzio, 1991; Monaghan, 2005b). This makes the

conditions in Equation (27) extremely hard to be satisfied because it requires a very symmetric distribution of particles in each direction. Therefore, for practical SPH applications, it is recommended to avoid the use of the second derivatives of the kernel function. Accordingly, a different way to approximate the second derivatives of a function by SPH is needed.

A straightforward method to derive the SPH approximation for the Laplacian of a function is to apply the Taylor series expansion of a function  $f_j$  around  $\mathbf{x}_i$  up to the third order of accuracy, giving:

$$f_j = f_i + \frac{\partial f_i}{\partial x^\alpha} x_{ji}^\alpha + \frac{1}{2} \frac{\partial^2 f_i}{\partial x^\alpha \partial x^\beta} x_{ji}^\alpha x_{ji}^\beta + O(h^3) \quad (28)$$

Next, multiplying Equation (28) by  $\mathbf{x}_{ji} \cdot \nabla_i W_{ij} / |\mathbf{x}_{ji}|^2$  and integrating both sides of the equation, giving:

From the integral theory, the integral of the first term on the right-hand side of Equation (29) vanishes for a symmetric kernel function  $W$  while that of the second term should result in a delta function  $\delta^{\alpha\beta}$ , which ultimately gives  $\frac{1}{2} \nabla^2 f_i$ . Accordingly, by rearranging Equation (29), we have<sup>3</sup>:

$$\nabla^2 f_i = 2 \int (f_j - f_i) \frac{\mathbf{x}_{ji} \cdot \nabla_i W_{ij}}{|\mathbf{x}_{ji}|^2} d\mathbf{x}_j \quad (30)$$

By performing the SPH approximation of the above integral onto a finite set of particles, the following SPH operator for the Laplacian of a function can be obtained:

$$\nabla^2 f_i \approx 2 \sum_{j=1}^N V_j (f_j - f_i) \frac{\mathbf{x}_{ji} \cdot \nabla_i W_{ij}}{|\mathbf{x}_{ji}|^2} \quad (31)$$

which shares a similar form to the SPH approximation for the Laplacian derived by Brookshaw (Brookshaw, 1985) and Monaghan (Monaghan, 2005a; Monaghan, 2005b). This SPH Laplacian only involves the first derivative of the kernel function, and thus could avoid issues associated with the second derivatives of the kernel function as discussed earlier. Up to this point, the readers should have immediately seen that the accuracy of Equation (31) relies on how well the SPH approximations for the following terms hold:

$$\int x_{ji}^\alpha \frac{\mathbf{x}_{ji} \cdot \nabla_i W_{ij}}{|\mathbf{x}_{ji}|^2} d\mathbf{x}_j \approx \sum_{j=1}^N V_j x_{ji}^\alpha \frac{\mathbf{x}_{ji} \cdot \nabla_i W_{ij}}{|\mathbf{x}_{ji}|^2} \approx 0 \quad (32)$$

$$\int x_{ji}^\alpha x_{ji}^\beta \frac{\mathbf{x}_{ji} \cdot \nabla_i W_{ij}}{|\mathbf{x}_{ji}|^2} d\mathbf{x}_j \approx \sum_{j=1}^N V_j x_{ji}^\alpha x_{ji}^\beta \frac{\mathbf{x}_{ji} \cdot \nabla_i W_{ij}}{|\mathbf{x}_{ji}|^2} \approx \delta^{\alpha\beta} \quad (33)$$

These conditions are, however, not easy to achieve by SPH and, for this reason, Equation (31) is often cited for having a low accuracy and being sensitive to the particle disordered, in addition to the issue associated with the kernel truncation at the boundary. To improve the accuracy of Equation (31), one could subtract the first term on the right-hand side of Equation (29) from its left-hand side and performing the SPH approximations, leading to the following equation:

<sup>2</sup> An alternative way to derive this SPH operator is to replace the function  $f$  in Equation (13) by  $\nabla^2 f$  and applying the Gaussian theorem as done for the first derivative.

<sup>3</sup> Here, we have ignored the integral errors associated with these operations.

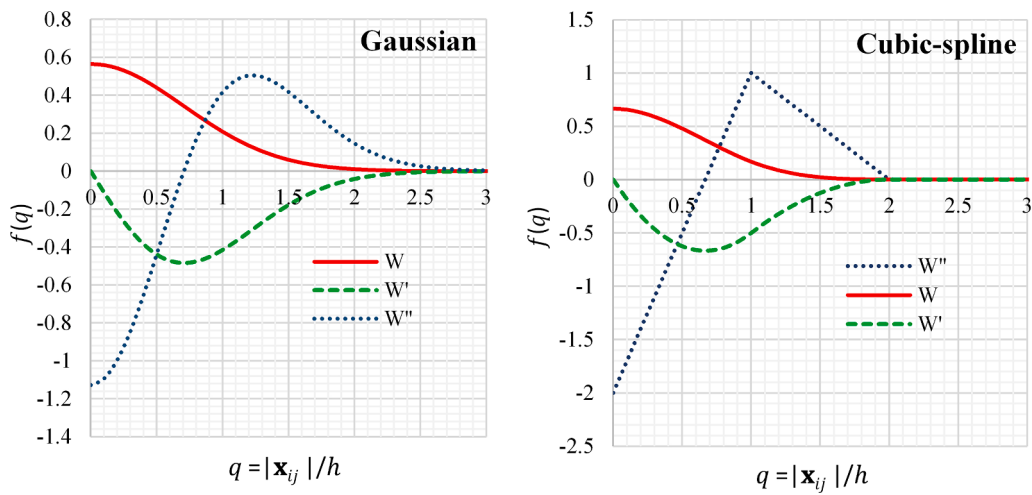


**Fig. 3.** Gaussian and Cubic-spline kernel functions and their derivatives, respectively.

$$2 \sum_{j=1}^N V_j (f_j - f_i) \frac{\mathbf{x}_{ji} \cdot \nabla_i W_{ij}}{|\mathbf{x}_{ji}|^2} - 2 \frac{\partial f_i}{\partial x^\alpha} \sum_{j=1}^N V_j x_{ji}^\alpha \frac{\mathbf{x}_{ji} \cdot \nabla_i W_{ij}}{|\mathbf{x}_{ji}|^2} = \frac{\partial^2 f_i}{\partial x^\alpha \partial x^\beta} \sum_{j=1}^N V_j x_{ji}^\alpha x_{ji}^\beta \frac{\mathbf{x}_{ji} \cdot \nabla_i W_{ij}}{|\mathbf{x}_{ji}|^2} \quad (34)$$

which removes SPH approximation errors associated with condition (32). The remaining error source of Equation (31) is associated with the condition (33), and to visualise this error, one can further expand the right-hand side of Equation (34), assuming 2D coordinate system, to obtain the following:

$$\underbrace{\frac{\partial^2 f_i}{\partial x^2} \sum_N V_j x_{ji}^2 \frac{\mathbf{x}_{ji} \cdot \nabla_i W_{ij}}{|\mathbf{x}_{ji}|^2}}_A + 2 \underbrace{\frac{\partial^2 f_i}{\partial x \partial y} \sum_N V_j x_{ji} y_{ji} \frac{\mathbf{x}_{ji} \cdot \nabla_i W_{ij}}{|\mathbf{x}_{ji}|^2}}_B + \underbrace{\frac{\partial^2 f_i}{\partial y^2} \sum_N V_j y_{ji}^2 \frac{\mathbf{x}_{ji} \cdot \nabla_i W_{ij}}{|\mathbf{x}_{ji}|^2}}_C \quad (35)$$

Condition (33) requires  $A = C = 1$  and  $B = 0$ , which ultimately results in expression (35) being the Laplacian  $\nabla^2 f_i$ . To achieve this condition, and thus removing numerical errors for the SPH approximation of the Laplacian up to the third-order Taylor-series expansion, one can adopt the CSPH method previously derived by Chen et al. (Chen and Beraun, 2000), which involves the inversion of a three-by-three matrix (in 2D and more complex in 3D) to solve a linear system equation for the second derivatives for every SPH particle. Although CSPH offers a rigorous approach to derive higher-order accurate SPH approximations for the second derivatives, the method requires high computation costs for each SPH simulation and thus losing the attractiveness of the SPH method.

To have a balance between robustness and mathematical rigour, whilst still keeping the attractiveness of the SPH method being simple and robust, an alternative approach is proposed in this work. First, condition (33) requires  $B = 0$  throughout the SPH computation and the easiest way to ensure this condition in SPH is to remove this term from the above SPH approximation, which ultimately eliminates errors associated with this term and leading to the following approximation:

$$\underbrace{\frac{\partial^2 f_i}{\partial x^2} \sum_N V_j x_{ji}^2 \frac{\mathbf{x}_{ji} \cdot \nabla_i W_{ij}}{|\mathbf{x}_{ji}|^2}}_A + \underbrace{\frac{\partial^2 f_i}{\partial y^2} \sum_N V_j y_{ji}^2 \frac{\mathbf{x}_{ji} \cdot \nabla_i W_{ij}}{|\mathbf{x}_{ji}|^2}}_C \quad (36)$$

Next, one needs to ensure  $A = C = 1$  throughout the SPH computation such that the approximation (36) results in the Laplacian  $\nabla^2 f_i$ . The equality  $A = C$  holds for a regular SPH particle configuration, but this equality might be lost, and  $A$  starts departing from  $C$  as the level of particle disorder increases, which is again attributed to the SPH summation errors. We note that the same SPH summation errors occur on the right-hand side of Equation (34), and thus, simply enforcing  $A = C = 1$  to expression (36) does not resolve the problem. Nevertheless, from the symmetry in a 2D space, we can equal the summation as follows:

$$\underbrace{\sum_N^{j=1} V_j x_{ji}^2 \frac{\mathbf{x}_{ji} \cdot \nabla_i W_{ij}}{|\mathbf{x}_{ji}|^2}}_A = \underbrace{\sum_N^{j=1} V_j y_{ji}^2 \frac{\mathbf{x}_{ji} \cdot \nabla_i W_{ij}}{|\mathbf{x}_{ji}|^2}}_C = \frac{1}{2} \left[ \sum_N^{j=1} V_j (x_{ji}^2 + y_{ji}^2) \frac{\mathbf{x}_{ji} \cdot \nabla_i W_{ij}}{|\mathbf{x}_{ji}|^2} \right] \quad (37)$$

Substituting this expression into the expression (35) leads to the following expression:

$$\frac{1}{2} \left[ \sum_{j=1}^N V_j (x_{ji}^2 + y_{ji}^2) \frac{\mathbf{x}_{ji} \cdot \nabla_i W_{ij}}{|\mathbf{x}_{ji}|^2} \right] \left( \frac{\partial^2 f_i}{\partial x^2} + \frac{\partial^2 f_i}{\partial y^2} \right) = K_{ij} \left( \frac{\partial^2 f_i}{\partial x^2} + \frac{\partial^2 f_i}{\partial y^2} \right) = K_{ij} \nabla^2 f_i \quad (38)$$

We acknowledge the above approximation leading to expression (38) is not unique, and further research is required to find a better way to enforce the condition (33). However, the approach we proposed in this work offers a superior way to balance between the accuracy and computational costs to improve the accuracy of SPH approximation for the Laplacian. We will demonstrate later that the above approximation significantly improves the accuracy of SPH approximation for the Laplacian, especially for a random particle configuration. Finally, by substituting expression (38) into Equation (31), and making use of Equation (21) for the first gradient approximation, the following SPH approximation for the Laplacian  $\nabla^2 f_i$  could be derived:

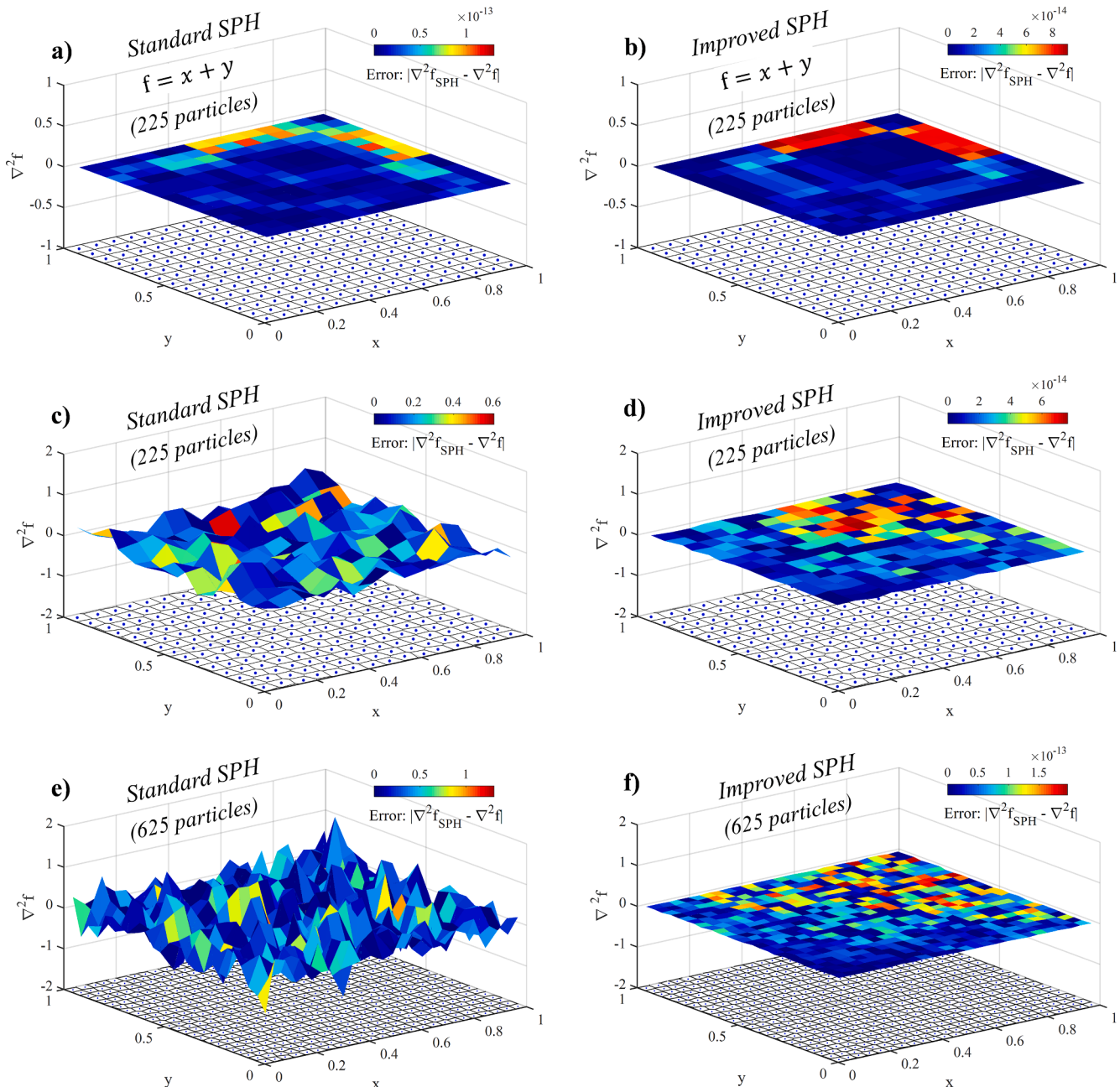


**Fig. 4.** Errors produced by SPH approximations of the Laplacian of a linear function:  $f(x, y) = x + y$ . Extra layers of particles were created on the boundary to remove the kernel truncation errors associated with the standard SPH formulation.

$$\nabla^2 f_i = \frac{2}{K_{ij}} \left[ \sum_{j=1}^N V_j (f_j - f_i) \frac{\mathbf{x}_{ji} \cdot \nabla_i W_{ij}}{|\mathbf{x}_{ji}|^2} - \sum_{j=1}^N V_j (f_j - f_i) \mathbf{L}_{ij} \nabla_i^a W_{ij} \sum_{j=1}^N V_j x_{ji}^a \frac{\mathbf{x}_{ji} \cdot \nabla_i W_{ij}}{|\mathbf{x}_{ji}|^2} \right] \quad (39)$$

Compared to the original SPH approximation for the Laplacian, i.e. Equation (31), the new formulation only incurs an extra computational cost to estimate the inversion of a  $(2 \times 2)$   $\mathbf{L}_{ij}$  matrix. However, this matrix inversion can be analytically computed for both 2D and 3D conditions, and thus the extra computational cost involved to compute this term is not significant. Indeed,  $\mathbf{L}_{ij}$  matrix could be used to improve the accuracy of SPH approximation for the first derivative, i.e. Equation

(21). In such applications,  $\mathbf{L}_{ij}$  matrix can be readily used without additional computational cost. The new formulation shares the same feature as the original one, which guarantees the vanishing of the gradient of a constant field function. It removes SPH approximation errors associated with the condition (32) and thus should be able to exactly reproduce the approximation for a liner field function. Nevertheless, because of the approximation for Equation (38), the new formulation only reduces

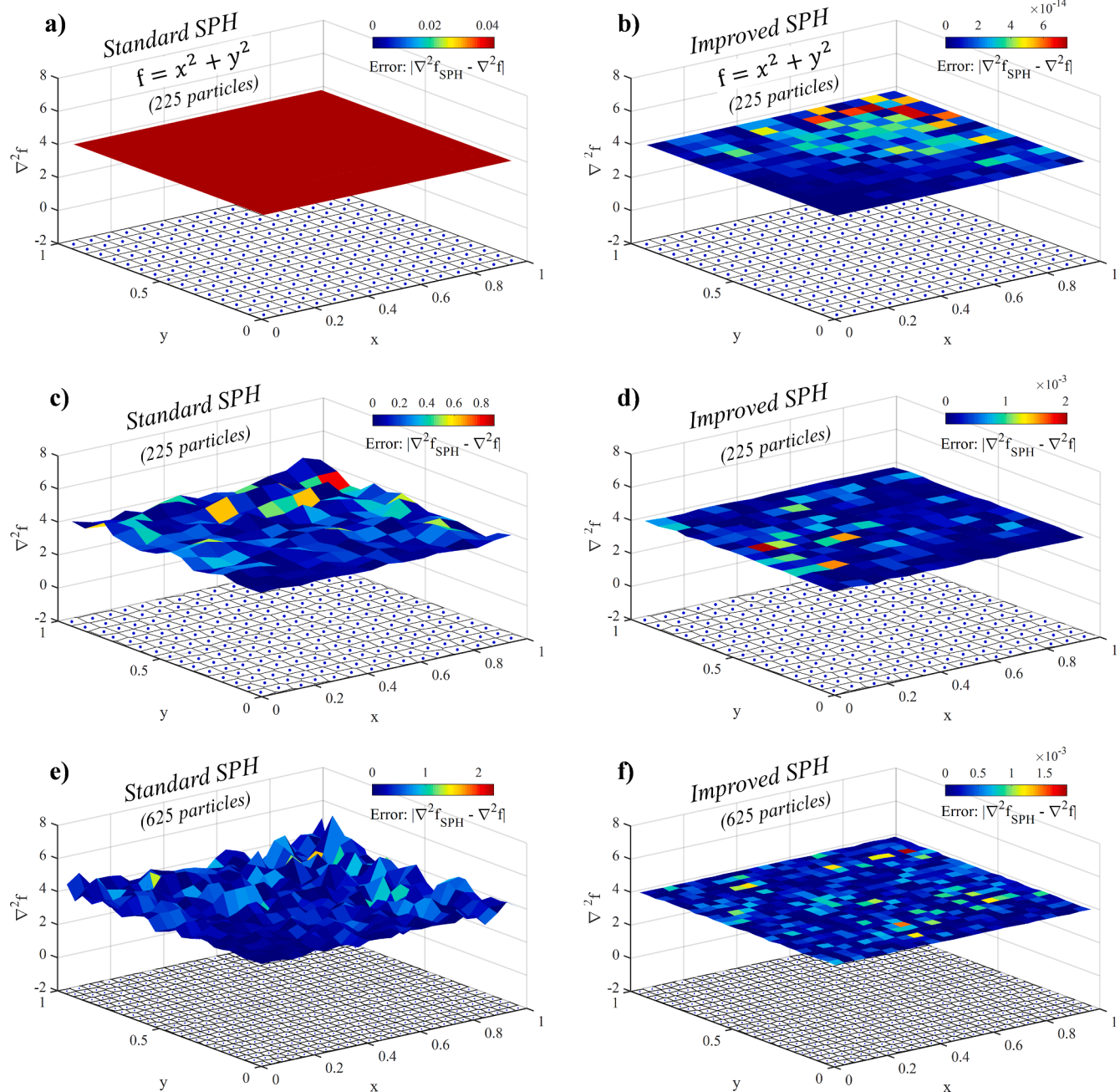


**Fig. 5.** Errors produced by SPH approximations of the Laplacian of a non-linear function:  $f(x, y) = x^2 + y^2$ . Boundary particles were used but not presented in the figure.

errors associated with the condition (33) for a non-linear function, not completely removing these errors.

Fig. 4 demonstrates the accuracy of Equations (31) and (39) for the SPH approximations of the Laplacian of a linear function on both regular and non-regular particle systems. The same cubic-spline function is adopted with a smoothing length of  $h = 1.3dx$ , where  $dx$  is the distance between two adjacent SPH particles. In addition, to avoid the obvious kernel truncation issue at the boundary (as illustrated in Fig. 2), three extra layers of particles were created on the boundary domains, and the plot does not present the information on these particles. It can be seen that on the regular particle systems, both the standard and new SPH formulations could exactly reproduce the SPH approximation of the Laplacian of a linear function. The errors of magnitude  $10^{-13}$  and  $10^{-14}$  are negligible and considered as round-off errors (Fig. 4a and b). The difference is clearly visible on the non-regular particle system, as shown

in Fig. 4c and d. The standard SPH formulation (31) produces a highly oscillated result with low accuracy on the non-regular particle system (Fig. 4c), which can be attributed to the SPH summation errors associated with conditions (32) and (33). The accuracy of the standard SPH formulation further deteriorates as the number of particles or the level of particle disorder increases, as shown in Fig. 4e. We note that the standard SPH formulation for the Laplacian also suffers from the kernel truncation errors at the boundaries, which is similar to the SPH approximation for the first derivative. On the other hand, the new SPH formulation (39) completely removes these errors, and the result appears to be less sensitive to the particle disorder, at least for the approximation of the linear field function, as demonstrated in Fig. 4d and f. The numerical errors produce by the new formulation is again negligible (i.e. round-off errors), and similar results could be achieved for a more random particle configuration, more particles in the system

or even without the presence of the boundary particles.

The performance of both SPH operators is further demonstrated for a non-linear function and shown in Fig. 5. The accuracy of the standard SPH operator (31) reduces for both regular and non-regular particle systems. In particular, the standard SPH formulation could not reproduce the exact approximation for a non-linear function (Fig. 5a) on the regular particle system, producing oscillating results on the non-regular particle system with a further reduction of accuracy (Fig. 5c), and further deteriorating as the number of particles or the level of particle disorder increases (Fig. 5e). On the other hand, the new SPH operator (39) exactly reproduces the approximation for the considered non-linear function on the regular particle system with negligible errors (Fig. 5b). The performance of the new formulation is shown to be significantly improved on the non-regular particle system (Fig. 5d) and maintains the same level of accuracy as the number of particles or the level of particle disorder increases (Fig. 5f). The numerical errors produced on the non-regular particle system is very small and can be attributed to errors associated with the approximation of Equation (38). In our view, these errors are acceptable and is considered as a price to pay for a robust SPH formulation, in addition to the SPH capability to handle extremely large deformation and flow failure problems, which are the real challenges for other numerical methods. In conclusion, by considering the accuracy and robustness, the newly proposed SPH formulation for the approximation of the Laplacian outperforms existing SPH formulations. A similar approach could be used to derive general SPH approximations for the second derivatives, and this work will be presented in future publications.

### 2.3. Selection of kernel functions and associated issues

The selection of appropriate kernel function in SPH will directly affect the accuracy, efficiency and stability of SPH algorithms. As discussed in Section 2.1, a good kernel function needs to satisfy several key requirements, which are summarised below:

1. It must be positive, symmetric with respect to the particle distance and have smooth first and second derivatives.
2. It should have a compact domain and smoothly reduces as the distance from the centre of the kernel function increases.
3. It must satisfy the normalised condition, which requires  $\int W(\mathbf{x}_i - \mathbf{x}_j, h) dV = 1$

Most exiting kernel functions in the literature satisfy the above requirements, and the two most popular kernel functions are the Gaussian kernel function and cubic-spline function. The Gaussian kernel function takes the following form (Monaghan, 2005a):

$$W(q, h) = \alpha_d \exp[-q^2] \quad (40)$$

where  $q = |\mathbf{x}_{ij}|/h$  is the ratio between the distance between two particles and the smoothing length  $h$ , which defines the rate of falling-off of  $W$  or the area of the kernel influence domain; and  $\alpha_d$  is the normalisation factor given as  $\alpha_d = [1/h\sqrt{\pi}, 1/\pi h^2, 1/(h^2\pi\sqrt{\pi})]$  for one-, two- and three-dimensions, respectively. The cubic-spline function takes the form (Monaghan and Lattanzio, 1991, Monaghan, 2005b):

$$W(q, h) = \alpha_d \begin{cases} \frac{2}{3} - q^2 + \frac{1}{2}q^3 & 0 \leq q < 1 \\ \frac{1}{6}(2-q)^3 & 1 \leq q < 2 \\ 0 & q \geq 2 \end{cases} \quad (41)$$

where  $\alpha_d$  is the dimensional normalising factor defined by  $\alpha_d = [1/h, 15/7\pi h^2, 3/2\pi h^2]$  for one-, two- and three-dimensions, respectively.

The graphical representation of these kernel functions and their derivatives were shown in Fig. 3. Compared to the Cubic-spline function, the Gaussian kernel function does not have a compact domain<sup>4</sup>, so all particles contribute to the SPH approximation in the computation, resulting in an extremely unnecessary large computational cost, i.e. in the order of  $O(N^2)$  with  $N$  being the total number of particles in the system. In contrast, the Cubic-spline function drops quickly and approaches zero as  $q = 2$  and thus allowing to reduce the calculation to a sum over closely neighbouring particles, which dramatically reduces the cost to  $O(nN)$  with  $n$  being the number of contributing neighbours, although there is an additional cost of finding the neighbouring particles.

In addition to the computational issue, the selection of kernel function will have a direct impact on the stability of SPH simulations. For instance, in the areas of computational fluid mechanics or astrophysics, the SPH estimation of density is very important as this quantity is subsequently used to compute the pressure, which governs the motion of the entire system. The SPH kernel approximation controls the accuracy of density calculation and thus has a direct influence on the numerical stability of the application. An earlier study conducted by Dehnen and Aly (Dehnen and Aly, 2012) on the stability of SPH concluded that the misuse of Gaussian and Cubic-spline kernel functions would facilitate the so-call pairing instability for a randomly disordered particle system, in which particles tend to form a clump in the numerical simulations. It is noted that the paring instability is different from the tensile instability, which is caused by negative stresses/pressures resulting in an attractive force between two particles. Unfortunately, most existing research in the literature, at least in the area of computational solid mechanics and geomechanics, does not distinguish these issues and thus giving a wrong impression about the tensile instability in SPH. Dehnen and Aly (Dehnen and Aly, 2012) argue that the paring issue in SPH is mainly caused by the SPH density estimator error resulted from the misuse of kernel estimations. In particular, each kernel function has a compacted domain, which can accommodate a limited number of “neighbouring” particles in its kernel estimation. When the number of “neighbouring” particles within the kernel domain exceeds a certain threshold (i.e. in a highly disordered system or chaotic system), the kernel estimation would result in significant errors. One way to mitigate these estimation errors, as well as to repair the pairing instability issue, is to use the Wendland  $C^2$  kernel function, which takes the following form for 1D condition:

$$W(q, h) = \alpha_d \begin{cases} (1 - 0.5q)^3(1.5q + 1) & 0 \leq q \leq 2 \\ 0 & q > 2 \end{cases} \quad (42)$$

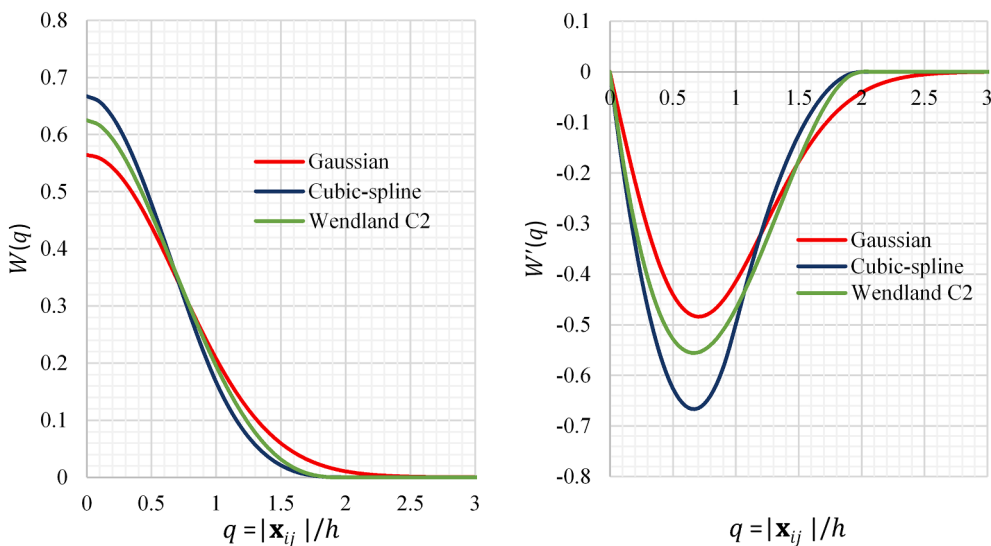
and the following form for 2D & 3D conditions:

$$W(q, h) = \alpha_d \begin{cases} (1 - 0.5q)^4(2q + 1) & 0 \leq q \leq 2 \\ 0 & q > 2 \end{cases} \quad (43)$$

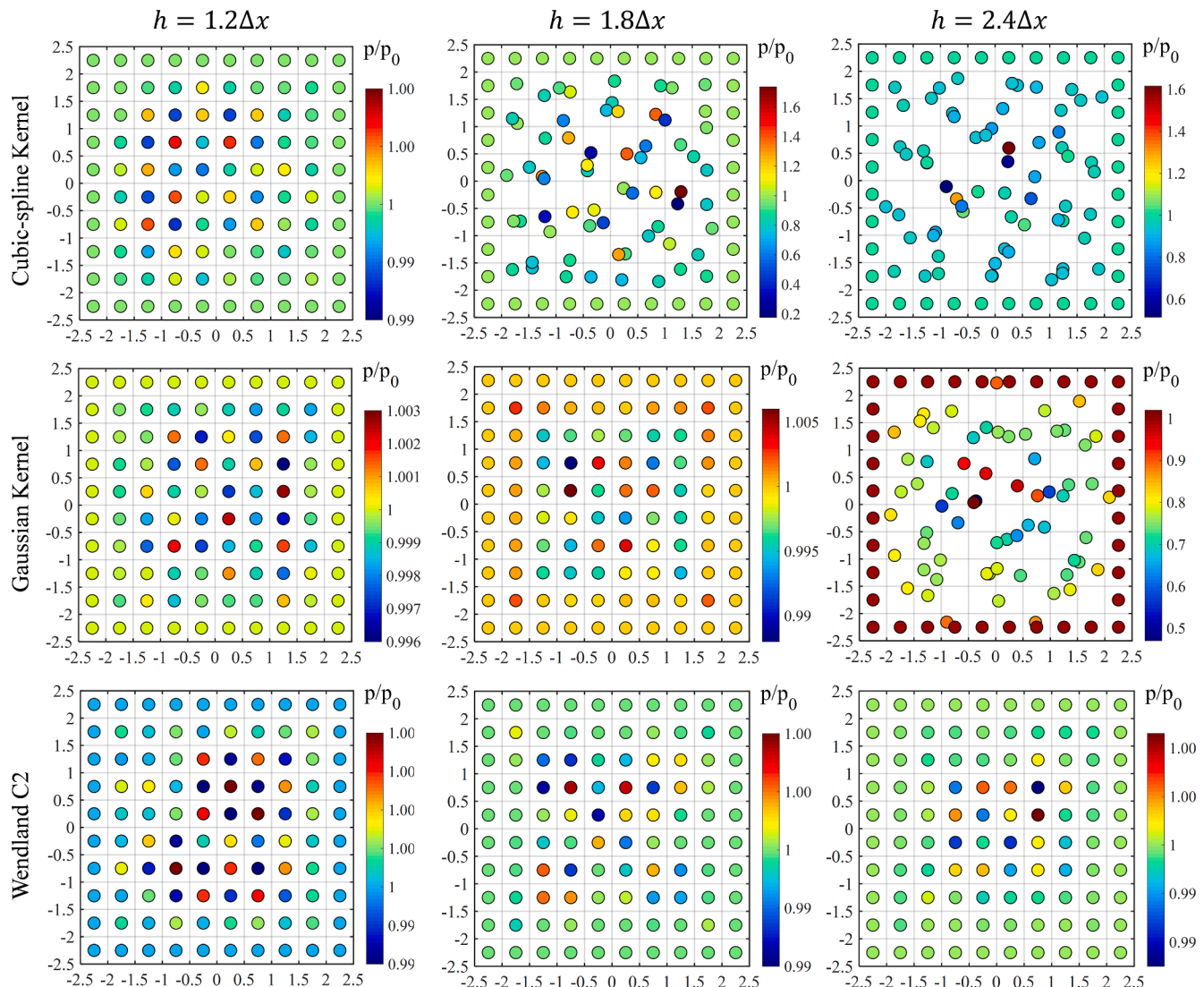
where  $\alpha_d$  is the dimensional normalising factor defined by  $\alpha_d = [5/8h, 7/4\pi h^2, 21/2\pi h^2]$  for one, two and three-dimensions, respectively.

Fig. 6 shows a comparison between the Wendland  $C^2$  kernel function against the other two popular ones. It can see that, similar to the Cubic-spline function, the Wendland  $C^2$  kernel function also features a compact support domain. However, the Wendland  $C^2$  kernel function can slightly accommodate more “neighbouring particles” than that of the Cubic-spline function. All three kernel functions also feature the so-called inflection point (i.e. the zero gradient point at the peak of the kernel function), which was attributed to the source of the pairing instability (Dehnen and Aly, 2012). This is because the gradient of the kernel function controls the magnitude of the interaction force between a pair of particles, see Equation (54), and thus particles located near the

<sup>4</sup> Note that the plot of Gaussian kernel function and its derivatives in Fig. 3 are truncated at  $q = 3$



**Fig. 6.** Comparison of Wendland C<sup>2</sup> kernel function and its first derivatives against the Gaussian and Cubic-spline kernel function.



**Fig. 7.** Misuses of kernel functions causing pairing instability in SPH simulations of elastic materials. The pressure is defined as  $p = (\sigma_{xx} + \sigma_{yy} + \sigma_{zz})/3$ .

inflection point would not gain enough repulsive force from their neighbouring particles. Nevertheless, even with the presence of the inflection point, the Wendland  $C^2$  kernel function does not show any sign of pairing instability (Dehnen and Aly, 2012). To demonstrate the pairing instability issue associated with a misuse of kernel function, a simple numerical test consisting of isotropic linear elastic SPH particles (with a density of  $\rho = 2700 \text{ kg/m}^3$ , elastic modulus  $E = 10 \text{ MPa}$  and Poisson's ratio  $\nu = 0.3$ ) subjected to a small perturbation is conducted. Initially, all SPH particles were uniformly distributed in a square box with an initial distance of  $\Delta x = \Delta y = 0.5 \text{ m}$ . The initial velocity all particles was set to zero, except the central particle which was assigned to a small velocity of  $v_x = v_y = 10^{-5}$  to produce a small perturbation. During the computational, the velocity of boundary particles was kept zero to prevent interior particles moving out of the box. In addition, to avoid the tensile instability which is caused by negative pressure, an initial pressure of  $p_0 = 5 \text{ kPa}$  was assigned to all particles. The governing equations used to describe the motion of particles in this simulation following the standard SPH governing equations for solid (Section 3.1) with a simple linear elastic constitutive model described in Section 3.2.2. To facilitate the pairing instability, we have intentionally designed the tests in such a way that both Gaussian and Cubic-spline functions will have more neighbouring particles than the standard number of particles that these kernels can accommodate. The simulations were then run for a long enough period of time (again to facilitate the pairing instability), and the results are shown in Fig. 7. The particle system in the Cubic-spline kernel function remains stable for the smoothing length  $h = 1.2\Delta x$  (or  $kh/\Delta x = 2.4$ ) with  $k$  being a scalar parameter and together with defining the influence domain of the kernel function. The paring instability (i.e. particles formed clumps) then occurs in the simulations with  $h = 1.8\Delta x$  and  $h = 2.4\Delta x$  when the Cubic-spline function was forced to take more neighbouring particles than the actual number of particles it can accommodate, which is around  $kh/\Delta x = 2.4$ . The Gaussian kernel function works better, and the results remain stable for both simulations with  $h = 1.2\Delta x$  and  $h = 1.8\Delta x$ , thanks to the capability of the Gaussian kernel function to accommodate more neighbouring particles due to its infinite kernel domain. However, as the number of neighbouring particles increases to an excessive number (i.e.  $h = 2.4\Delta x$ ), the pairing instability again occurs in the simulation. In contrast, the Wendland  $C^2$  kernel function could maintain stable results for all three tested smoothing lengths, and this can be theoretically explained by the linear stability analysis for conservative SPH in spatial dimensions (Dehnen and Aly, 2012). In particular, Dehnen and Aly (Dehnen and Aly, 2012) demonstrated that SPH kernel functions whose Fourier transform is negative for some wave vectors would inevitably trigger the SPH paring instability at a sufficiently large number of neighbouring particles, which are the cases for both Cubic-spline and Gaussian functions. To sufficiently use these kernel functions, the number of neighbouring particles needs to be sufficiently maintained not to exceed a certain threshold, which depends on specific applications. In contrast, the Wendland  $C^2$  kernel function shows a non-negative Fourier transform and demonstrates a remarkable feature in removing the paring instability. This suggests that the Wendland  $C^2$  kernel function is a good candidate for dealing with problems involved highly disordered particles. Nevertheless, the drawback of the Wendland  $C^2$  kernel function is that it suffers comparably large errors when the number of neighbouring particles is low. Thus, when using the Wendland  $C^2$  kernel function, it is important to maintain a good number of neighbouring particles.

The above numerical tests show that the misuse of kernel functions (i.e. forcing the kernel function to take more particles than its capacity) could cause the pairing instability issue even though there is no negative pressure (i.e. causing attraction force) in the system. In fact, there has been a common misconception on this issue reported in the literature. Most existing research, at least in the area of computational solid mechanics and geomechanics, did not recognise or distinguish this pairing

instability issue from the tensile instability and thus often mixed up the pairing instability issue with the tensile instability, which is caused by negative pressures/stresses. This has resulted in an exaggerated impression that SPH is heavily suffered from the tensile instability problem in the literature, which is incorrect as the pairing instability issue could be completely eliminated when appropriate kernel functions are adopted. As pointed out in the earlier research on the SPH application for geomechanics using the plasticity theory, Bui et al. (Bui, 2007, Bui et al., 2008a) demonstrated that tensile instability only occurs in SPH when being applied to simulate cohesive granular materials, which features the tensile stress zone (i.e. negative stress) in the yielding stress space. On the other hand, for non-cohesive granular materials, no tensile instability was observed in SPH simulations, and SPH could be applied well to simulate granular materials without any issue. We will come back to this tensile instability issue later with more demonstration after introducing SPH governing equations for geomaterials and relevant material constitutive models used to describe the behaviour of these materials.

#### 2.4. Choosing smoothing length for kernel function

In SPH simulations, each particle is assigned with a smoothing length, which controls the size of the kernel supporting domain and thus the number of neighbouring particles. In addition, depending on specific kernel functions, the smoothing length should be set to maximise its benefit. For example, the recommended smoothing length for the Cubic-spline function is within  $h/\Delta x = 1.0 - 1.5$ , and that for the Gaussian kernel functions should be less than 2.0. Failure to maintain these numbers will facilitate the paring stability issue demonstrated in Fig. 7. Furthermore, in early SPH applications, the smoothing length of each particle was often kept unchanged but gradually found to be no longer suitable for applications involving highly disordered particles such as complex free-surface flows or debris flows. In such applications, SPH particles might concentrate in some regions while scattering in other areas within the computational domain. Keeping the constant smoothing length will result in a smaller number of neighbouring particles in the scatter regions and thus losing the accuracy of SPH kernel estimation. In contrast, the number of neighbouring particles would be too large in the concentrated areas, causing pairing instability, as illustrated in Section 2.3. Therefore, it is generally a good practice to design an adaptive smoothing length, which can automatically adjust depending on the level of particle concentration or density. Of various approaches proposed in the literature, the simplest approach is perhaps to link the smoothing length to the rate of change of the density (Benz, 1990):

$$\frac{dh}{dt} = -\frac{1}{\nu_d} \frac{h}{\rho} \frac{dp}{dt} \quad (44)$$

where  $\nu_d$  indicates the dimension of the problems. This rule appears to work well for most practical applications. Since each particle now has its own smoothing length, the kernel influence domain of particle  $i$  might cover particle  $j$  but not necessarily vice versa. Therefore, it is possible for particle  $i$  to exert a force on particle  $j$  without  $j$  exerting the same corresponding reaction on particle  $i$ . As a result, the momentum equation will not exactly conserve. To overcome this problem, some measures must be taken to preserve the symmetry of particle interactions. One simple approach to preserve the symmetry of particle interaction is to modify the smoothing length by taking the arithmetic mean or the average of the smoothing length of a pair of interacting particles:

$$h_{ij} = \frac{h_i + h_j}{2} \quad (45)$$

Another way to get the symmetric smoothing length is to use the geometric mean of the smoothing lengths of the pair of the interaction particles:

$$h_{ij} = \frac{2h_i h_j}{h_i + h_j} \quad (46)$$

Alternatively, one can take the maximum value of the smoothing lengths  $h_{ij} = \max(h_i, h_j)$  or minimum of the smoothing lengths  $h_{ij} = \min(h_i, h_j)$ . The kernel function can be subsequently obtained using the symmetric smoothing length  $W_{ij} = W(\mathbf{x}_i - \mathbf{x}_j, h_{ij})$ . It is noted that there are some advantages and disadvantages associated with each of the above approaches to average the smoothing length. For example, taking the arithmetic mean or maximum smoothing length tends to use more neighbouring particles, which can cause the pairing instability problem or may overly smooth out the interaction with surrounding particles. Taking geometric or minimum smoothing length, on the other hand, tends to possess less neighbouring particles. Another approach to preserve the symmetry of particle interaction is to directly use the average of kernel function values without using a symmetric smoothing length (Hernquist and Katz, 1989):

$$W_{ij} = \frac{W(\mathbf{r}_{ij}, h_i) + W(\mathbf{r}_{ij}, h_j)}{2} \quad (47)$$

Finally, it is noted that, while it is preferable to use the variable smoothing length, many SPH applications in geotechnical engineering areas do not require this update, but still achieving reasonable results (Bui et al., 2008a, Pastor et al., 2009, Wang et al., 2020, Chen and Qiu, 2012). The use of a constant smoothing length is strongly recommended for those who are new to SPH. Nevertheless, the use of symmetric smoothing length or symmetric kernel average is very important to guarantee the conservation of the momentum equation, which controls the stability and accuracy of SPH.

### 3. General SPH framework for geomechanics applications

The readers, at this point, should have developed a basic understanding of several key concepts of the SPH method. The next question would be how these concepts can be applied to solve geotechnical problems and in what capacity SPH can produce results comparable to those existing numerical methods such as FEM, besides its advantages in some specific areas. Before we start this discussion, it is important to remind the readers that, in SPH, the computational domain is represented by a set of moving particles (or material points), each of which occupies a given volume in the continuum space and carries field variables. Therefore, SPH is indeed a continuum-based numerical method, which is very similar to FEM, although SPH does not require any background mesh to solve the strong-form governing differential equations, unlike FEM. In this section, we will first revisit the continuum governing equations for a single-phase system of general geomaterials (assuming isothermal). We will then present some potential applications of SPH in this area and discuss potential issues associated with these applications as well as with SPH in general.

#### 3.1. SPH approximation of governing equations

The governing equations for solving general geomechanics and geotechnical engineering problems consist of the mass (or continuity) and momentum balance equations. The mass balance equation describes the change of material density, and thus porosity or void ratio, during the deformation process, while the momentum balance equation describes how the materials undergo deformation under external loads. These two equations are written as follows, respectively (Bui et al., 2008a):

$$\frac{d\rho}{dt} = -\rho \nabla \cdot \mathbf{v} \quad (48)$$

$$\frac{d\mathbf{v}}{dt} = \frac{1}{\rho} \nabla \cdot \boldsymbol{\sigma} + \mathbf{f}_{ext} \quad (49)$$

where  $\mathbf{v}$  is the velocity vector;  $\boldsymbol{\sigma}$  is the stress tensor, which will be defined later; and  $\mathbf{f}_{ext}$  is the external force per unit mass, including the acceleration due to the gravity. To solve the above governing equations in SPH, one needs to perform the SPH approximations for the spatial derivative terms using a set of SPH particles as discretisation of the continuum domain considered. Starting with the mass balance equation, the readers can immediately notice that SPH approximation of Equation (48) can be straightforwardly achieved by applying Equation (17) or Equation (20) for the divergence of the vector velocity field, which leads to the following equations, respectively:

$$\frac{d\rho_i}{dt} = \sum_{j=1}^N m_j (\mathbf{v}_i - \mathbf{v}_j) \cdot \nabla_i W_{ij} \quad (50)$$

$$\frac{d\rho_i}{dt} = \rho_i \sum_{j=1}^N V_j (\mathbf{v}_i - \mathbf{v}_j) \cdot \nabla_i W_{ij} \quad (51)$$

Both SPH approximations are commonly used in the literature to evaluate the density change (or porosity change) of materials and vanish for a constant velocity field. However, there is a fundamentally important difference between these two equations. Equation (50) makes use of the mass of neighbouring particles  $m_j$  to approximate the divergence of velocity, while Equation (51) involves the volume of neighbouring particles  $V_j$  and the density of the particle itself  $\rho_i$ , not neighboring particles. The use of mass limits the application of Equation (50) to problems with a homogenous material or with less density variation/discontinuity in the computational domain. On the other hand, Equation (51) can accommodate problems with high discontinuity in the density since the approximation only involves the volume of neighbouring particle  $V_j$  and the density of particle itself  $\rho_i$ . Therefore, for general geomechanics applications, Equation (51) is recommended for problems involved multi-layer soils, while Equation (50) is more suitable for soils with less discontinuity (i.e. density ratio of less than 2 (Monaghan, 2005a)). It is noted that the density change can also be evaluated using Equation (2). However, this formulation is not recommended for geomechanics applications as its accuracy is significantly affected by the boundary truncation at the free-surface boundaries. Alternatively, the SPH continuity equation can also be derived by taking the derivative of Equation (2), leading to the following continuity equations (Price, 2012):

$$\frac{d\rho_i}{dt} = \frac{1}{\vartheta_i} \sum_{j=1}^N m_j (\mathbf{v}_i - \mathbf{v}_j) \cdot \nabla_i W_{ij} \quad (52)$$

where  $\vartheta_i$  is an extra term introduced to the continuity equation to account for the variation of the smoothing length and is defined as follows:

$$\vartheta_i = \left[ 1 - \frac{\partial h_i}{\partial \rho_i} \sum_{j=1}^N m_j \frac{\partial W(\mathbf{x}_i - \mathbf{x}_j, h)}{\partial h_i} \right] \quad (53)$$

For a constant smoothing length, Equation (52) simply returns to Equation (50), suggesting that the SPH continuity equation can be simply derived from the SPH estimation of density, which was discussed in Section 2.1. It is noted that Equation (53) requires an additional law to describe the variation of smoothing length with density and Equation (44) could be adopted.

On the other hand, the SPH approximation of momentum equation can be obtained by adopting the symmetric SPH operator, i.e. Equation (23), to the  $\nabla \cdot \boldsymbol{\sigma}$  term, giving<sup>5</sup>:

<sup>5</sup> Note that an alternative popular SPH momentum equation can also be derived by applying the SPH operator (24), which produces similar results, and thus here we only focus on one of the two popular SPH equations for the momentum balance.

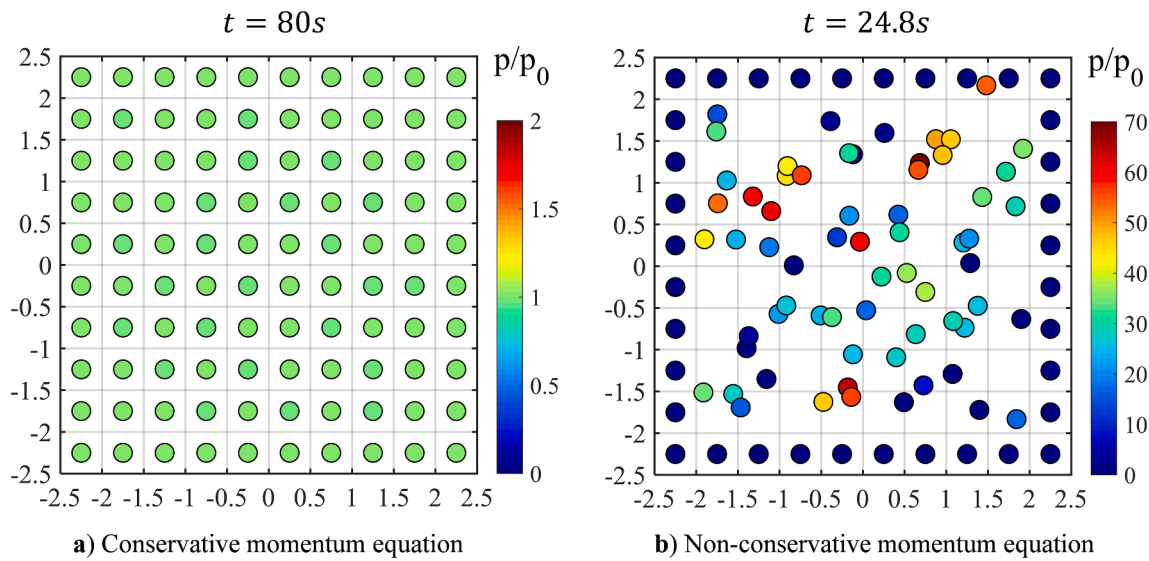


**Fig. 8.** Numerical instability in SPH caused by the non-conservative form of the momentum equation.

$$\frac{d\mathbf{v}_i}{dt} = \frac{1}{\rho} \nabla \cdot \boldsymbol{\sigma} + \mathbf{f}_{ext} \Big|_i = \sum_{j=1}^N m_j \left( \frac{\boldsymbol{\sigma}_i}{\rho_i^2} + \frac{\boldsymbol{\sigma}_j}{\rho_j^2} \right) \cdot \nabla_i W_{ij} + \mathbf{f}_{ext} \quad (54)$$

The readers would wonder why we apply the “bad” SPH operator, which has poor results of SPH approximation for the gradient of a constant function, to approximate the momentum equation, instead of using a “good” SPH operator such as Equation (20) or Equation (21). This is one of the interesting features of SPH as it appears that the “good” SPH operators do not reproduce the SPH momentum equation that exactly conserves both total linear and angular momenta, while the “bad” SPH operator does well in this aspect. The conservation of total linear momentum of the above governing equation can be proven by taking the derivative of the total momentum of the entire system (Price, 2012):

$$\frac{d}{dt} \sum_i m_i \mathbf{v}_i = \sum_i \sum_j m_i m_j \left( \frac{\boldsymbol{\sigma}_i}{\rho_i^2} + \frac{\boldsymbol{\sigma}_j}{\rho_j^2} \right) \cdot \nabla_i W_{ij} = 0 \quad (55)$$

where the double summation is equal to zero because  $\nabla_i W_{ij} = -\nabla_j W_{ij}$ . Similarly, the conservation of the total angular momentum can also be proven in a similar manner by:

$$\begin{aligned} \frac{d}{dt} \sum_i \mathbf{x}_i \times m_i \mathbf{v}_i &= \sum_i m_i \left( \frac{d\mathbf{x}_i}{dt} \times \mathbf{v}_i \right) + \sum_i m_i \left( \mathbf{x}_i \times \frac{d\mathbf{v}_i}{dt} \right) \\ &= \sum_i \sum_j m_i m_j \left\{ \mathbf{x}_i \times \left[ \left( \frac{\boldsymbol{\sigma}_i}{\rho_i^2} + \frac{\boldsymbol{\sigma}_j}{\rho_j^2} \right) \cdot \nabla_i W_{ij} \right] \right\} = 0 \end{aligned} \quad (56)$$

which again equals zero because of the symmetric features of the kernel function.

On the other hand, if one prefers to use a “good” SPH operator such as Equation (20), the following momentum equation can be obtained:

$$\frac{d\mathbf{v}_i}{dt} = \sum_j m_j \left( \frac{\boldsymbol{\sigma}_j - \boldsymbol{\sigma}_i}{\rho_i \rho_j} \right) \cdot \nabla_i W_{ij} = 0 \quad (57)$$

which guarantees the vanishing of gradient of a constant stress field. Unfortunately, the above equation does not conserve both linear and angular momenta, and thus failing to maintain the stability of numerical simulations. To demonstrate the importance of using the momentum equation that conserves linear and angular momenta, we repeat the test conducted in Section 2.3 using the Cubic-spline kernel function ( $h = 1.2\Delta x$ ) for two different momentum Equations (56) and (57). The

results are illustrated in Fig. 8. It can be seen that Equation (56) helps to keep the simulation remains stable with small perturbation thanks to its capability to conserve the total momentum, while the non-conservative form (57) caused particles to clump and penetrating the boundary due to the unbalance force in the system. To the best of our knowledge, we have not yet achieved an SPH formulation for the momentum equation that exactly conserves both linear and angular momenta while maintaining exact derivatives. And this conclusion extends to all existing particle numerical methods. Finally, to close the above governing equations, one needs a material constitutive model to compute stresses, and this topic is discussed in the next section.

### 3.2. Material constitutive models

Constitutive model is a core component of a computational framework used to describe how a material behaves under external loads. Early applications of SPH in the field of geomechanics (Bui et al., 2006a, Bui et al., 2005, Bui and Fukagawa, 2005, Bui et al., 2007, Maeda et al., 2006) explored the traditional SPH approach developed for computational fluid mechanics (CFD) (Monaghan, 1994) and elastic solid (Monaghan, 1994, Gray et al., 2001, Randles and Libersky, 1996, Libersky et al., 1993, Randles et al., 1995), hereafter referred to as CFD approach. In this approach, the total stress tensor was decomposed into isotropic and shear components, and different constitutive laws were used for these components. A more rigorous approach was subsequently developed (Bui et al., 2008a, Bui, 2007, Pastor et al., 2009), in which advanced constitutive models based on plasticity theory were adopted, and successfully describe and simulate a wide range of applications in geomechanics (Bui et al., 2008a, Bui et al., 2014, Bui et al., 2008b, Nguyen et al., 2017a, Neto and Borja, 2018, Bui and Nguyen, 2017, Wang et al., 2019, Tran, 2019a, Zhao et al., 2019, Tran et al., 2019, Wang et al., 2020, Peng et al., 2015, Sheikh et al., 2020, Chen and Qiu, 2012). In this section, a brief description of several constitutive modelling approaches for geomaterials and their SPH applications are presented.

#### 3.2.1. CFD-based approaches for modelling geomaterials

**3.2.1.1. A simple elastic-perfectly plastic model for soils.** In the earlier applications of SPH to geomechanics (Bui et al., 2006a, Bui et al., 2007, Bui et al., 2006b), a constitutive model for cohesive-frictional soils was formulated following the standard CFD approach, in which the stress tensor is decomposed into the isotropic pressure ( $p$ ) and the deviatoric

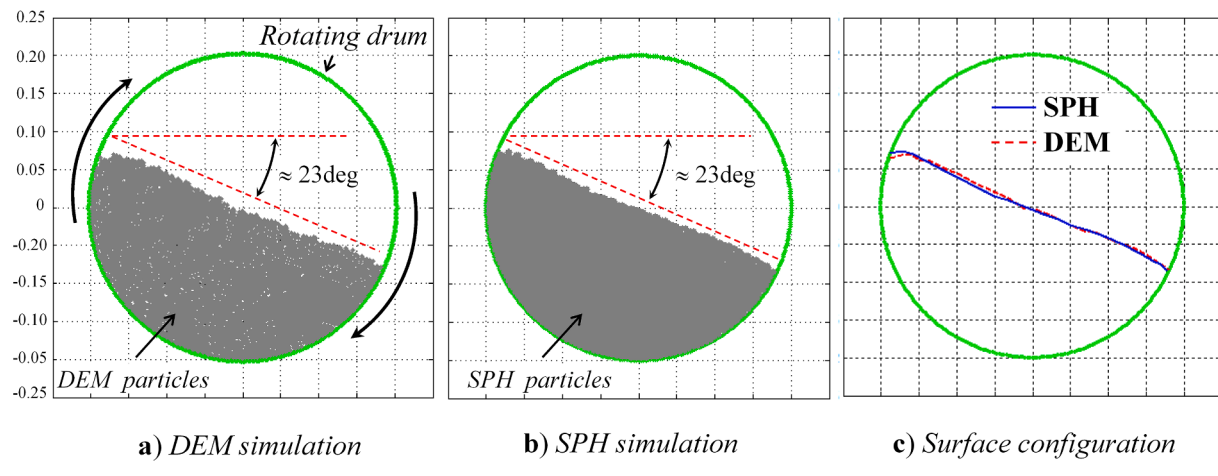


**Fig. 9.** A comparison between SPH and DEM simulations of granular flows in a rotating drum using the simple elastic-perfectly plastic constitutive model, after (Bui et al., 2006b).

stress ( $\sigma$ ):

$$\sigma = p\mathbf{I} + \mathbf{s} \quad (58)$$

where  $\mathbf{I}$  is the unit tensor. The isotropic pressure is computed using an equation of state (EOS), which is often formulated as a function of density change and sound speed (Randles and Libersky, 1996, Monaghan, 2012, Gray et al., 2001). For geomechanics applications, Bui et al. (Bui et al., 2006a, Bui et al., 2007) proposed the following formulation, following the general Hooke's law:

$$p = K \frac{\Delta V}{V_0} = K \left( \frac{\rho}{\rho_0} - 1 \right) \quad (59)$$

where  $\Delta V/V_0$  is the volumetric strain produced by the isotropic pressure component;  $K$  is the elastic bulk modulus of the materials; and  $\rho_0$  is the initial density. On the other hand, the deviatoric shear stress can be estimated using the general Hooke's law for elastic materials, which takes the following form:

$$\dot{\mathbf{s}} = 2G \left( \dot{\mathbf{\epsilon}} - \frac{1}{3} \mathbf{I} \dot{\mathbf{e}}_v \right) \quad (60)$$

where  $G$  is the elastic shear modulus;  $\dot{\mathbf{\epsilon}} = \frac{1}{2} [\nabla \mathbf{v} + \mathbf{v} \nabla]$  is the strain rate tensor;  $\dot{\mathbf{e}}_v$  is the volumetric component of the strain rate tensor; and the accent-dot indicates the time derivative of the vector/tensor quantities. For large deformation analyses, an invariant stress rate with respect to rigid-body rotation is required, and this can be achieved by adopting the Jaumann stress-rate, leading to:

$$\dot{\mathbf{s}}' = \dot{\mathbf{s}} - \boldsymbol{\omega} \cdot \dot{\mathbf{s}} + \dot{\mathbf{s}} \cdot \boldsymbol{\omega} \quad (61)$$

where  $\dot{\boldsymbol{\omega}} = \frac{1}{2} [\nabla \boldsymbol{\omega} - \boldsymbol{\omega} \nabla]$  is the spin-rate tensor. The shear stresses obtained from the above equation increase linearly with the increasing shear strain, and thus cannot capture the plastic response of geomaterials. To describe this behaviour, a simple approach is to restrict the development of shear stresses when the materials enter their plastic flow regime without actually solving the plastic deformation (Liberky et al., 1993). This treatment somewhat replicates the perfectly-plastic response of the materials for the shear stress components, but does not invoke the plastic strain components. The plastic regime for general soils can be determined by the well-known Mohr-Coulomb failure criterion:

$$\tau_f = c + p \tan \phi \quad (62)$$

where  $\tau_f = \left( \frac{3}{2} s : s \right)^{1/2}$  is the maximum shear stress at failure;  $c$  is the soil cohesion; and  $\phi$  is the friction angle. Therefore when the soil enters its

plastic flow regime, the shear stress components are scaled back to the yield surface defined by Equation (62). The application of the above constitutive model in SPH to simulate granular materials was successfully demonstrated in previous works (Bui et al., 2006a, Bui et al., 2007, Bui et al., 2006b). For example, the results predicted by this model showed comparable results to those obtained by the Discrete Element Method (DEM), which is well-suited for granular materials, when being applied to simulate a granular material in a rotating drum, as shown in Fig. 9.

**3.2.1.2.  $\mu(I)$ -rheological constitutive model.** The  $\mu(I)$ -rheological model originally proposed by Jop et al. (Jop et al., 2006b) is one of the most commonly used and widely validated rheological models, developed to capture the rate-dependent and inertial effect of granular materials in the dense flow regime. It was derived based on the Bingham constitutive relation for non-Newtonian fluids, which assumes the materials behave as a rigid body or stiff elastic response before yielding and then quickly reaching their plastic flow behaviour (i.e. critical state after yielding). To establish the constitutive model of this type, it is convenient to separate the stress tensor ( $\sigma$ ) into an isotropic pressure ( $p$ ) and viscous shear stress tensor ( $\tau$ ), such that  $\sigma = p\mathbf{I} + \tau$ . The  $\mu(I)$ -rheological model then defines the viscous shear stress as a function of total strain-rate, as follows:

$$\tau = 2\eta \dot{\epsilon}, \quad (63)$$

$$\eta = \frac{\mu(I)p}{\sqrt{2(\dot{\epsilon} : \dot{\epsilon})}} \quad (64)$$

$$\mu(I) = \mu_s + \frac{\mu_2 - \mu_s}{I_0/I + 1} \quad (65)$$

where  $\eta$  is an effective viscosity;  $\dot{\epsilon}$  is the total strain-rate tensor;  $\mu$  is a frictional function dependent on the inertial number  $I = d_s \sqrt{2(\dot{\epsilon} : \dot{\epsilon})}/\sqrt{p/\rho_s}$  with  $d_s$  being the grain diameter,  $\rho_s$  being the solid density;  $\mu_2$  and  $I_0$  are both materials constants with  $\mu_2$  being the critical friction angle at very high  $I$ ; and  $\mu_s$  is the static friction coefficient, corresponding to the state of no plastic flow.

It can be seen from the above constitutive model that the effective viscosity ( $\eta$ ) diverges to infinity when the shear strain rate approaches zero (i.e.,  $\dot{\epsilon} \rightarrow 0$ ). This divergence ensures the material behaviour is rigid or very stiff when the strain rate is very small (or at the static condition) and thus guaranteeing the existence of a yield criterion. The yielding condition can be inferred from the above model by considering the strain rate tensor in the limit of zero (i.e.,  $\dot{\epsilon} \rightarrow 0$ ). Under this condition, the second component of  $\mu(I)$  will approach zero as  $(I_0/I)$  goes to infinity.

This suggests that, under static condition,  $\mu(I) = \mu_s$ , which defines a yielding threshold above which yielding occurs. Accordingly, the following yield criterion, which takes the form of the Drucker Prager-like criterion, can be defined (Jop et al., 2006a):

$$|\boldsymbol{\tau}| \leq \mu_s p \quad \text{where } |\boldsymbol{\tau}| = \sqrt{0.5(\boldsymbol{\tau} : \boldsymbol{\tau})} \quad (66)$$

To complete the description of this constitutive relation, one needs to define the isotropic pressure and Equation (59) can be adopted. Alternatively, the following equation of state, which is commonly used in the SPH context to model quasi-compressible fluid, can be used to compute the isotropic pressure:

$$p = c^2(\rho - \rho_0), \quad (67)$$

where  $c$  is the speed of sound,  $\rho$  is the density of an SPH particle, and  $\rho_0$  is the reference density of the material. Finally, it is noted that when incorporating this model in the above SPH framework to simulate granular materials, to avoid unphysical behaviour, the shear component of the stress tensor should be set to zero for negative pressure value. In addition, the initial strain rate tensor should be set close to zero (e.g.  $10^{-7}$ ) as zero strain rates can result in mathematically undefined behaviour. For details of these treatments, the readers are recommended to our recent work in (Yang et al., 2021).

The application of CFD approach to model geomaterials using SPH has gained successes in modelling granular or debris flows (Bui et al., 2006a, Bui et al., 2007, Bui et al., 2006b, Minatti and Paris, 2015, Hurley and Andrade, 2017), where the materials are considered to either be fluid-like materials (i.e. liquefied materials) or have reached its critical state. The key advantage of this approach is that it is relatively simple and can be easily implemented in any existing SPH open-source code. However, the key drawback of this type of constitutive model is that it cannot describe complex responses of geomaterials, including the hardening or/and softening processes, before reaching the critical state of soils. For this reason, advanced constitutive models are required, and this will be covered in the next section.

### 3.2.2. General elastoplastic constitutive modelling approach for modelling geomaterials

This type of constitutive model was built on the basis of continuum plasticity theory, in which a single mathematical relationship that relates the stress-increment to the strain-increment was established for a homogenous representative volume element (or an SPH particle) which is assumed to remain homogenous. A yield surface and a plastic potential function (or dilatancy rule) are then used to control the hardening or/and softening processes commonly observed in the materials. In principle, any existing elastoplastic constitutive models developed for FEM can be implemented in SPH and sharing the same procedure for updating stresses. Unlike the CFD approach, such as the  $\mu(I)$ -rheological model, which derives the stress tensor from instantaneous density and strain-rate, the general elastoplastic approach evolves the stress tensor over time using a unique stress-strain relationship that relates the stress-increment to the strain-increment. It is assumed that for an elastoplastic material, the total strain-increment tensor ( $d\boldsymbol{\epsilon}$ ) is decomposed into elastic ( $d\boldsymbol{\epsilon}_e$ ) and plastic ( $d\boldsymbol{\epsilon}_p$ ) components:

$$d\boldsymbol{\epsilon} = d\boldsymbol{\epsilon}_e + d\boldsymbol{\epsilon}_p \quad (68)$$

The stress increment is then calculated from the generalized Hooke's Law:

$$d\boldsymbol{\sigma} = \mathbf{D}^e : (d\boldsymbol{\epsilon} - d\boldsymbol{\epsilon}_p) = \mathbf{D}^{ep} : d\boldsymbol{\epsilon} \quad (69)$$

where  $\mathbf{D}^e$  is the elastic stiffness matrix and  $\mathbf{D}^{ep}$  is an elasto-plastic matrix (Bui et al., 2008a).

A yield function  $f(\boldsymbol{\sigma}, \kappa)$  in the form of stress tensor (or more often stress invariants) and variable  $\kappa$ , which controls the hardening/softening rule of the yield function, is then required to determine when the plastic

deformation takes place. When the yielding condition is met, i.e.  $f(\boldsymbol{\sigma}, \kappa) = 0$ , the plastic strain increment can be computed using the general plastic flow rule:

$$d\boldsymbol{\epsilon}_p = d\lambda \frac{\partial g(\boldsymbol{\sigma})}{\partial \boldsymbol{\sigma}} \quad (70)$$

where  $d\lambda$  is a positive plastic-multiplier and  $g(\boldsymbol{\sigma})$  is the plastic potential function, which controls the direction of plastic strain increments. If the plastic potential function is assumed to coincide with the yield surface, the model is known as associated plastic flow rule; otherwise, it is called non-associated flow plastic rule. It is noted that, in several critical state soil constitutive models (Dafalias and Manzari, 2004, Jefferies, 1993), the plastic potential function is not explicitly defined; instead, a dilatancy rule which defines the ratio between the volumetric to deviatoric plastic strain increments is often adopted.

To complete the definition of the above constitutive model, one needs to define the plastic multiplier (or to establish an elasto-plastic matrix), and this can be achieved by using the following complementary conditions:

$$d\lambda \geq 0, \quad f(\boldsymbol{\sigma}, \kappa) \leq 0, \quad d\lambda f(\boldsymbol{\sigma}, \kappa) = 0 \quad \text{and} \quad d\lambda df(\boldsymbol{\sigma}, \kappa) = 0 \quad (71)$$

Such that the stress of the material can be advanced as follows:

$$\boldsymbol{\sigma}_{t+1} = \boldsymbol{\sigma}_t + \mathbf{D}^{ep} : d\boldsymbol{\epsilon} \quad (72)$$

There exist several approaches in the literature for the computation of the plastic multiplier, and updating stresses (Pietruszczak, 2010, Simo and Hughes, 2006, Borja, 2013). Here, we present two simple but effective methods to compute the plastic multiplier and updating stresses for a constitutive model, which has been proven to work well in SPH for geomechanics applications, thanks to the small time-step requirement in the fully explicit SPH approach.

**3.2.2.1. A fully explicit approach to update a constitutive model.** The fully explicit stress updating approach is perhaps the simplest method used to advance the stress update in SPH. This method makes use of all information of stresses and internal variables at the previous time step ( $\boldsymbol{\sigma}_t, \kappa_t$ ) to update the stresses and internal variables for the current time step ( $\boldsymbol{\sigma}_{t+1}, \kappa_{t+1}$ ). For this reason, this approach is also referred to as the forward-Euler method. This method requires the plastic multiplier to be explicitly defined and this can be achieved from the following so-called consistency condition (i.e.  $df = 0$ ):

$$df(\boldsymbol{\sigma}, \kappa) = \frac{\partial f(\boldsymbol{\sigma}, \kappa)}{\partial \boldsymbol{\sigma}} : d\boldsymbol{\sigma} + \frac{\partial f(\boldsymbol{\sigma}, \kappa)}{\partial \kappa} d\kappa = 0 \quad (73)$$

Accordingly, any existing elasto-plastic constitutive models, which were previously developed for FEM, can be implemented in SPH through the above procedure. Here, we present the simplest case for an elasto-plastic constitutive model following the Drucker-Prager criterion, which takes the following general form:

$$f(I_1, J_2, \kappa) = \alpha_\phi(\kappa)I_1 + \sqrt{J_2} - k_c(\kappa) = 0 \quad (74)$$

where  $I_1$  and  $J_2$  are the first and second invariants of the stress tensor;  $\alpha_\phi$  and  $\beta_\phi$  are Drucker-Prager constants related to the Coulomb internal friction angle ( $\phi$ ); and  $c(\kappa)$  is related to soil cohesion and is assumed to be a function of plastic strain. In 3D conditions,  $\alpha_\phi$  and  $k_c$  are calculated as, respectively:

$$\alpha_\phi(\kappa) = \frac{2\sin\phi(\kappa)}{\sqrt{3}(3 - \sin\phi(\kappa))} \quad \text{and} \quad k_c(\kappa) = \frac{6c(\kappa)\cos\phi(\kappa)}{\sqrt{3}(3 - \sin\phi(\kappa))} \quad (75)$$

To describe the softening process, involving the reduction of soil friction and cohesion during the post-failure process, the following non-linear softening laws can be adopted (Zabala and Alonso, 2011):

$$\phi(\kappa) = \phi_r + (\phi_p - \phi_r)e^{-\eta_\phi \kappa} \quad (76)$$

$$c(\kappa) = c_r + (c_p - c_r) e^{-\eta_c \kappa} \quad (77)$$

where the subscripts  $p$  and  $r$  represent the peak and residual strengths of the material, respectively;  $\eta_\phi$  and  $\eta_c$  are the softening coefficients controlling the rate of shear strength degradation of the material; and the variable  $\kappa$  controlling the softening behaviour can be defined from the equivalent plastic shear strain tensor as follows:

$$d\kappa = \sqrt{\frac{2}{3} d\epsilon^p : d\epsilon^p} \quad (78)$$

where  $\epsilon^p$  is the deviatoric plastic strain tensor. The plastic flow function can be simply defined as follow:

$$g = \alpha_\psi I_1 + \sqrt{J_2} \quad (79)$$

where  $\alpha_\psi$  is a Drucker-Prager constant, which can be determined using Equation (75) with  $\phi$  being replaced by the dilation angle  $\psi$ . In addition, it is well-known that the value of dilation angle in granular materials evolves with the material state and tends to vanish at a critical state corresponding to zero volume change with material deformation (Bolton, 1986). To reproduce this mechanism towards the critical state, the dilation angle  $\psi$  can be related to the development of accumulated plastic displacement by an exponential function as follows:

$$\psi = \psi_0 e^{-s_f |\epsilon^p|} \quad (80)$$

where  $\psi_0$  is the initial dilation angle and  $s_f$  is the scale factor. Equation (80) implies that  $\psi = \psi_0$  at the initial state and gradually approaches zero as the accumulated plastic strain develops. The rate of change of  $\psi$  toward zero is controlled by the scale factor  $s_f$ .

With the yield and plastic functions explicitly defined, the plastic multiplier can be obtained from the consistency condition as follows:

$$d\lambda = \frac{\frac{\partial f}{\partial \sigma} : \mathbf{D}^e : d\epsilon}{\frac{\partial f}{\partial \sigma} : \mathbf{D}^e : \frac{\partial g}{\partial \sigma} + \frac{\partial f}{\partial \kappa} \sqrt{\frac{2}{3} \frac{\partial g}{\partial \sigma} : \frac{\partial g}{\partial \sigma}}} \quad (81)$$

Finally, by substituting  $d\lambda$  back to Equation (69), the following general elastoplastic incremental stress-strain relation can be established for the above constitutive model:

$$d\sigma = \left( \mathbf{D}^e - \frac{\mathbf{D}^e : \frac{\partial g}{\partial \sigma} \otimes \frac{\partial f}{\partial \sigma} : \mathbf{D}^e}{\frac{\partial f}{\partial \sigma} : \mathbf{D}^e : \frac{\partial g}{\partial \sigma} + \frac{\partial f}{\partial \kappa} \sqrt{\frac{2}{3} \frac{\partial g}{\partial \sigma} : \frac{\partial g}{\partial \sigma}}} \right) : d\epsilon = \mathbf{D}^{ep} : d\epsilon \quad (82)$$

For large deformation analyses, an invariant stress rate with respect to the rigid-body rotation must be enforced to the stress-strain relation. Here, the Jaumann stress-rate formulation is adopted:

$$\dot{\sigma}^J = \dot{\sigma} - \dot{\omega} \cdot \sigma + \sigma \cdot \dot{\omega} \quad (83)$$

And thus, the rate-constitutive equation then becomes:

$$\dot{\sigma} = \mathbf{D}^{ep} : \dot{\epsilon} - \dot{\omega} \cdot \sigma + \sigma \cdot \dot{\omega} \quad (84)$$

It is noted that the above treatment for large deformation is only acceptable for a small time interval or a small rotation within a given time interval and this is usually satisfied in SPH due to its strict requirement of a very small time interval to integrate the fully dynamic governing equations. Furthermore, because of the direct procedure to obtain  $\mathbf{D}^{ep}$  from the current stress state, the fully explicit approach often results in the stress states, which are gradually drifting away from the yield surface, and thus violating conditions (71). To avoid this issue, stress corrections are required and the readers are referred to (Bui et al., 2008a) for the detailed procedure for this stress correction and its illustration in SPH. The above stress-strain relation is used to govern the behaviour of SPH particles and stress update for every particle is carried out each time increment following Algorithm 1.

#### Algorithm 1. (Fully-explicit stress updating procedure)

- 
- 1 Given strain-rate and spin-rate tensors  $\dot{\epsilon}$  &  $\dot{\omega}$  (or their increments  $d\epsilon = \dot{\epsilon}dt$  and  $d\omega = \dot{\omega}dt$ ) and other state variables at  $t$ :
  - 2 Check if yielding takes place by computing:  $f(\sigma_t, \kappa_t)$   
If  $f(\sigma_t, \kappa_t) < 0$  then  
Proceed to Step 3  
Else  $f(\sigma_t, \kappa_t) \geq 0$  the loading step is elasto-plastic  
Proceed to Step 4  
End
  - 3 Elastic stress update:  
 $d\sigma_{t+1} = \mathbf{D}^e : d\epsilon - d\omega \cdot \sigma_t + \sigma_t \cdot d\omega \sigma_{t+1} = \sigma_t + d\sigma_{t+1}$
  - 4 Elastoplastic stress update:  
$$\mathbf{D}^{ep} = \left( \mathbf{D}^e - \frac{\mathbf{D}^e : \frac{\partial g}{\partial \sigma} \otimes \frac{\partial f}{\partial \sigma} : \mathbf{D}^e}{\frac{\partial f}{\partial \sigma} : \mathbf{D}^e : \frac{\partial g}{\partial \sigma} + \frac{\partial f}{\partial \kappa} \sqrt{\frac{2}{3} \frac{\partial g}{\partial \sigma} : \frac{\partial g}{\partial \sigma}}} \right) \sigma_t + \sigma_t \cdot d\omega \sigma_{t+1} = \sigma_t + d\sigma_{t+1}; \epsilon_{t+1}^p = d\sigma_{t+1} = \mathbf{D}^{ep} : d\epsilon - d\omega$$
  
 $\epsilon_t^p + d\epsilon^p; \& \kappa_{t+1} = \kappa_t + d\kappa$   
EXIT the algorithm
- 

**3.2.2.2. A semi-implicit approach to update a constitutive model.** Explicit stress return algorithm usually requires the determination of the intersection between the stress incremental vector and the yield surface, so that elasto-plastic stress-strain relation can be appropriately applied when yielding occurs. As it is an explicit approach, error accumulates leading to drifting of the stress point from the yield surface and affect the accuracy of the stress update process. An alternative approach to mitigate the stresses drift from the yield surface and to avoid error accumulation is to adopt a non-direct approach to define the plastic multiplier (or the elastoplastic matrix). The basic idea of this approach starts from Equation (69), which combines with Equation (70) can be written as follows:

$$d\sigma = \mathbf{D}^e : d\epsilon - \mathbf{D}^e : \left( d\lambda \frac{\partial g(\sigma)}{\partial \sigma} \right) \quad (85)$$

The first term on the right-hand side of Equation (85) is an elastic stress increment  $d\sigma^e$  caused by the entire strain increment  $d\epsilon$ , while the second term,  $d\sigma^p$ , is the stress relaxation due to the plastic deformation. The difference between these two quantities gives rise to the correct stress applied on the material point (or RVE). Therefore, if  $d\sigma$  is the correct stress increment required to produce a correct stress meeting the condition of  $f(\sigma, \kappa) = 0$ ,  $d\sigma^e$  can be thought as an elastic trial stress and  $d\sigma^p$  is a plastic corrector stress, which is dependent on the plastic multiplier  $d\lambda$  and the gradient of the loading surface  $\partial g(\sigma)/\partial \sigma$  at the correct stress state on the correct yield surface. The key question now is how these quantities are determined to give a closed-form solution for  $d\sigma$  to complete the above stress update. The plastic multiplier can be determined by considering the Taylor-series expansion of the yield function at the correct stress state around the trial stress state up to the second-order accuracy, we have:

$$f(\sigma, \kappa) = f^{trial} - \frac{\partial f(\sigma)}{\partial \sigma} : d\sigma^p + \frac{\partial f(\sigma)}{\partial \kappa} dk = 0 \quad (86)$$

$$d\lambda = \frac{f^{trial}}{\frac{\partial f(\sigma)}{\partial \sigma} : \mathbf{D}^e : \frac{\partial g(\sigma)}{\partial \sigma} + \frac{\partial f(\sigma)}{\partial \kappa} \sqrt{\frac{2}{3} \frac{\partial g(\sigma)}{\partial \sigma} : \frac{\partial g(\sigma)}{\partial \sigma}}} \quad (87)$$

By substituting the expression of  $d\sigma^p$  and the definition of  $dk$  from Equation (78) into the above expression of the correct yield function and solving for  $d\lambda$ , one can get:

It can be seen from the above equations that the closed-form solution for  $d\sigma$  can be achieved if the gradients  $\partial f(\sigma)/\partial \sigma$  and  $\partial g(\sigma)/\partial \sigma$  are correctly determined. However, the final stress state is unknown due to the fact that the corrector stress path (i.e. from the trial stress to the correct stress states) is unknown. Therefore iterations are required and the algorithm is considered a fully implicit one in such cases. This is the

basis of several well-known stress return mapping algorithms, which aim to minimise errors associated with the determination of the gradients  $\partial f(\sigma)/\partial \sigma$  and  $\partial g(\sigma)/\partial \sigma$  (Simo and Hughes, 2006; Pietruszczak, 2010; Borja, 2013). Here, given the requirement of a very small time step in SPH to solve its fully dynamic SPH governing equations in a fully explicit time integration scheme (Bui et al., 2008a), the strain increment over each time step in SPH is also very small. For this reason, instead of performing iteration to obtain the correct  $\partial f(\sigma)/\partial \sigma$  and  $\partial g(\sigma)/\partial \sigma$ , which is usually complicated, we take the gradients of the loading surface and plastic potential at the trial stress for the calculation. This can be considered appropriate within the SPH context thanks to very small time steps used to ensure the stability of the time integration. And because of this assumption, the stress updating procedure presented in this section is called the semi-implicit stress return mapping algorithm (Nguyen and Bui, 2020; Nguyen and Housby, 2008; De Borst et al., 2012), which has been previously demonstrated to work well within the context of SPH (Tran et al., 2019; Wang et al., 2019; Wang et al., 2020) or FEM with relatively small strain increment (Le et al., 2018; Le et al., 2019). Once the plastic multiplier is determined, the stress increment  $d\sigma$  required for the stress update can be obtained and Jaumann stress rate is again adopted to keep the objective measure of stresses with respect to the rigid body rotation. The details of this stress updating algorithm is presented in Algorithm 2.

#### Algorithm 2. (Semi-explicit stress updating procedure)

- 
- 1 Given strain-rate and spin-rate tensors ( $\dot{\epsilon}$  &  $\dot{\omega}$ ) or their increments  $d\dot{\epsilon} = \dot{\epsilon}_{t+1}$  and  $d\dot{\omega} = \dot{\omega}_{t+1}$ , and other state variables at  $t$ , evaluate elastic trial stress for plastic loading:  
Elastic trial stress increment:  $d\sigma_{t+1}^{trial} = D^e : d\dot{\epsilon} - d\sigma \cdot \dot{\epsilon}_t + \sigma_t d\dot{\omega}$
  - Trial stress:  $\sigma_{t+1}^{trial} = \sigma_t + d\sigma_{t+1}^{trial}$   
Trial internal variable:  $\kappa_{t+1} = \kappa_t$   
Trial yield function:  $f_{t+1}^{trial}(\sigma_{t+1}^{trial}, \kappa_{t+1})$
  - 2 Check if plastic yielding occurs by computing:  $f_{t+1}^{trial}(\sigma_{t+1}^{trial}, \kappa_{t+1})$   
If  $f_{t+1}^{trial}(\sigma_{t+1}^{trial}, \kappa_{t+1}) < 0$  then  
Proceed to Step 3  
Else  $f_{t+1}^{trial}(\sigma_{t+1}^{trial}, \kappa_{t+1}) \geq 0$  the loading step is elasto-plastic  
Proceed to Step 4  
End
  - 3 Elastic stress update:  
 $\sigma_{t+1} = \sigma_{t+1}^{trial}; \epsilon_{t+1}^p = \epsilon_t^p; \& \kappa_{t+1} = \kappa_t$
  - 4 Perform stress corrector:  

$$d\lambda = \frac{f_{t+1}^{trial}}{\left| \frac{\partial f}{\partial \sigma} \right|_{trial} : D^e : \left| \frac{\partial g}{\partial \sigma} \right|_{trial} + \left| \frac{\partial f}{\partial \kappa} \right|_{trial} \sqrt{\left| \frac{2}{3} \frac{\partial g}{\partial \kappa} \right|_{trial} : \left| \frac{\partial g}{\partial \sigma} \right|_{trial}} \sigma_{t+1} = \sigma_t + d\sigma_{t+1}; \epsilon_{t+1}^p = \epsilon_t^p + d\epsilon^p; \& \kappa_{t+1} = \kappa_t + d\kappa$$
- EXIT the algorithm
- 

#### 3.2.3. A double-scale constitutive modelling approach: Capturing pre- and post-localisation behaviour at the particle level

**3.2.3.1. Localised failure and constitutive modelling.** Classical continuum constitutive models (i.e. Section 3.2.2) are written for a unit volume element, thanks to the assumption of homogeneous deformation, and hence can be used for a volume element of any size. In relation to the SPH, the particle size does not affect the behaviour of the constitutive model it uses, given homogenous deformation over the volume of the particle is the implicit assumption. However, localised failure in the form of fracture or localisation band makes the assumption of homogeneous deformation that continuum constitutive models are based on invalid. The deformation and nonlinear processes inside the localisation band dominate the inelastic response of the material, while the material outside this band usually undergoes elastic or negligible inelastic

deformation. The definition of a Representative Volume Element (RVE) ceases to exist, given the thickness of localisation band is usually very small and mainly governed by the microstructure of the materials (such as grain size) and most importantly because of very high deformation gradients across the width of the localisation band. In such cases of localised failure, the behaviour of the volume element crossed by the localisation band is governed by behaviour of the localisation band, its size and orientation, in addition to the size and behaviour of the zone outside the band. A length scale related to the thickness of the localisation band is involved in the behaviour. Classical continuum models do not possess such a length scale and hence fails to correctly describe post-localisation behaviour. In the analysis of Boundary Value Problems (BVPs) involving localised failure, the material stability in such cases is lost, leading to the dependence of numerical solutions on the discretisation (Neilsen and Schreyer, 1993). Without enhancements to account for localised failure and behaviour at the scale of the localisation band (mesoscale), these classical continuum models cannot give correct and converging numerical solutions upon refinement of the discretisation and this is a common issue with any numerical method, including the SPH. A range of different available enhancements can be selected, such as higher-order theories (Pijaudier-Cabot and Bažant, 1987; Chen and Schreyer, 1987; Bažant, 1991; Vardoulakis and Aifantis, 1991; Borst and Pamin, 1996), or simply artificial scaling of constitutive behaviour using smeared crack/deformation approach (Cedolin and Bažant, 1980; Crook et al., 2006; Zabala and Alonso, 2011). However, they are not always suitable in terms of versatility, simplicity and computational efficiency for SPH simulations of complex failure processes that usually involve the activation and deactivation of several cracks or localisation bands (Nguyen et al., 2016; Nguyen and Bui, 2020). In addition, higher-order theories require the discretisation at the scale of the localisation band to capture very high gradients of deformation across the thickness of the localisation band, inducing high computational costs and restricting the scale of their practical applications (Nguyen and Bui, 2020).

A generic and systematic enrichment based on the mechanism of localised failure that can be applied to any existing constitutive model and particularly suitable for SPH is presented in this sub-section, based on our earlier developments (Nguyen et al., 2016; Nguyen and Bui, 2020). The key idea is to consider the case of a volume element much larger than the thickness of the localisation band, given the thickness of this band is very small compared to the size of the RVE before localisation. This is opposite to the idea of higher-order continuum theories in which the size of the elements (or particles) must be smaller than the thickness of the localisation band to capture in great details high gradients of deformation across the band. In our approach, the deformation can be reasonably assumed to be homogeneous inside and outside the band. However, the strain is discontinuous across the boundary of the band and there exist two zones possessing different behaviours in a volume element considered to account for inelasticity mainly inside the localisation band and unloading behaviour outside the band (Fig. 10). The averaged strain rate, illustrated in Fig. 10c as a black horizontal line, is still needed to interface with numerical methods for the solution of the governing equations. However, it is a result of behaviours inside and outside the localisation band and corresponding length scales (thickness of the localisation band and size of the volume element containing it). For that purpose, the structure of constitutive model is enriched to accommodate mesoscale details of the localisation band, including its orientation, thickness and behaviour (Fig. 10).

**3.2.3.2. A general formulation for an SPH particle with an embedded localisation band.** Given the fact that the localisation band thickness is usually very small, it is physically reasonable and computationally efficient to consider the case of a volume element represented by an SPH particle crossed by a localisation band (Fig. 10b). The location of the band inside an SPH particle is not relevant in the current constitutive

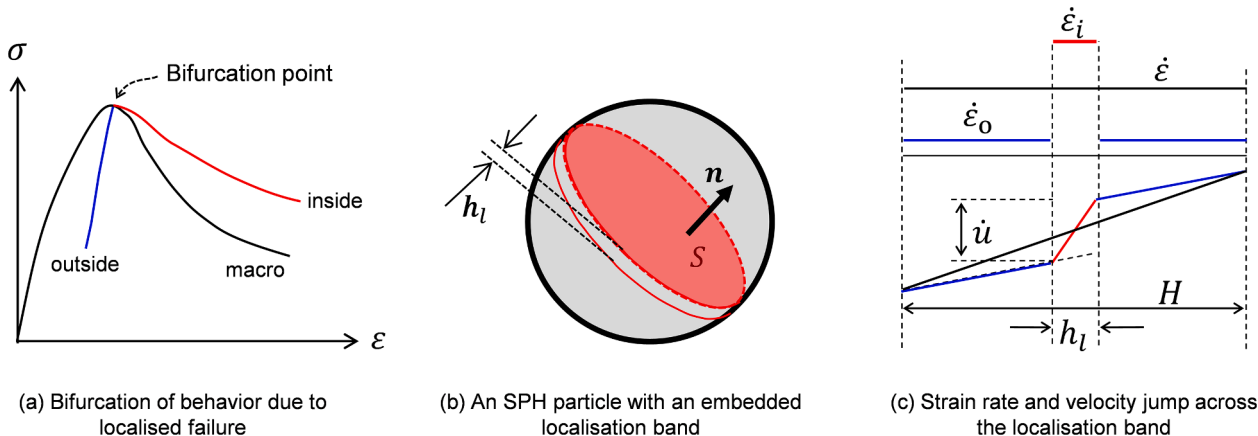


**Fig. 10.** An SPH particle crossed by a localisation band of thickness  $h_l$ : constitutive behaviour and strain profile across the localisation band (illustrated in 1D for simplicity).

structure and this helps reduce the amount of details needed at the particle level. In conjunction with this simplification should be approaches to analyse and quantify data so that these data obtained at grain or meso scale can be useful for the development of the enriched constitutive model presented in this paper (Nguyen and Bui, 2020). Macro test data involving localised failure should also be correctly analysed and interpreted, using additional information on the orientation and thickness of the localisation band, so that more intrinsic material behaviour inside the localisation band can be obtained for constitutive modelling (Le et al., 2020). This matter of analysing micro-scale or experimental data is not a key focus of this paper, and if interested, the readers can see the merits of such an analysis and condensation of rich micro-scale data (Nguyen and Bui, 2020, Le et al., 2020) and interpretation of experimental data involving localised failure (Le et al., 2020) in our recent papers (Le et al., 2020).

The strain rate inside the band  $\dot{\epsilon}^i$  can take the following form (Neilsen and Schreyer, 1993):

$$\dot{\epsilon}^i = \dot{\epsilon}^o + \frac{1}{h_l}(\mathbf{n} \otimes \dot{\mathbf{u}})^{\text{sym}} = \dot{\epsilon}^o + \frac{1}{2h_l}(\mathbf{n} \otimes \dot{\mathbf{u}} + \dot{\mathbf{u}} \otimes \mathbf{n}) \quad (88)$$

where  $\mathbf{n}$  is the normal vector of the band,  $\dot{\mathbf{u}}$  the velocity jump across the localisation band and  $\dot{\epsilon}^o$  the strain rate outside the localisation band. It is noted that all rate terms in this sub-section are pseudo rates, as all equations can be written in incremental forms. Rate forms are used just for the sake of simplicity in the presentation.

The volume averaged strain rate  $\dot{\epsilon}$  is:

$$\dot{\epsilon} = f\dot{\epsilon}^i + (1-f)\dot{\epsilon}^o \quad (89)$$

where  $f$  is the volume fraction of the localisation zone. If an effective size  $H$  of the particle can be defined as  $H = V/S$ , where  $V$  is the volume of the particle and  $S$  the surface area of the localisation zone (Fig. 10), then the volume fraction  $f$  can be expressed as the ratio between the thickness of the localisation band and the particle size  $H$ :

$$f = \frac{Sh_l}{V} = \frac{Sh_l}{SH} = \frac{h_l}{H} \quad (90)$$

Equations (88) and (89) can be used to obtain strain rates  $\dot{\epsilon}^i$  and  $\dot{\epsilon}^o$  in terms of the macro strain rate  $\dot{\epsilon}$  and velocity jump  $\dot{\mathbf{u}}$ :

$$\dot{\epsilon}^o = \dot{\epsilon} - \frac{f}{h_l}(\mathbf{n} \otimes \dot{\mathbf{u}})^{\text{sym}} \quad (91)$$

In the same way, the strain rate inside the band can also be expressed in terms of  $\dot{\epsilon}$  and  $\dot{\mathbf{u}}$ , as:

$$\dot{\epsilon}^i = \dot{\epsilon} + \frac{1-f}{h_l}(\mathbf{n} \otimes \dot{\mathbf{u}})^{\text{sym}} \quad (92)$$

Equations (91) and (92) indicate different strain rates outside and inside the localisation zone, generated by the macro strain rate and the velocity jump between two surfaces of the localisation band and reflecting the discontinuity of strain rates due to localisation. Associated with these strain rates are corresponding stress tensors outside and inside the localisation band, denoted as  $\sigma^o$  and  $\sigma^i$ , and different constitutive responses outside and inside the band. The relationships between macro stress  $\sigma$  and stresses outside ( $\sigma^o$ ) and inside ( $\sigma^i$ ) the localisation band can be obtained using the virtual work equation, expressed as:

$$\sigma : \dot{\epsilon} = f\sigma^i : \dot{\epsilon}^i + (1-f)\sigma^o : \dot{\epsilon}^o \quad (93)$$

Substituting equations (88)-(92) into the above expression of the virtual work and rearranging the obtained expression, we obtain:

$$\frac{1-f}{H}(\mathbf{t}^o - \mathbf{t}^i) \cdot \dot{\mathbf{u}} + [\sigma - f\sigma^i - (1-f)\sigma^o] : \dot{\epsilon}^o = 0 \quad (94)$$

where  $\mathbf{t} = \sigma \cdot \mathbf{n}$ ,  $\mathbf{t}^i = \sigma^i \cdot \mathbf{n}$  and  $\mathbf{t}^o = \sigma^o \cdot \mathbf{n}$  are the tractions associated with macro stress  $\sigma$ , stress  $\sigma^i$  inside and stress  $\sigma^o$  outside the localisation zone, respectively. Since condition (94) must be met for any arbitrary rates  $\dot{\mathbf{u}}$ , and  $\dot{\epsilon}^o$ , the following relationships are obtained:

$$\mathbf{t}^o = \mathbf{t}^i \quad (95)$$

$$\sigma = f\sigma^i + (1-f)\sigma^o \quad (96)$$

It can be proved that the above two relationships also lead to  $\mathbf{t} = \mathbf{t}^o$  as continuity of traction across the whole volume element. As can be seen, there are three stress-strain relationships associated with the macro behaviour and the responses inside and outside the localisation band. While the macro strain rate exhibits a jump across the localisation band, it is reasonable to assume homogeneous deformation inside and outside the localisation band, and corresponding constitutive relationships in the following generic forms:

$$\dot{\sigma}^o = \mathbf{D}^o : \dot{\epsilon}^o = \mathbf{D}^o : \left[ \dot{\epsilon} - \frac{f}{h_l}(\mathbf{n} \otimes \dot{\mathbf{u}})^{\text{sym}} \right] \quad (97)$$

$$\dot{\sigma}^i = \mathbf{D}^i : \dot{\epsilon}^i = \mathbf{D}^i : \left[ \dot{\epsilon} + \frac{1-f}{h_l}(\mathbf{n} \otimes \dot{\mathbf{u}})^{\text{sym}} \right] \quad (98)$$

in which  $\mathbf{D}^o$  and  $\mathbf{D}^i$  are the tangent stiffnesses outside and inside the localisation band, respectively.

Equations (95)–(98) can be used to obtain the macro stress – macro strain relationship as functions of constitutive responses inside and outside the localisation band and the geometrical properties of the band (thickness and orientation). Substituting the rate constitutive equations (97) and (98) into the rate form of volume-averaged stress, we obtain the

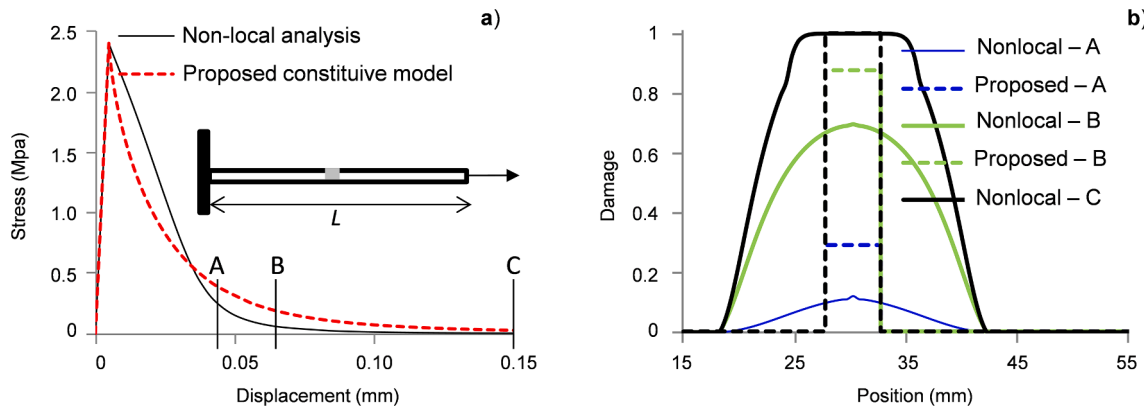


**Fig. 11.** Comparison of our constitutive model and nonlocal analysis for a bar under tension: a) Load-displacement responses and b) Damage profile at points A, B, C in a).

macro stress:

$$\hat{\sigma} = f \mathbf{D}^i : \left[ \dot{\epsilon} + \frac{1-f}{h_l} (\mathbf{n} \otimes \dot{\mathbf{u}})^{\text{sym}} \right] + (1-f) \mathbf{D}^o : \left[ \dot{\epsilon} - \frac{f}{h_l} (\mathbf{n} \otimes \dot{\mathbf{u}})^{\text{sym}} \right] \quad (99)$$

It can be seen that the velocity jump  $\dot{\mathbf{u}}$  is needed for the calculation of the macro stress rate in the above equation, given macro strain rate  $\dot{\epsilon}$  as the input at the particle (or constitutive) level from the numerical methods for the solution of BVPs. The traction continuity  $\mathbf{t}^i = \mathbf{t}^o$  in rate form is used for the determination of  $\dot{\mathbf{u}}$ . From the condition  $\mathbf{t}^i = \mathbf{t}^o$  and constitutive relationships (97) and (98), we can write:

$$\mathbf{D}^i : \left[ \dot{\epsilon} + \frac{1-f}{h_l} (\mathbf{n} \otimes \dot{\mathbf{u}})^{\text{sym}} \right] \bullet \mathbf{n} = \mathbf{D}^o : \left[ \dot{\epsilon} - \frac{f}{h_l} (\mathbf{n} \otimes \dot{\mathbf{u}})^{\text{sym}} \right] \bullet \mathbf{n} \quad (100)$$

The above can be rearranged to obtain the velocity jump  $\dot{\mathbf{u}}$  in term of macro strain rate  $\dot{\epsilon}$ :

$$\dot{\mathbf{u}} = \left[ \frac{1-f}{h_l} (\mathbf{n} \bullet \mathbf{D}^i \bullet \mathbf{n}) + \frac{f}{h_l} (\mathbf{n} \bullet \mathbf{D}^o \bullet \mathbf{n}) \right]^{-1} \bullet (\mathbf{D}^o - \mathbf{D}^i) : \dot{\epsilon} \bullet \mathbf{n} \quad (101)$$

The described algorithm is an explicit stress return algorithm, based on the rate form of traction continuity,  $\mathbf{t}^i = \mathbf{t}^o$ . This is also used to obtain the tangent stiffness of the volume element crossed by a shear band. The readers can refer to Nguyen et al. (Nguyen et al., 2016) and Nguyen & Bui (Nguyen and Bui, 2020) for details and examples on an implicit stress return algorithm.

The approach presented can be used with any existing constitutive models, given the generic forms (97) and (98) for constitutive responses outside and inside the localisation zone, respectively. As can be seen in equations (99) and (101), the size  $H$  of the volume element, thickness  $h_l$  of the localisation band, its orientation and constitutive responses of two separate regions (the band and the outside zone) appear in the constitutive structure. Models derived from this approach automatically possess a length scale  $h_l$  that is invariant with the discretisation and can be considered as an intrinsic material property and behaviour at the mesoscale of the localisation band. Therefore, they can describe and correctly capture both pre- and post-localisation responses at the constitutive (or particle) level (Nguyen et al., 2016, Nguyen and Bui, 2020). As a result, no ad hoc regularisation is needed in the analysis of BVPs. This approach is suitable for any numerical methods for the solution of BVPs, and particularly the SPH, given it does not require any modification beyond the constitutive level, and can be used straightforwardly for an SPH particle. This also forms the basis for more advanced ones, with both elastic and inelastic responses outside the localisation band associated with the activation and deactivation of more than one localisation bands (Nguyen et al., 2017b), or evolution of localisation band thickness associated with the transition from diffuse to localised failure (Nguyen and Bui, 2020).

We assess the performance of our enriched constitutive model against that of a nonlocal analysis of a bar under tension (Fig. 11). This is equivalent to the use of a single integration point (or particle) against detailed modelling and numerical analysis using a nonlocal model. As the stress distribution in this 1D case is uniform, a defect is introduced in the middle of the bar to trigger localised failure. As can be seen in Fig. 11a, the macro stress-displacement responses are very close and the areas under the curves reproduce the input fracture energy, while at the mesoscale (damage evolution inside the band) the nonlocal approach can capture the high gradient of damage thanks to the use of finite elements smaller than the size of the localisation band (Fig. 11b). However, the proposed approach is much more computationally efficient thanks to the embedded mechanism of localised failure at the constitutive level and everything is contained in the structure of the proposed constitutive model, allowing capturing the high gradient of damage across the boundary of the localisation zone in a simplest possible way. In particular, the proposed constitutive approach involves only a few constitutive equations, the solutions of which takes a fraction of a second, compared to the time to solve a large system of coupled equations in the nonlocal approach. The damage profiles along the bar are plotted in Fig. 11b in which the simplicity in the model assumption is clearly reflected. This key feature is missing in classical continuum models, given they do not possess a mechanism and structure to accommodate mesoscale behaviour.

**3.2.3.3. An SPH particle with an embedded localisation band represented by a zero-thickness cohesive frictional model.** From the above general approach, simplified ones can be derived using assumption on the thickness of the localisation band in relation to the size of the volume element containing it. The above whole formulation can also be obtained using a thermodynamics-based approach, as presented in Nguyen & Bui (Nguyen and Bui, 2020). For localisation zone of very small thickness, if this thickness is also very small compared to the size of the volume element (or SPH particle) considered then the volume fraction  $f$  is very small:  $f = \frac{h_l}{H} \ll 1$ , the homogeneous term  $\dot{\epsilon}^o$  in the expression of  $\dot{\epsilon}^i$  is negligible compared to the one caused by the velocity jump and hence can be dropped. Therefore  $\dot{\epsilon}^i$  in equation (88) can be approximated as (Nguyen et al., 2012, Nguyen et al., 2014, Nguyen and Bui, 2020):

$$\dot{\epsilon}^i = \dot{\epsilon}^o + \frac{1}{h_l} (\mathbf{n} \otimes \dot{\mathbf{u}})^{\text{sym}} \approx \frac{1}{h_l} (\mathbf{n} \otimes \dot{\mathbf{u}})^{\text{sym}} \quad (102)$$

Given  $f = \frac{h_l}{H}$ , the strain rate outside the localisation zone can be rewritten as:

$$\dot{\epsilon}^o = \dot{\epsilon} - \frac{f}{h_l} (\mathbf{n} \otimes \dot{\mathbf{u}})^{\text{sym}} = \dot{\epsilon} - \frac{1}{H} (\mathbf{n} \otimes \dot{\mathbf{u}})^{\text{sym}} \quad (103)$$

Examples that are suitable for the above simplification include, but

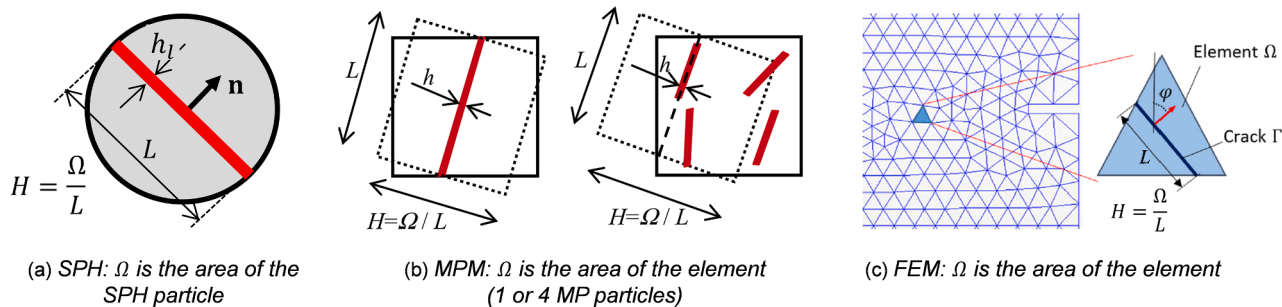


Fig. 12. Determination of size  $H$  for 2D applications using (a) SPH, (b) MPM and (c) FEM, after (Wang et al., 2019, Nguyen et al., 2014, Le et al., 2018).

are not limited to, localised failure of geomaterials such as rocks, concrete under tension or shearing under sufficiently low confining pressures. In such cases, given very small physical thickness of the localisation band, its responses can be described by a cohesive-frictional model for an idealised zero-thickness interface, using traction  $\mathbf{t}^i$  and displacement jump  $\mathbf{u}$ . Therefore the stress  $\sigma^i$  and strain  $\epsilon^i$  are no longer needed. This cohesive-frictional interface model can be described in the following generic incremental form:

$$\dot{\mathbf{t}}^i = \mathbf{K}^i \dot{\mathbf{u}} \quad (104)$$

where  $\mathbf{t}^i = \sigma^i \mathbf{n}$  is the traction and  $\mathbf{K}^i$  the corresponding tangent stiffness of the interface. For  $f \rightarrow 0$ , the macro stress  $\sigma$  coincides with the stress  $\sigma^o$  for the zone outside the localisation band:

$$\sigma = f\sigma^i + (1-f)\sigma^o \approx \sigma^o \quad (105)$$

and the traction continuity (95) is expressed in the following form:

$$\sigma^o \mathbf{n} - \mathbf{t}^i = 0 \quad (106)$$

As traction and displacement jump are used to describe the behaviour inside the localisation zone, the simplified system now contains the following three key relationships:

$$\sigma = \sigma^o = \mathbf{D}^o : \dot{\mathbf{e}}^o = \mathbf{D}^o : \left[ \dot{\mathbf{e}} - \frac{1}{H} (\mathbf{n} \otimes \dot{\mathbf{u}})^{\text{sym}} \right] \quad (107)$$

$$\dot{\mathbf{t}}^i = \mathbf{K}^i \dot{\mathbf{u}} \quad (108)$$

$$\sigma^o \mathbf{n} - \mathbf{t}^i = 0 \quad (109)$$

This simplified model, with the effects of thickness  $h_l$  of the localisation band lumped into the fracture behaviour of the cohesive-frictional model (via fracture energies in both pure and mixed modes) has been extensively used in our groups for modelling geomaterial failure using the SPH (Tran et al., 2019, Wang et al., 2019, Wang et al., 2020, Wang et al., 2017, Tran et al., 2017), MPM (Nguyen et al., 2012, Nguyen et al., 2014, Nguyen and Bui, 2020, Nguyen et al., 2016, Nguyen, 2014), and also FEM (Le et al., 2017, Le et al., 2018, Le et al., 2019).

The length  $H$ , as an effective size of an SPH particle, naturally appears in the structure of the constitutive model, i.e. Equations (107)–(109), and allows scaling of the constitutive behaviour of the SPH particle to correctly describe the post-localisation stage of failure. This is particularly an appealing characteristic for SPH, a truly mesh-free numerical method, as everything required for the proposed approach can be accessed at the particle level and interaction between constitutive models derived from the proposed approach and the SPH-based discretisation is through the effective size  $H$  of the SPH particle, which is

also the resolution of the discretisation (Fig. 12). This is different from FEM (Le et al., 2017, Le et al., 2018, Le et al., 2019) and MPM applications (Nguyen et al., 2012, Nguyen et al., 2014, Nguyen and Bui, 2020, Nguyen et al., 2016, Nguyen, 2014) in which involvement of element size in interfacing models derived from this approach with mesh-based methods is required, given the resolution of the discretization is governed by the element size, not the size of the integration (or material) point (Fig. 12).

The results of SPH simulation for the failure of a notched beam under the three-point bending test in Fig. 13a shows the insensitiveness of the numerical solution with respect to the resolution of the SPH discretisation (Fig. 13a), and damage contour at different stages of failure (Fig. 13b). The constitutive behaviour for SPH in that simulation is based on the approach described above Equations (107)–(109), in combination with a mixed-mode cohesive-frictional model to describe the behaviour of the localisation band idealized as a zero-thickness surface and embedded in the SPH particle. The behaviour of the fracturing SPH particle in such cases automatically scales with its size, thanks to the appearance of its size  $H$  in the constitutive equation. The readers are referred to (Wang et al., 2020) for the detail descriptions of the constitutive model, material constitutive parameters and SPH setting conditions.

### 3.2.4. How do I test the constitutive models implemented in SPH?

Once a particular continuum constitutive model is implemented in SPH, it is important to ensure the SPH code can correctly reproduce the constitutive response. The readers would have noticed that it is not straightforward in SPH to perform an element test, like FEM. Thus, an alternative approach should be used. In our view, one of the first SPH tests that need to pass to ensure the SPH code can correctly reproduce the constitutive response is to conduct a simple shear test (Zhao et al., 2019, Nonoyama et al., 2015). The geometry and setting of this test are shown in Fig. 14. In this test, a representative soil element, which is formed by a group of SPH particles, is placed at the centrally located area and surrounded by boundary areas which are also modelled by a set of SPH particles with the same properties. Particles within the central area are allowed to move freely, while those located within the boundary area are enforced by a constant velocity field defined by:

$$v_{xi} = \zeta v_i \quad \text{and} \quad v_{yi} = 0 \quad (110)$$

where  $v_{xi}$  and  $v_{yi}$  are the horizontal and vertical velocities of particles within the boundary area, respectively, and  $\zeta$  is a constant parameter defining the loading rate (Zhao et al., 2019).

The responses of a constitutive model in SPH can be then checked by calculating the averaged normal and shear stresses of all SPH particles located within the central area, and comparing these results against those obtained from a single-element test using standard stress-updating

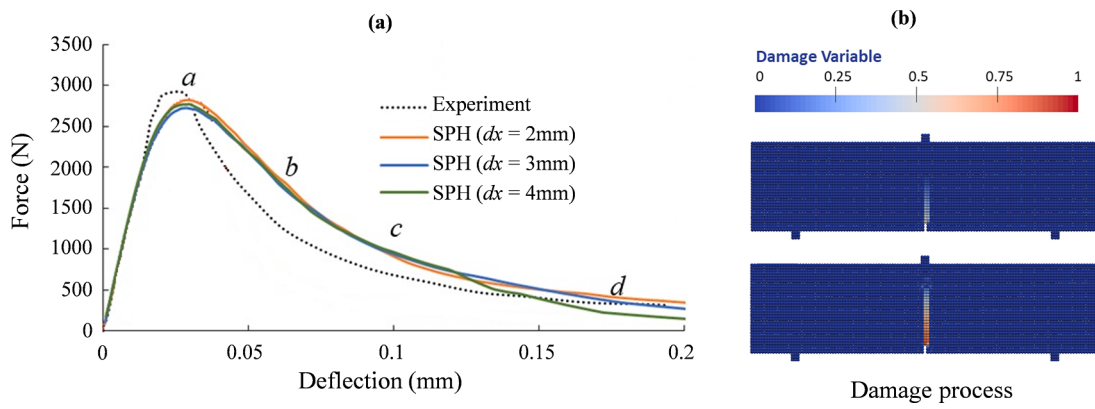


Fig. 13. SPH simulation of three-point bending fracture, after (Wang et al., 2020).

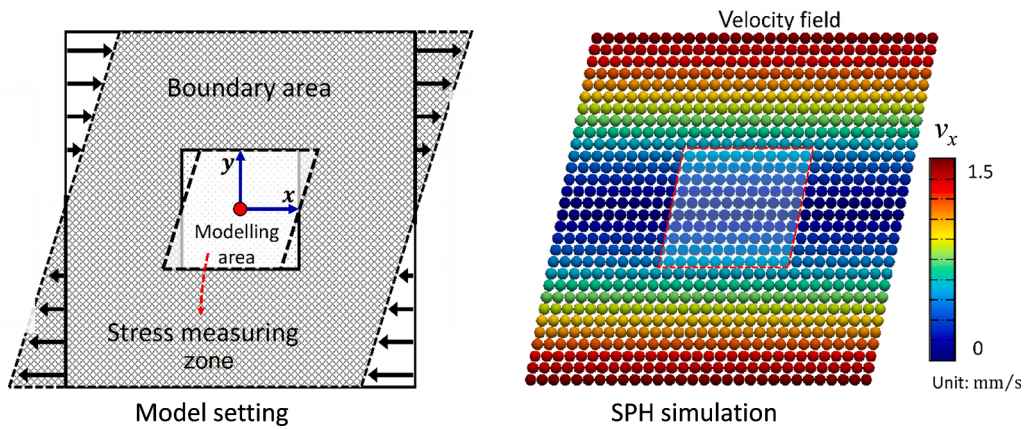


Fig. 14. Setting of simple shear test for SPH simulations and example of velocity field, after (Zhao et al., 2019).

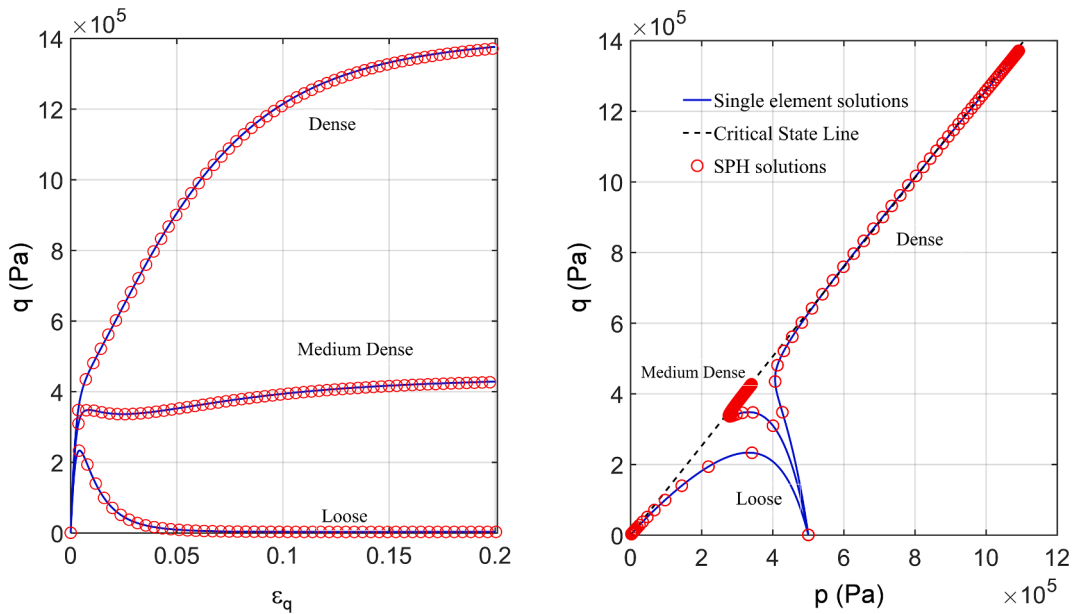


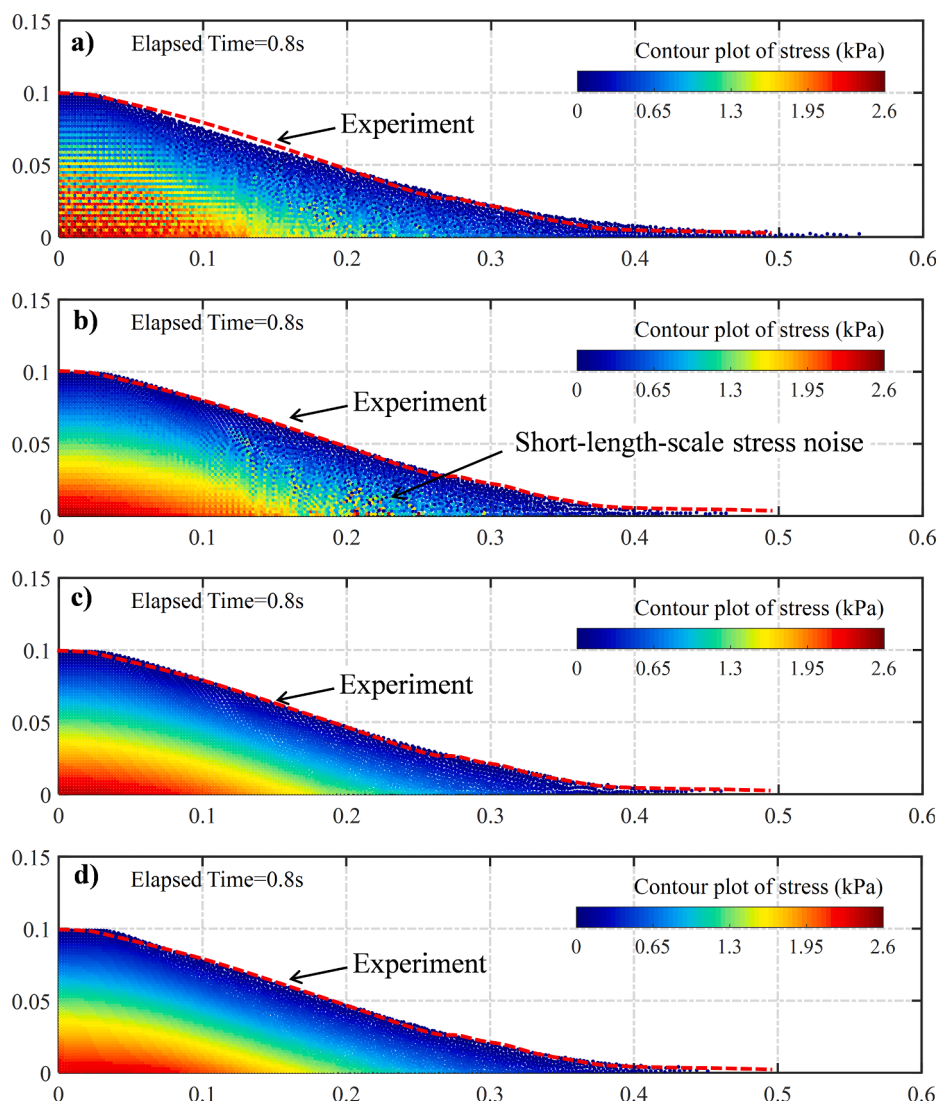
Fig. 15. SPH modelling of the simple shear test for a critical state soil model.

**Table 1**

Physical properties used in the critical state soil model.

Material properties	Loose sand	Medium dense	Dense
Referential bulk modulus, $K_0$ (dimensionless)	130	130	130
Elastic constant controlling nonlinear stiffness, $\zeta$	0.67	0.67	0.67
Poisson's ratio, $\nu$	0.2	0.2	0.2
Critical-state friction angle, $\phi_c$	31.4°	31.4°	31.4°
Initial critical state void ratio, $e_{ref}$	0.964	0.964	0.964
CSL slope in the $e - \log p'$ , $\lambda$	0.118	118	118
Constant controlling the nonlinear of CSL, $\xi$	0.205	0.205	0.205
Stress-dilatancy parameter, $A_d$	0.5	0.5	0.5
Phase transformation parameter, $n_d$	3.5	3.5	3.5
Peak strength parameter, $n_p$	1.9	1.9	1.9
Plastic shear modulus constant, $k_p$	0.0017	0.0017	0.0017
Initial void ratio, $e_0$	0.77	0.81	0.91

Note: CSL = Critical State Line and the notations follow the definitions in (Jin et al., 2017).

**Fig. 16.** Numerical oscillations in the granular flow simulation using SPH its alternative treatments: a) without any dissipative term, b) with the artificial viscosity; c) with the artificial viscosity and stress regularisation; and d) with the viscous damping and stress regularisation, after (Nguyen et al., 2017a).

algorithms. Fig. 15 illustrates the capability of the simple shear test in assessing a constitutive model implemented in an SPH code. In this figure, a critical state-based constitutive model for sandy materials (Jin et al., 2017), which was basically a simplified version of the well-known SANISAND model (Dafalias and Manzari, 2004), was implemented in the MCG-SPH code<sup>6</sup> and tested for three different states of materials, i.e. dense, medium and loose sands. The material properties required for this model are listed in Table 1 and the semi-implicit stress updating procedure was used to advance the stress update. The readers should have immediately seen that, under the current setting conditions, the simple shear test represents the undrained testing conditions, leading to the fully liquefied behaviour of loose sand. In contrasts, the effective mean stress in the medium dense and dense sands increases upon reaching the so-call zero dilatancy point and reverses its direction toward the critical state line. The SPH results obtained from the simple shear tests reflect well these testing conditions and agree well with the results obtained from a single element test at the constitutive level. This indicates that the SPH method, in combination with the semi-implicit stress updating procedure, could reproduce well the stress-strain relationship and stress loading path for an advanced constitute model. The simple shear test serves as an excellent mean to verify a constitutive model implemented in SPH. However, it is worth noting that when checking a constitutive model using the simple shear test, it is important to not produce localised failure within the testing zone. This can be achieved by either varying the size of the testing element or the particle resolution.

### 3.3. Numerical oscillations and dissipations in SPH

The readers should have noticed that the SPH motion equation described in Section 3.1 is a fully dynamic equation<sup>7</sup>, i.e. Equation (49). In the absence of any dissipated term, the fully dynamic equation would cause SPH particles to freely oscillate due to even small unbalanced forces, most of which is attributed to the zero-energy mode produced by the anti-symmetric kernel function with zero kernel gradient at the inflection point. The readers should also be aware that this oscillation of SPH particles or material points is a common issue associated with any numerical method used to solve the fully dynamic motion equation, including FEM, MPM or more obvious in DEM and molecular dynamic simulations. A common way to suppress this numerical oscillation in SPH is to introduce an artificial viscosity term, which was originally proposed by Monaghan and Gingold (Monaghan and Gingold, 1983):

$$\mathbf{D}_{disp}|_i = \sum_{j=1}^N m_j \left( \frac{\alpha_d c_{ij} \pi_{ij} - \beta_d \tau_{ij}^2}{\rho_{ij}} \right) \cdot \nabla_i W_{ij} \quad \text{with} \quad \pi_{ij} = \frac{h_{ij} \mathbf{v}_{ij} \cdot \mathbf{r}_{ij}}{|\mathbf{r}_{ij}|^2 + \epsilon h_{ij}^2} \quad (111)$$

where  $\alpha_d$  and  $\beta_d$  are two unknown constants, which are usually taken to be unity (Monaghan, 1992) or equal to 0.1 and 0 for granular materials (Bui et al., 2008a), respectively;  $\rho_{ij}$  and  $h_{ij}$  are the mean density and smoothing length;  $\epsilon = 0.01$  is a numerical parameter introduced to prevent numerical divergences; and  $c_{ij}$  is the mean sound velocity, which for solid materials is computed by  $c_i = \sqrt{E_i/\rho_i}$  with  $E_i$  is the material elastic modulus (Bui and Fukagawa, 2013). The artificial viscosity is added to the motion equation of a particle  $i$  only if the following condition is satisfied,  $\mathbf{v}_{ij} \cdot \mathbf{r}_{ij} < 0$ , leading to:

$$\frac{d\mathbf{v}_i}{dt} = \sum_{j=1}^N m_j \left( \frac{\mathbf{\sigma}_i}{\rho_i^2} + \frac{\mathbf{\sigma}_j}{\rho_j^2} \right) \cdot \nabla_i W_{ij} + \mathbf{D}_{disp}|_i \cdot \mathbf{I} + \mathbf{f}_{ext} \quad (112)$$

<sup>6</sup> MCG-SPH code refers to the SPH code developed at the Monash Computational Geomechanics (MCG) Lab at Monash University, Melbourne, Australia.

<sup>7</sup> Dissipation due to plastic deformation is different from the dissipation discussed in this section. This raises an interesting question on whether viscoplastic constitutive models would help to suppress these numerical oscillations, which could be an interesting topic for future investigations of SPH.

The introduction of the artificial viscosity to the momentum equation not only helps to suppress the numerical oscillations but also mitigates the pairing instability in SPH since the artificial viscosity acts as a repulsive force between two particles when they are approaching each other (i.e.  $\mathbf{v}_{ij} \cdot \mathbf{r}_{ij} < 0$ ). However, the main drawback of this approach is that it introduces a large amount of dissipated energy to the system when a high value of  $\alpha_d$  is adopted. Therefore, it is preferable to minimise the influence of this dissipated term in SPH simulations by setting these unknown parameters as small as possible. Bui et al. (Bui et al., 2008a), through the investigation on the influence of this dissipated term on the granular flow, suggested that the second term involved  $\beta_d$  does not have a strong influence on the overall behaviour of granular materials. They suggested that, for SPH applications adopting the Cubic-spline function with  $h = 1.2\Delta x$ ,  $\alpha_d = 0.1$  seems to be suitable to most cases.

The effectiveness of the artificial viscosity in suppressing the numerical oscillation is demonstrated in Fig. 16a and Fig. 16b, where an SPH simulation of a granular column collapse test using the Drucker-Prager model described in Section 3.2.2.1 was adopted, with other details of material properties and setting conditions for these simulations being found in (Nguyen et al., 2017a). The readers can immediately see that, without any dissipated term, SPH results in a highly oscillated stress profile across the computational domain, causing unrealistic motion of SPH particles in the undisturbed zone (i.e. left corner of the computational domain) and thus over predicting the final runout distance of the granular material (Fig. 16a). This oscillation could be effectively suppressed by adding the artificial viscosity in the momentum equation, which dampens out undesired motions in the undisturbed zone and thus helping to produce a realistic stress profile in this zone and the final run-out distance as compared to the experiment (Fig. 16b). Nevertheless, there still exists the stress noise in the area where the material undergoes large shear deformation, which was previously referred to as the short-length scale noises (Nguyen et al., 2017a), which were caused by several factors including zero-energy mode and explicit numerical scheme and further works are required to fully address this issue. Nevertheless, it was previously demonstrated that the stress/pressure noise does not produce pronounced effects on the kinematics of material flows (Bui et al., 2008a, Bui and Fukagawa, 2013, Nguyen et al., 2017a), thanks to the SPH summation kernel approximation, which compensates these noises. One simple way to remove this stress noise is to adopt the stress regularisation technique, which requires filtering the stresses after each or several computational cycles using the following formulation (Nguyen et al., 2017a):

$$\langle \mathbf{\sigma}_i \rangle = \sum_{j=1}^N V_j \mathbf{\sigma}_i \bar{W}_{ij} \quad (113)$$

where  $\bar{W}_{ij}$  is the corrected kernel function, which could be achieved by using either Shepard or Moving Least Square (MLS) corrections (Nguyen et al., 2017a, Bui and Nguyen, 2020). The MLS correction produces a smooth stress profile as shown in Fig. 16c, while still achieving the result which is comparable to that without using the stress regularisation (Fig. 16b) as well as experiment. This confirms that the short-length scale noise, although existing in SPH simulations, does not produce pronounced effects on the kinematic of the granular flows. Nevertheless, the use of stress regularisation might have a strong implication in applications involving soil-structure interactions, where accurate measures of stresses acting on structures are required.

In view of the dissipated mechanism, the readers should have noticed that the artificial viscosity is only activated between two particles when they are approaching each other (i.e.  $\mathbf{v}_{ij} \cdot \mathbf{r}_{ij} < 0$ ). This means that some particles in the large shear deformation zone might not have received dissipated forces from their neighbouring particles when  $\mathbf{v}_{ij} \cdot \mathbf{r}_{ij} \geq 0$ . Thus, the oscillation caused by the dynamic equation might not be fully dissipated in the large shear deformation zone, causing numerical os-

cillations. An alternative approach is to replace the artificial viscosity by a viscous damping force per unit mass defined by (Nguyen et al., 2017a):

$$\mathbf{D}_d|_i = -c_d \mathbf{v}_i \quad (114)$$

where  $c_d$  is a damping coefficient, which can be computed by  $c_d = \xi \sqrt{E/\rho h^2}$  (Bui and Fukagawa, 2013) with  $\xi$  being a non-dimensional damping coefficient that requires calibrations for different applications. This viscous damping force is directly added to each particle, and thus in principle, representing the true damping force in the dynamic system. The damping force can be added to the momentum equation as follows:

$$\frac{d\mathbf{v}_i}{dt} = \sum_{j=1}^N m_j \left( \frac{\boldsymbol{\sigma}_i}{\rho_i^2} + \frac{\boldsymbol{\sigma}_j}{\rho_j^2} \right) \cdot \nabla_i W_{ij} + \mathbf{D}_d|_i \cdot \mathbf{I} + \mathbf{f}_{ext} \quad (115)$$

It is argued that this viscous damping force has a more physical meaning compared to the artificial viscosity because the damping coefficient is directly linked to material properties (Nguyen et al., 2017a). Thus, once the non-dimensional parameter is calibrated for a certain type of material, the damping coefficient will purely depend on the material properties, unlike the artificial viscosity, whose constant parameter has no physical meaning. The combination of this viscous damping and the stress regularisation could effectively remove the short-length scale stress noises in SPH simulations while still producing the result that is comparable to the standard SPH with the artificial viscosity as well as the experiment as shown in Fig. 16d. Furthermore, as demonstrated in the previous study by Bui et al. (Bui and Fukagawa, 2013), the use of this viscous damping force in SPH is critical in obtaining correct initial in-situ stress profiles for general geotechnical applications.

### 3.4. Tensile instability issue in SPH

Perhaps, the SPH tensile instability issue is the most confusing SPH topic reported in the literature because it is often mixed up with a very similar issue but is totally different in mechanism, namely the pairing instability issue. Different from the paring instability issue, which is mainly caused by the misuse of the kernel function and was discussed in details in Section 2.3, the SPH tensile instability is caused by negative pressures/stresses, which results in an attraction force between a pair of SPH particles and causing particles to move closer to each other (i.e. forming clumps or clusters of SPH particles). This tensile instability issue was first studied by Swegle et al. (Swegle et al., 1995), who related it to the sign of the stress and the second derivative of the kernel function. They stated that the tensile instability occurs in SPH simulations whenever the following condition meets, i.e.  $\boldsymbol{\sigma} \cdot \nabla^2 W > 0$  with  $\boldsymbol{\sigma}$  being the stress tensor of an SPH particle. With the second derivative of the kernel function (i.e. the gradient of  $\nabla W$ ) changes its sign from negative to positive as the relative distance from between two particles increases (i.e. Fig. 6), this condition suggests that the SPH tensile instability occurs in both compression and tension stresses regardless of the kernel function so long as this condition meets. However, our numerical tests illustrated in Fig. 7 showed that no tensile or pairing instability issues were observed in SPH simulations using the Wendland C<sup>2</sup> kernel function. This suggests that the above tensile instability condition established by Swegle et al. (Swegle et al., 1995) is no longer valid, if not incorrect. In particular, Swegle et al. (Swegle et al., 1995) did not recognise the mechanism of pairing instability caused by the misuse of the kernel function and thus incorrectly described both instability mechanisms using the same criterion. Furthermore, the Cubic-spline kernel function used in their study appears to be suffered the most from pairing instability, as demonstrated in Section 2.3.

Within the context of geomechanics applications, Bui et al. (Bui et al., 2008a) were the first who demonstrated that no tensile instability should occur in non-cohesive granular materials, which again suggests

that the tensile instability condition established by Swegle et al. (Swegle et al., 1995) is not valid. In particular, Bui et al. (Bui et al., 2008a) demonstrated that the tensile instability issue does not appear in non-cohesive granular materials and can be completely removed by adopting a tension cracking treatment, which removes undesirable negative stresses from numerical simulations. This treatment is physically correct for non-cohesive granular materials as these materials, in principle, cannot carry any tensile stress unless they are under unsaturated conditions, which is out of the scope of this discussion. On the other hand, for cohesive frictional granular materials, it is inevitable to avoid the possibility of tensile instability in SPH simulations because there always exists a tension zone in the yield surface space of these materials, which is corresponding to the negative stress zone (Bui et al., 2008a). Therefore, an alternative treatment is required to remove this tensile instability issue associated with cohesive soils. There have been several attempts reported in the literature, which can be used to remove this instability issue (Randles and Libersky, 2000, Dyka et al., 1997). However, in our view, the most effective and successful has been the artificial pressure method originally proposed by Monaghan (Monaghan, 2000) for fluids and was subsequently generalised by Gray & Monaghan (Gray et al., 2001) for elastic solid and named as the artificial stress method. The key idea of this method is to introduce a small repulsive force, which can be either formulated as a function of pressure (Monaghan, 2000) or stresses (Gray et al., 2001), between a pair of neighbouring particles by using an artificial pressure/stress term to prevent them from getting closer to each other when two particles are in a state of tensile stress. The artificial stresses approach appears to be more generic and rigours, though it is computationally more expensive than the artificial pressure approach. The artificial stress is defined as follows (Gray et al., 2001):

$$\mathbf{F}_o|_i = \sum_{j=1}^N m_j f_{ij}^n (\mathbf{R}_i + \mathbf{R}_j) \cdot \nabla_i W_{ij} \quad \text{with} \quad f_{ij} = \frac{W_{ij}(\mathbf{x}_{ij}, h)}{W(\Delta x, h)} \quad (116)$$

where  $n$  is the exponential factor dependent on the smoothing kernel and  $\Delta x$  is the initial particle spacing. Gray and Monaghan (Gray et al., 2001) suggested the best choice of  $n$  when applying SPH for elastic solid is 4. However, Bui et al. (Bui et al., 2008a) found that this choice cannot be used for cohesive-frictional soils. Instead, they suggested that, for most SPH applications to simulate cohesive-frictional granular materials using the Cubic-spline function, the exponential factor  $n$  should be chosen to be around 2.55. This ensures that the effect of the artificial stress is confined to the nearest neighbouring particles.

To complete the expression of the artificial stress method, one needs to define the artificial stress tensor  $\mathbf{R}$  and this can be achieved by simply linking this quantity to the stress tensor  $\boldsymbol{\sigma}$ . Gray and Monaghan (Gray et al., 2001) suggested that the artificial stress tensor  $\mathbf{R}_i$  of a particle  $i$  can be calculated as follows:

$$\widehat{\mathbf{R}}_i = \varepsilon_0 \frac{\langle -\widehat{\boldsymbol{\sigma}}_i \rangle}{\rho_i^2} \quad (117)$$

where  $\langle \cdot \rangle$  indicates the Macaulay brackets;  $\widehat{\mathbf{R}}_i$  is the diagonal component of the artificial stress tensor  $\mathbf{R}_i$ ;  $\widehat{\boldsymbol{\sigma}}_i$  is the diagonal component of the stress tensor  $\boldsymbol{\sigma}_i$  of the particle  $i$ ; and  $\varepsilon_0$  is a constant parameter controlling the amount of artificial stress (or repulsive force) required to avoid particles getting too close to each other. The value of  $\varepsilon_0$  should be in a range of 0 to 1, and the recommended value for cohesive-frictional granular materials is  $\varepsilon_0 = 0.5$  for SPH simulations using the Cubic-spline kernel function (Bui et al., 2008a). Accordingly, the procedure to obtain  $\mathbf{R}_i$  can be generally summarised as follows:

1.  $\widehat{\boldsymbol{\sigma}}_i$  is obtained by diagonalising  $\boldsymbol{\sigma}_i$
2.  $\widehat{\mathbf{R}}_i$  is calculated from  $\widehat{\boldsymbol{\sigma}}_i$  using Equation (117)
3.  $\mathbf{R}_i$  is obtained by rotating  $\widehat{\mathbf{R}}_i$  back to the reference coordinate system

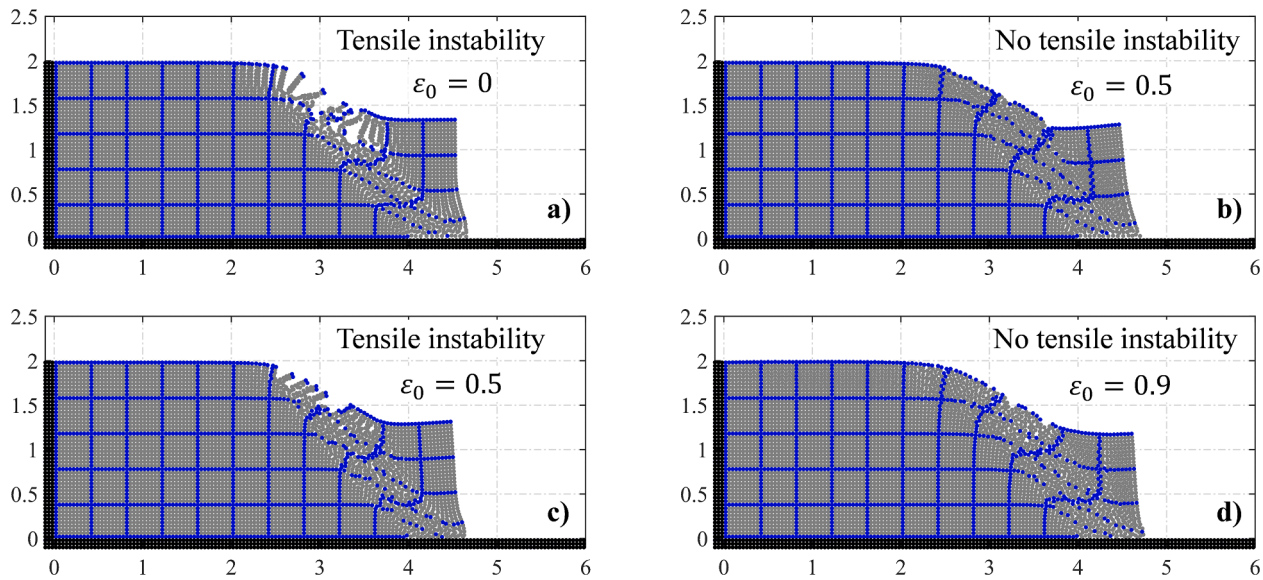


**Fig. 17.** Tensile instability test in a cohesive-frictional granular material: a) without any tensile instability treatment; b) with the artificial stress method; c-d) with the artificial pressure method. In all cases, the exponent  $n$  was kept constant at 2.55.

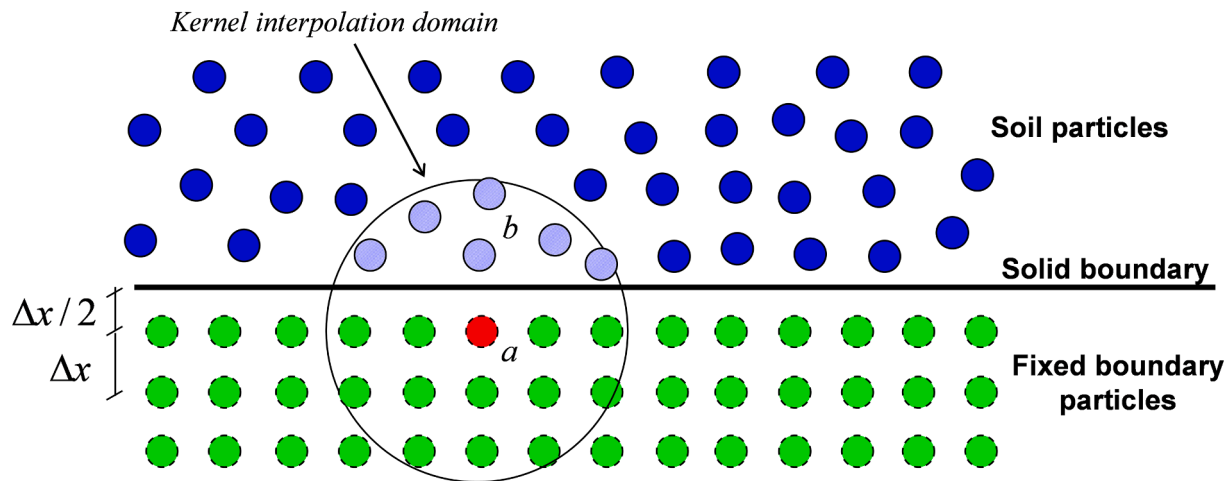


**Fig. 18.** Arrangement of boundary and real particles in SPH.

The readers should have noticed that the above procedure is general and, in principle, is suitable for both 2D and 3D applications. For 2D applications, the procedure to compute  $\hat{\sigma}_i$ ,  $\hat{R}_i$  and  $\mathbf{R}_i$  is straightforward, and the details of which were explained in (Bui et al., 2008a, Gray et al., 2001) and thus are not repeated here. The readers are referred to (Bui et al., 2008a) for further discussion on the selection of appropriate constant parameters for applications in geomechanics. The extension of the artificial stress method for 3D applications is rather complicated and has not been widely reported in the literature, mainly due to the complex and time-consuming procedure to obtain  $\hat{\sigma}_i$ ,  $\hat{R}_i$  and  $\mathbf{R}_i$  under 3D conditions. An alternative approach to avoid the complicated procedure to obtain the artificial stress in 3D is to adopt the artificial pressure approach, originally proposed by Monaghan (Monaghan, 2000) for CFD applications. According to this approach, the artificial stress (or pressure) can be simply computed by:

$$\mathbf{R}_i = \epsilon_0 \frac{\langle p_i \rangle}{\rho_i^2} \bullet \mathbf{I} \quad (118)$$

where  $p_i = I_1/3$  is the isotropic mean pressure and  $\epsilon_0$  should be still in a range of 0 to 1. The artificial pressure approach is straightforward as it

does not require any extra computational effort to diagonalise stress tensors, and thus saving much more computational cost compared to the artificial stress method. However, because only the mean pressure is involved in the computation, this approach appears to be less effective than the artificial stress method, though this can be compensated by adjusting constant parameters.

Once the artificial stress  $\mathbf{F}_{\sigma}|_i$  is evaluated, it can be simply added to the momentum equation as follows:

$$\frac{d\mathbf{v}_i}{dt} = \sum_{j=1}^N m_j \left( \frac{\sigma_i}{\rho_i^2} + \frac{\sigma_j}{\rho_j^2} \right) \bullet \nabla_i W_{ij} + \mathbf{D}_{disp}|_i \bullet \mathbf{I} + \mathbf{F}_{\sigma}|_i + \mathbf{f}_{ext} \quad (119)$$

The effectiveness of the artificial stress method in removing the tensile instability in a cohesive frictional granular material was previously demonstrated in Bui et al. (Bui et al., 2008a) and shown in Fig. 17b for the same material properties and numerical setting conditions. The recommended value for constant parameter  $\epsilon_0$  was 0.5 for SPH simulations adopting the Cubic-spline kernel function with the smoothing length of  $h = 1.2\Delta x$ . However, for different kernel functions with a different range of interpolation domain, parametric studies are required to find an appropriate constant parameter  $\epsilon_0$  for the chosen kernel

function. On the other hand, the artificial pressure method appears to be less effective than the artificial stress method as it does not remove the tensile instability for the same set of constant parameter (i.e.  $\varepsilon_0 = 0.5$  and  $n = 2.55$ ), as shown in Fig. 17c. However, when increasing this parameter to  $\varepsilon_0 = 0.9$ , the artificial pressure method starts to show its effectiveness in removing the tensile instability in the cohesive frictional materials, as demonstrated in Fig. 17d. Finally, it is noted that when investigating the tensile instability issue, it is important to distinguish this issue from the pairing stability, which is mainly caused by the misuse of the smoothing length of a particular kernel function.

### 3.5. Boundary conditions in SPH

Like any other numerical methods, the treatment of boundary conditions in SPH is required to facilitate its applications to a wide range of engineering problems. Several specific boundary conditions that are commonly encountered when applying SPH to the geotechnical engineering field are discussed below.

#### 3.5.1. Solid boundary conditions

Fully-fixed and free-slip (or free-roller) conditions are two typical boundary conditions commonly encountered in geotechnical applications. In FEM and other numerical methods, these boundary conditions can be straightforwardly imposed by prescribing specific conditions on material nodes/points located on the boundary of the problem domain. In SPH, although it is possible to directly impose such prescribed boundary values to SPH particles, there exist other issues associated with particles located close to the solid boundary. For example, when an SPH particle approaches the solid boundary, the kernel interpolation domain of the particle will be truncated by the boundary and resulting in a low accuracy of SPH interpolation. Thus, extra treatment is required to avoid this issue and a common approach is to create boundary particles with appropriated boundary conditions.

Two typical methods, which are the root of all existing boundary treatment methods, were proposed to deal with the above SPH solid boundary conditions, including the ghost-particle approach (Libersky et al., 1993) and fixed-particle approach (Takeda et al., 1994, Morris et al., 1997). The former approach requires a frequent update of boundary particle position and is often used to enforce free-slip (or symmetric) boundary conditions, while in the latter approach, the position of boundary particles is fixed and is often used to model fully-fixed boundary conditions. While the ghost-particle approach (Libersky et al., 1993) can be directly used to replicate the free-slip boundary conditions suitable for most geotechnical problems (Bui et al., 2008a), the fixed-particle approach (Takeda et al., 1994, Morris et al., 1997) required further improvement to accommodate stress boundary conditions suitable for wider geomechanics applications. For example, to achieve the required stress boundary conditions for the fully-fixed solid boundary,

Bui et al. (Bui et al., 2008a, Bui and Fukagawa, 2013) proposed an approach that assumes a locally uniform distribution of stress on the solid boundary. In their approach, when a soil particle  $b$  interacts with a boundary particle  $a$  on the solid boundary (see Fig. 18), the stress tensor of particle  $a$  is assumed to be equal to that of particle  $b$ . In this way, all neighbouring particles of  $b$  located within the solid boundary will share the same stress tensor as the soil particle  $b$  (i.e. locally uniform distribution of stress), and thus generating a sufficient repulsive force to preventing soil particles from penetrating the solid boundary.

Alternative to the combined approach, which requires to create ghost- and fixed-particles to model to the free- and fully fixed-boundary conditions, the fixed-boundary particles can be used to replicate both boundary conditions (Bui, 2007, Yang et al., 2020a). As shown in Fig. 18, depending on the extent of kernel interpolation domain, three or four layers of fixed boundary particles are used to represent the solid boundary with the first layer placed at a distance of  $0.5\Delta x$  away from the boundary in the normal direction. These boundary particles carry all essential information as required for material particles, but their properties are directly interpolated from adjacent soil particles (Bui, 2007, Yang et al., 2020a). For the fully-fixed boundary condition, the following conditions are imposed to fixed-boundary particles:

$$\mathbf{v}_a = - \sum_j V_b \mathbf{v}_b W_{ij} \quad \text{and} \quad \boldsymbol{\sigma}_a = \sum_j V_b \boldsymbol{\sigma}_b W_{ab} \quad (120)$$

while for the free-slip boundary condition, the following conditions are imposed to fixed-boundary particles:

$$\mathbf{v}_{a,n} = - \sum_b V_b \mathbf{v}_{b,n} W_{ab} \quad \text{and} \quad \mathbf{v}_{a,t} = \sum_b V_b \mathbf{v}_{b,t} W_{ab} \quad (121)$$

$$\boldsymbol{\sigma}_a^{\alpha\beta} = \begin{cases} \sum_b V_b \boldsymbol{\sigma}_b^{\alpha\beta} W_{ab} & \alpha = \beta \\ - \sum_b V_b \boldsymbol{\sigma}_b^{\alpha\beta} W_{ab} & \alpha \neq \beta \end{cases} \quad (122)$$

where  $\alpha$  and  $\beta$  represent the Cartesian coordinate;  $W_{ab} = W_{ab}/(\sum_b V_b W_{ab})$  is the normalised kernel operator;  $\mathbf{v}_{a,n}$  and  $\mathbf{v}_{a,t}$  are the normal and shear velocity components of particle  $a$  with respect to the solid boundary surface; and  $\boldsymbol{\sigma}_a$  is the stress tensor of boundary particle  $a$ . The above fixed-boundary particles approach was proven to work well in the context of geophysical granular flow modelling (Yang et al., 2020a) and achieved comparable results to that of the combined boundary treatment approach (Bui et al., 2008a, Bui and Fukagawa, 2013)

#### 3.5.2. Flexible confined stress boundary

While the solid boundary conditions can be reasonably well modelled using either ghost- or fixed-boundary particles, it is not straightforward to extend these approaches to model flexible confining stress boundaries. One of the key reasons is because this type of boundary condition often involves complex moving surface boundary, making it difficult to create a required number of boundary layers of ghost- or fixed-boundary particles. Therefore, it is desirable to develop a robust approach that does not require creating ghost- or fixed-boundary particles, while can still impose the required confining stress to flexible boundaries. Such an approach was recently proposed in (Zhao et al., 2019) by making use of kernel truncation properties of SPH kernel approximations near boundaries (Bui and Fukagawa, 2013). The key idea behind this approach is illustrated in Fig. 19. Consider a continuum body  $\Omega$  of arbitrary shape represented by a set of SPH particles. If one wants to automatically impose a constant confining stress  $\sigma_c$  on the interface of the continuum domain, all they need to do is to assign a constant stress field to all SPH particles representing the body  $\Omega$ , and adding the following confining stress term to the momentum equation of each SPH particle:

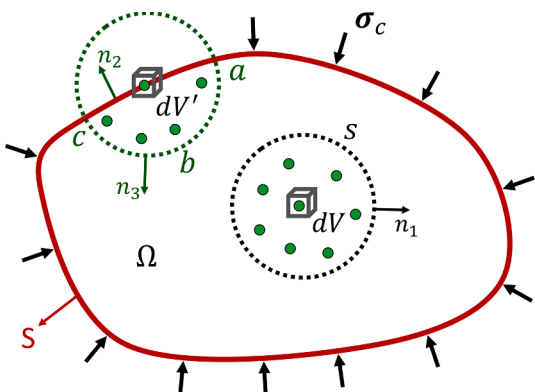


Fig. 19. Illustration of the proposed confining boundary condition, after (Zhao et al., 2019).

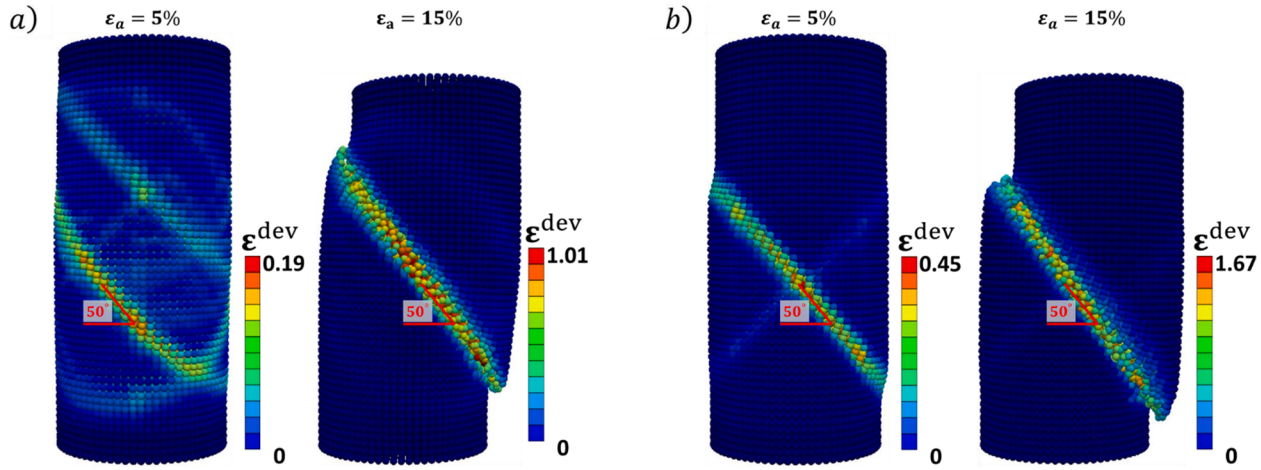


Fig. 20. Deformation of soil specimens in triaxial shear tests under a) 50 kPa confining stress b) 100 kPa confining stresses, after (Zhao et al., 2019).

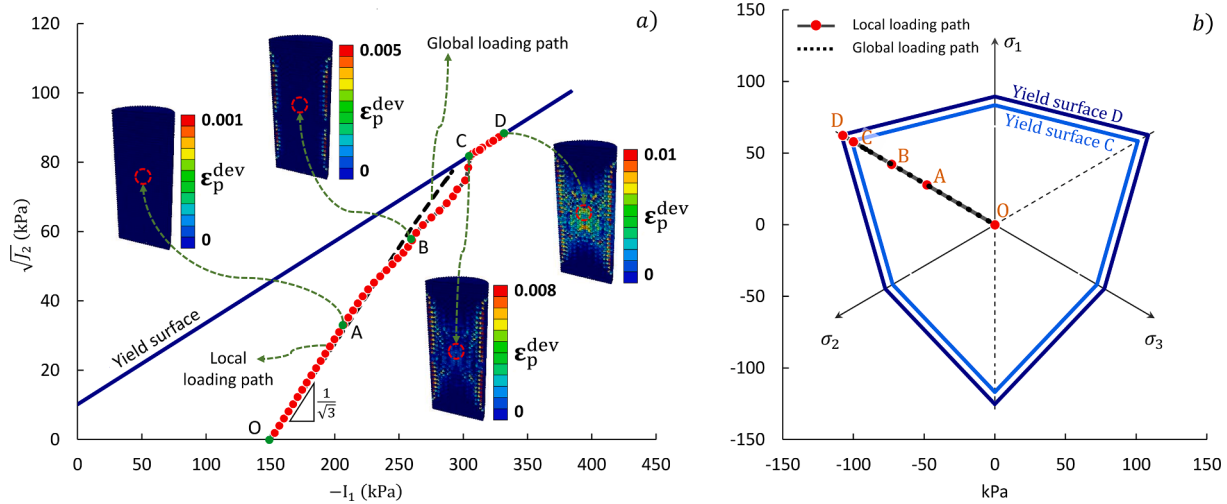


Fig. 21. Stress loading path measured at the centre of the numerical sample in the triaxial test under the confining stress of 50 kPa: a) On the meridian plane and b) On the deviatoric plane, after (Zhao et al., 2019).

$$\mathbf{P}_{\sigma_c}|_{l_i} = \sum_{j=1}^N \frac{m_j}{\rho_i \rho_j} (\boldsymbol{\sigma}_{ci} + \boldsymbol{\sigma}_{cj}) \bullet \nabla_i W_{ij} \quad (123)$$

The readers would have wondered why the above additional term produces the constant confining stress  $\sigma_c$  on the surface  $S$  of the continuum body  $\Omega$ , while not altering the internal forces acting on SPH particles located inside the interface (i.e. particle represents an element  $dV$ ). To demonstrate this concept, let us rewrite Equation (123) in the following kernel integral form:

$$\mathbf{P}_{\sigma_c}|_{l_i} = \sum_{j=1}^N \frac{m_j}{\rho_i \rho_j} (\boldsymbol{\sigma}_{ci} + \boldsymbol{\sigma}_{cj}) \bullet \nabla_i W_{ij} \approx \frac{1}{\rho_i} \int_{\Omega} (\boldsymbol{\sigma}_{ci} + \boldsymbol{\sigma}_{cj}) \bullet \nabla_i W_{ij} dV_j \quad (124)$$

where  $dV_j$  is the volume of particle  $j$  or a volume element  $j$ . The above kernel integral can be further extended as follows:

$$\frac{1}{\rho_i} \int_{\Omega} (\boldsymbol{\sigma}_{ci} + \boldsymbol{\sigma}_{cj}) \bullet \nabla_i W_{ij} dV_j = \frac{1}{\rho_i} \int_{\Omega} (\boldsymbol{\sigma}_{cj} - \boldsymbol{\sigma}_{ci}) \bullet \nabla_i W_{ij} dV_j + \frac{1}{\rho_i} \int_{\Omega} (2\boldsymbol{\sigma}_{ci}) \bullet \nabla_i W_{ij} dV_j \quad (125)$$

Because the confining pressure is constant everywhere on the domain  $\Omega$ , the first term on the right-hand side of Equation (125) vanishes for every particle representing  $\Omega$ . The remaining term can be further analysed by applying the divergence theorem, which converts the volume integral to the surface integral, we have:

$$\frac{1}{\rho_i} \int_{\Omega} (2\boldsymbol{\sigma}_{ci}) \bullet \nabla_i W_{ij} dV_j = -\frac{2\boldsymbol{\sigma}_{ci}}{\rho_i} \left( \int_S W_{ij} \vec{n} ds \right) \quad (126)$$

where  $S$  is the surface of the volume  $\Omega$  and  $\vec{n}$  is unit vector normal to  $S$ . The above surface integral is zero everywhere within  $\Omega$ , such as for SPH particle  $i$  representing element  $dV$  in Fig. 19, which can be attributed to the symmetric property of the kernel function  $W_{ij}$ . In other words, if the kernel interpolation domain of a particle representing  $\Omega$  is closed or not truncated, its surface integral will theoretically vanish<sup>8</sup>. However, this is not the case for particle representing element  $dV$ , which located close to the surface boundary  $S$  of the domain  $\Omega$ . In this case, the above surface integral can be further written as follows:

$$-\frac{2\boldsymbol{\sigma}_{ci}}{\rho_i} \left( \int_S W_{ij} \vec{n} ds \right) = -\frac{2\boldsymbol{\sigma}_{ci}}{\rho_i} \int_{ac} W_{ij} \vec{n}_2 ds - \frac{2\boldsymbol{\sigma}_{ci}}{\rho_i} \int_{abc} W_{ij} \vec{n}_3 ds \quad (127)$$

where  $\vec{n}_2$  and  $\vec{n}_3$  are unit vectors normal to surface sections  $ac$  and  $abc$ , as shown in Fig. 19, respectively. The readers can immediately see that the last term in Equation (127) again vanishes due to the closed surface  $abc$ , while the first term is indeed the surface integral of the confining stress over the surface  $ac$ . This results in the confining force acting on the

<sup>8</sup> Here we have ignored the interpolation error.

element  $dV$  in the direction opposite to the normal vector  $\vec{n}_2$ . As a result, the additional confining stress term in Equation (123) is simplified to:

$$\mathbf{P}_{\sigma_c}|_i = \sum_{j=1}^N \frac{m_j}{\rho_i \rho_j} (\boldsymbol{\sigma}_{ci} + \boldsymbol{\sigma}_{cj}) \cdot \nabla_i W_{ij} = -\frac{2\boldsymbol{\sigma}_{ci}}{\rho_i} \int_S W_{ij} \vec{n} ds \quad (128)$$

Equation (128) indicates that the confining stress term only works on particles located close to the interface surface of the domain  $\Omega$ , and thus can be used to impose the confining stress to the surface of the domain  $\Omega$ . At this point, the readers may have noticed that the above confining stress is multiplied by 2 and wonders if the above equation exactly reproduces a constant confining stress  $\sigma_c$  on the surface of the domain  $\Omega$ . Our numerical investigation (Zhao et al., 2019) has confirmed that this multiplication is required to exactly reproduce the desirable confining stress. Finally, since all we need in this approach is the locations of particles and a constant confining stress  $\sigma_c$  assigned to all SPH particles, the above method can be applied to any complex and moving surface interfaces without any difficulty. However, in practical applications of SPH, it is recommended that the above confining stress term is only applied to particles located close on the surface area to avoid numerical errors introduced by the errors associated with the SPH kernel estimation. This involves an additional step to specify those particles located close to the confining stress boundary. A straightforward approach to specify these SPH particles is to again make use of the SPH kernel truncation, which results in the following empirical criteria (Zhao et al., 2019):

$$f_i = \begin{cases} \leq 0.55 & \text{in } 2D \\ \leq 0.70 & \text{in } 3D \end{cases} \quad (129)$$

where  $f_i$  is an index parameter calculated by  $f_i = \sum_{j=1}^N m_j / \rho_j W_{ij}$ .

The effectiveness of this approach in capturing a complex moving interface subjected to a constant confining stress can be demonstrated in SPH simulations of a triaxial test shown in Fig. 20. In this test, a cylinder soil specimen with a dimension of 25 mm in diameter and 100 mm in height was subjected to shearing under a constant confining stress of 50 kPa and 100 kPa. The soil was modelled by the general elasto-plastic constitutive model with the Mohr-Coulomb yielding criterion, and the details of which, including all other numerical setting conditions required for SPH simulation, were explained in (Zhao et al., 2019). The confining stress was facilitated by assigning the constant confining stress value (i.e. 50 kPa and 100 kPa, respectively) to all SPH particles at the beginning of the simulation and kept these values unchanged throughout the simulations. Thanks to SPH kernel approximation

features, the confining stress was automatically enforced on all particles located close to the flexible boundary and automatically updated as the sample deformed (Fig. 20). The readers would have noticed that this method does not require any extra computational efforts to determine normal vectors of the confining curvature boundary, which are commonly required in other numerical methods to enforce the confining stress boundary. The loading path was well maintained until the structural failure of the soil specimens occurred (i.e. localised failure) where the stress loading path was slightly off the expected loading path. Nevertheless, it was well maintained under the three-dimensional space, as shown in Fig. 21.

### 3.6. Time integrations

The SPH governing equations written in the form of time-dependent ordinary differential equations can be integrated using standard numerical techniques such as the second-order accurate leapfrog (LF), predictor–corrector and Runge-Kutta (RK) schemes. In practice, the leapfrog algorithm is very popular for its low memory storage required in the computation and the efficiency for one force per step, and hence it is used in all applications presented in this paper. In the LF scheme, field variables ( $\mathbf{A}$ ) such as velocities, density and stresses are advanced at mid-time steps, while the positions ( $\mathbf{x}$ ) are advanced in a full time-steps:

$$\mathbf{A}_{t+\Delta t/2} = \mathbf{A}_{t-\Delta t/2} + \Delta t \left( \frac{d\mathbf{A}}{dt} \right)_{t+\Delta t/2} \quad (130)$$

$$\mathbf{x}_{t+1} = \mathbf{x}_t + \Delta t \left( \frac{d\mathbf{v}}{dt} \right)_{t+\Delta t/2} \quad (131)$$

The stability of the LF time integration scheme is governed by the so-called CFL (Courant-Friedrichs-Levy) condition, which results in a time-step proportional to the smoothing length:

$$\Delta t \leq C_{CFL} h / c \quad \text{with } c = \sqrt{E/\rho} \quad (132)$$

where  $c$  is the sound speed of the material;  $E$  is the elastic modulus of the material; and  $C_{CFL}$  is a constant, which is typically taken to be 0.1.

### 3.7. Parallel computing with SPH

One of the key advantages of SPH in geotechnical applications is its capability to handle large deformation and flow failure behaviour of geomaterials. However, because of the mesh-free nature, the method generally leads to more computational cost and becomes very expensive

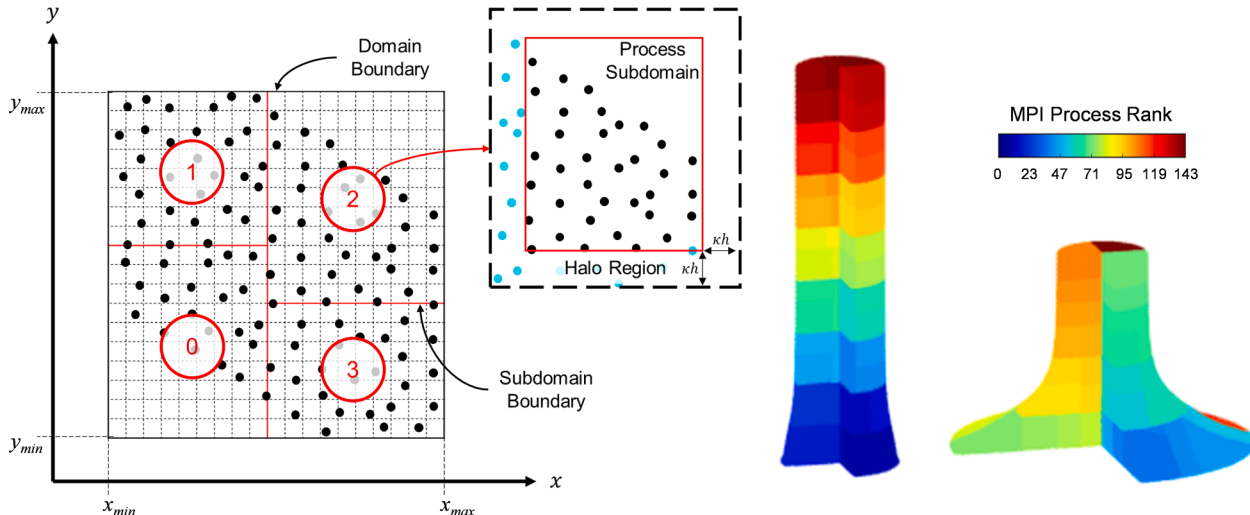


Fig. 22. Computational domain participation strategy in SPH.

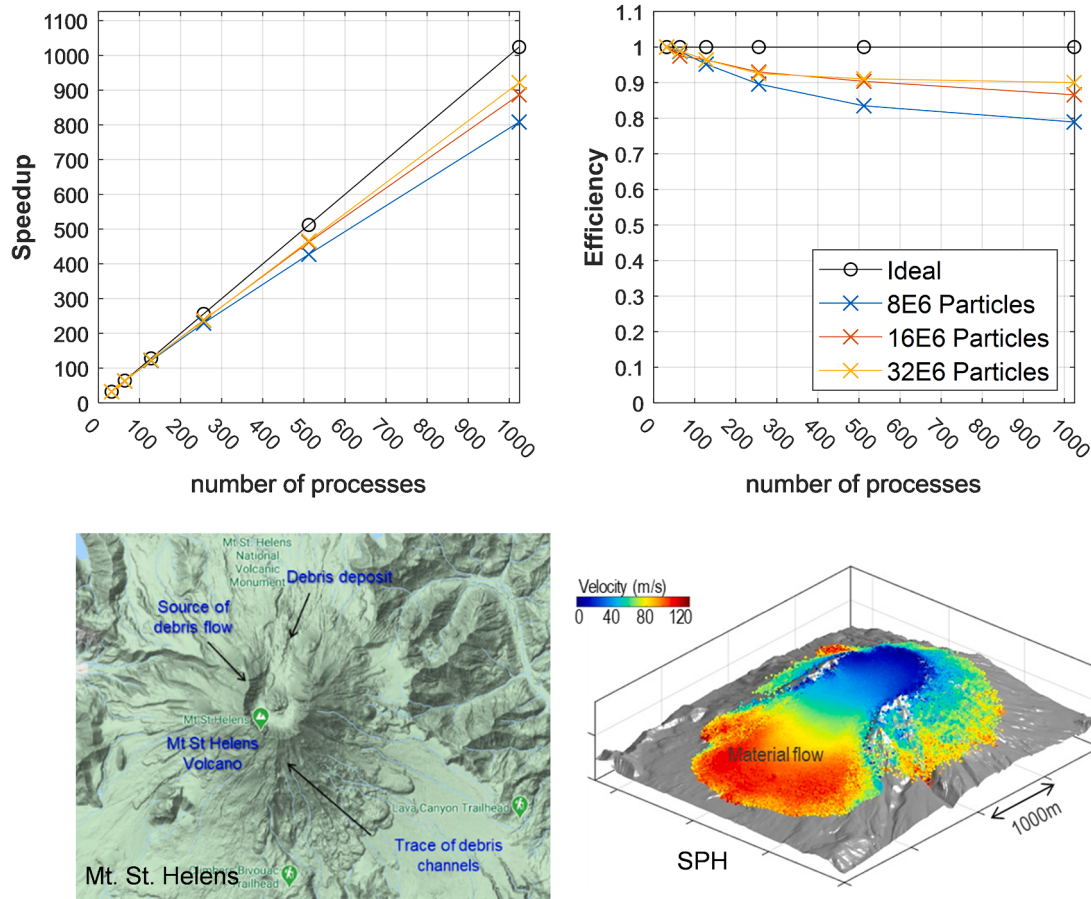


Fig. 23. Computing efficiency and application of SPH to simulate field-scale applications, after (Yang et al., 2020a).

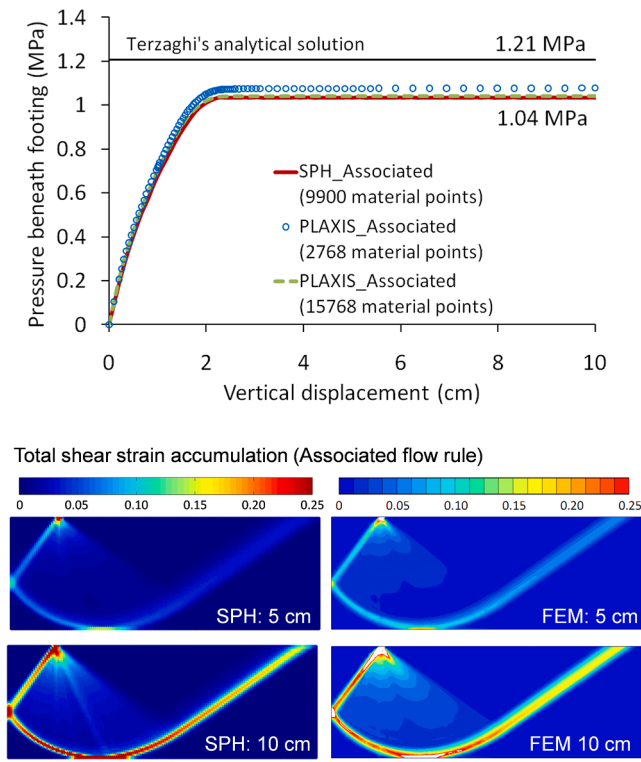


Fig. 24. Comparison between SPH and FEM for bearing capacity problems.

for large-scale applications. In such a case, it is desirable to develop a scalable parallel computing SPH code to broaden its use cases. Of many existing parallelisation approaches (Oger et al., 2016, Valdez-Balderas et al., 2013), which can be used to speed up an SPH code, we are interested in developing distributed-memory parallelism using the Message Passing Interface (MPI). The choice of MPI is common for short-range interaction particle methods such as SPH as it is relatively straightforward to parallelise, allows us to access more computational resources, and can be extendable to hybrid MPI-GPU approaches. The readers are referred to our recent publication in (Yang et al., 2020a) for the detailed algorithm. Here, we only summary key steps required to develop an MPI code and demonstrate the performance of our high-performance MCG-SPH code suitable for large scale geophysical applications. The key steps required to develop a scalable parallel SPH code include:

- 1. Domain participation:** We adopted the Orthogonal Recursive Bisection (ORB) algorithm, which subdivides the domain into bounding boxes whose faces/edges are co-axial with the Cartesian axes and each MPI process is assigned a box (Fig. 22). The boundaries of these domains are updated occasionally, depending on the motion of the particles in the simulation.
- 2. Physical particle distribution:** This step, which occurs every time-step, involves the redistribution of real SPH particles that have crossed subdomain boundaries.
- 3. Halo distribution:** The step involves the redistribution of halo particle information, which also occurs every time-step. The halo particles are copies of real particles that are located within a kernel radius of another subdomain boundary (Fig. 22). Halo particles are necessary for ensuring that real particles within subdomains have the

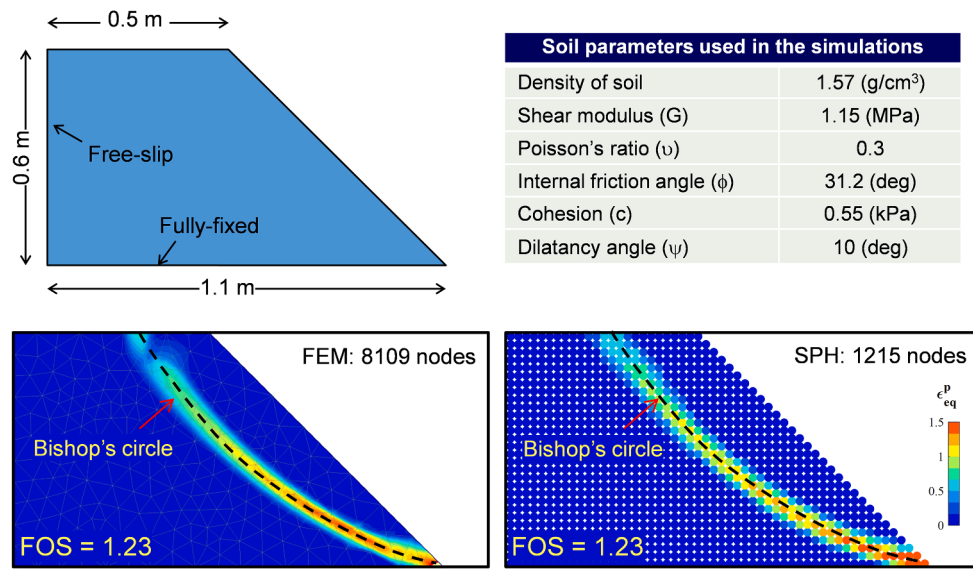


Fig. 25. Comparison between SPH and FEM for a slope stability problem.

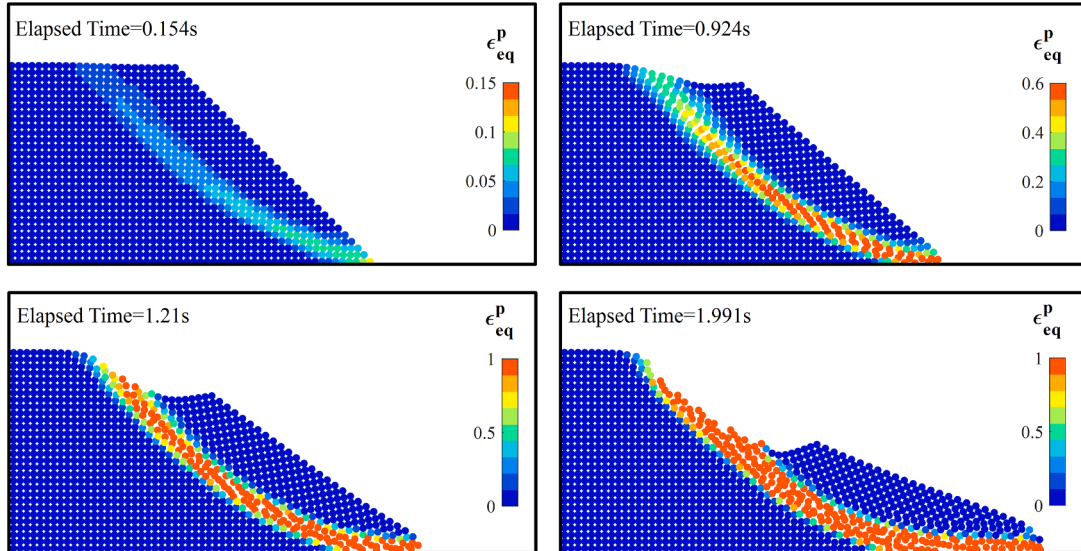


Fig. 26. Modelling the post-failure process using SPH.

necessary particle neighbours to perform SPH interpolations. In some cases, where SPH particles' stress tensor is updated based on strain-rate, a second exchange of information is required to update halo particles' stress tensor.

Fig. 23 demonstrates the efficiency of the code for a test case of 32 million real SPH particles, the parallel scheme obtains a speedup of more than 900 times (~90% efficiency) at 1024 CPU cores (Yang et al., 2020a). A demonstration of a used case is the simulation of the Mt. St Helens debris flow event that occurred in 1980, which involved 2.9 billion cubic meters of deposit over 62 million square meters and over \$3 billion in damages (USD, inflation-adjusted) and 57 lives lost.

#### 4. Some specific applications of SPH in geomechanics

##### 4.1. Traditional geomechanics applications

When it comes to assessing a numerical method, the first question

one could ask is: *how is this method compared with the existing ones?* The finite element method (FEM) is well-known for its capability to predict high-accurate solutions for “**small-deformation**” problems. Therefore, it is a good idea to benchmark SPH against FEM for small deformation problems such as the bearing capacity and slope stability problems. Fig. 24 shows a comparison between SPH (MCG-SPH code) and FEM (PLAXIS) for the prediction of load-bearing capacity and shear-banding development in the soil, which was previously reported in (Bui and Khoa, 2011). In both models, the soil was simulated using an elastic-perfectly plastic model following the Drucker-Prager yield criterion (i.e. associated plastic flow rule). The FEM analysis was conducted using PLAXIS using 15-nodes triangular elements (i.e. a high accurate element). Two PLAXIS FE-models, consisting of 2768 material points and 15,768 material points (i.e. Gauss points), were performed to provide reference solutions for SPH. On the other hand, for the same problem geometry, the SPH simulations adopted 9900 material points. It can see that the SPH method could produce results that are closely matched with FEM models for both the load–displacement curve and the

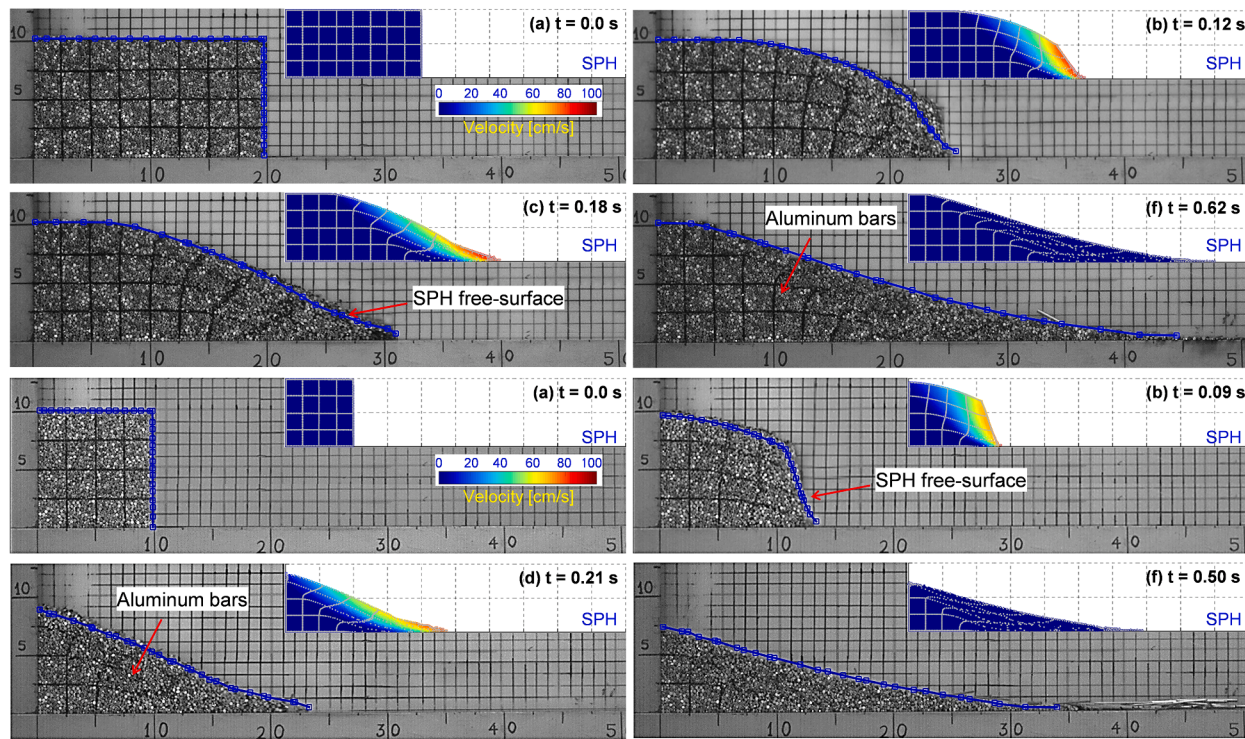


**Fig. 27.** Progressive failure of 2D granular column with the initial aspect ratio  $a = 0.5$  and  $1.0$ . Blue line represents the free-surface extracted from the SPH simulations, after (Nguyen et al., 2020). (For interpretation of the references to colour in this figure legend, the reader is referred to the web version of this article.)

shear band development in the model. The SPH results were closer to the FEM results using finer meshes (i.e. 15,768 material points), demonstrating that SPH could produce results with an accuracy close to that of FEM for small deformation problems. It is worth noting that the above comparison does not mean SPH is more accurate than FEM for small deformation analyses. It simply indicates that any numerical method, including FEM, needs to meet a certain refinement level of spatial discretisation in order to achieve accurate solutions. The accurate FEM solution presented above contains more material points because it uses 15-node triangular elements. In reality, this FEM model only consists of 1314 elements, and thus if we consider each FEM element equivalent to one SPH particle, the spatial discretisation of FEM in this application is much coarser than that of SPH.

The capability of SPH in reproducing results that are similar to FEM for small deformation problems can be further demonstrated through a

slope stability problem. Fig. 25 shows a comparison between SPH and FEM for the stability analysis of a simple cut-slope. In both methods, the simple cut-slope was analysed using an elastic-perfectly plastic constitutive model following the Drucker-Prager yield criterion. The FE model was again analysed using PLAXIS with 15-nodes triangular elements, and the entire slope was represented by 8109 material points (i.e. Gauss points). On the other hand, 1215 SPH particles placed in a square lattice system with an initial equidistance of 0.02 m were adopted in the SPH model to represent the slope, and this is considered as relatively coarse spatial discretisation (i.e. mesh). Ghost particles were adopted to represent the free-slip condition on the vertical boundary, while fixed-boundary particles were used to enforce the fully-fixed boundary. The simulation was conducted using the standard Cubic-spline function. The slope was first subjected to the gravitational load following the procedure described in (Bui and Fukagawa, 2013) to achieve initial in-situ stress conditions. The shear strength reduction method (Bui et al., 2011) was subsequently applied to bring the slope to failure, and the safety factor, as well as the potential failure surface, were recorded. It can be seen from Fig. 25 that SPH could still reproduce the potential failure surface that is very well matched with the result predicted by FEM. Both methods are in good agreement with the potential failure surface predicted by the Bishop's method of slices, and all three methods result in the same factor of safety of  $FOS = 1.23$ . For further applications of SPH for slope stability problems, the readers are referred (Bui et al., 2011, Bui and Fukagawa, 2013).

The above numerical demonstrations reaffirm the capability of the SPH method in reproducing results that are very similar (if not almost identical) to FEM for small deformation problems. However, the key advantage of SPH lies in its capability to simulate the post-failure process of an unstable slope in a more straightforward way, as shown in Fig. 26. Here, to appropriately model the post-failure of the slope, the soil constitutive model is extended to accommodate the softening response of the materials. The Drucker-Prager yield criterion is still adopted to control the yielding condition of the slope soil. However, unlike the elastic-perfectly plastic model, both friction and cohesion of

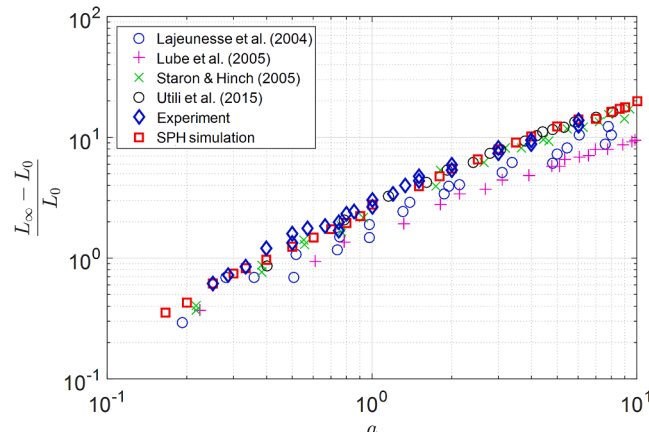


**Fig. 28.** Comparison of the final run-out distances of 2D granular flow with different aspect ratios obtained from experiments and simulations, after (Nguyen et al., 2020).

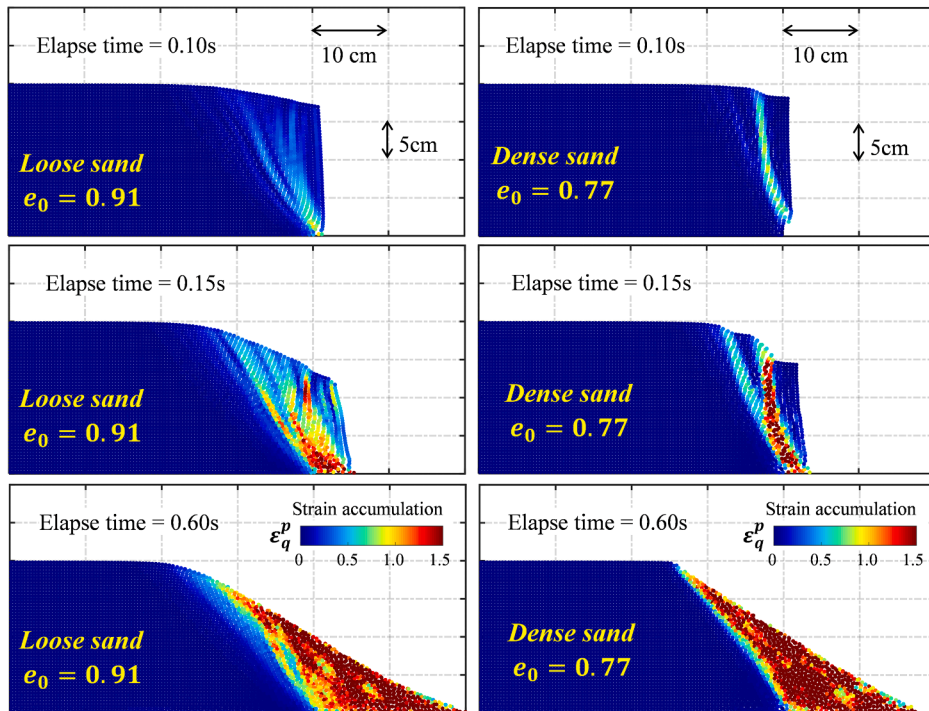


**Fig. 29.** SPH simulations of progressive failure of a 2D granular column collapse test ( $a = 0.5$ ) using an advanced critical state constitutive model for sandy materials. The contour plot represents the deviatoric plastic strain accumulation.

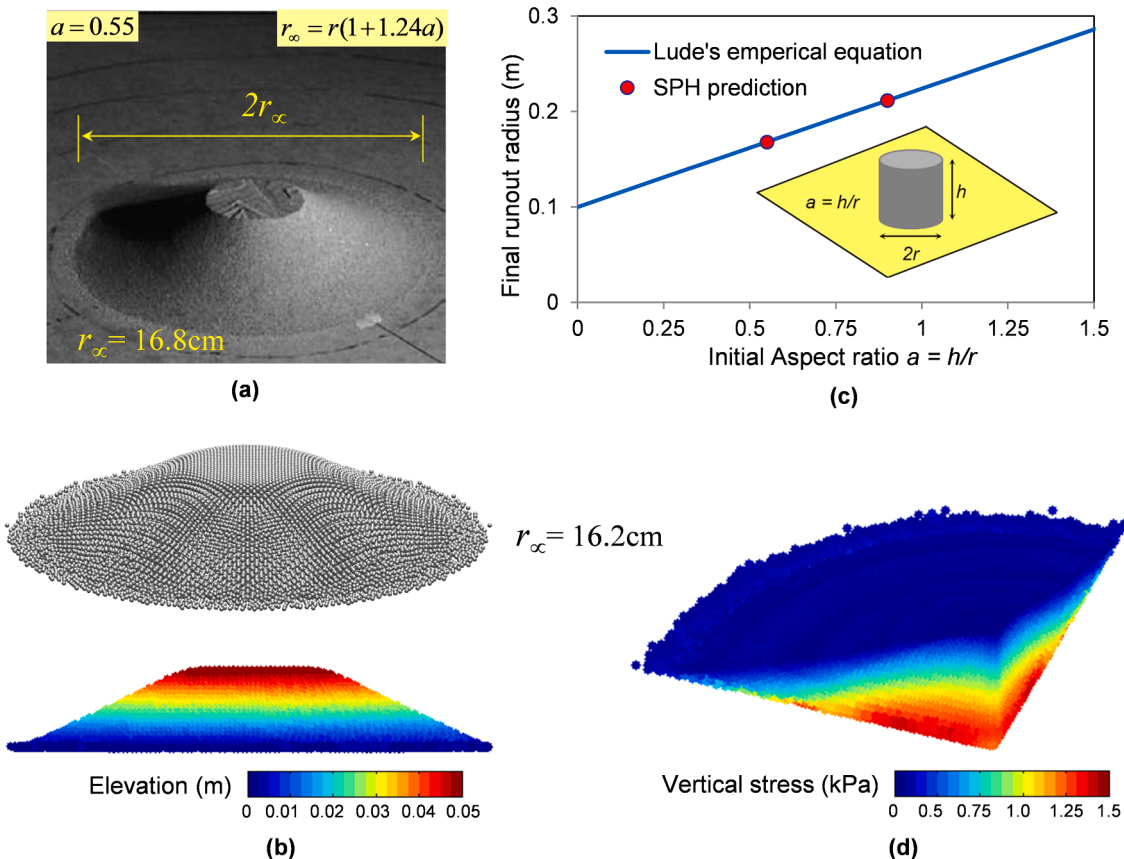


**Fig. 30.** Comparisons between SPH and experiment for the granular column collapse test: (a) Final configuration in experimental (after (Lube et al., 2004)), (b) Final configuration in SPH, (c) Comparision between SPH and experiment for the final runout distance, and (d) Stress profile in SPH simulation.

the soil now degrade with the plastic straining during the post-failure process and can be formulated as a function of the deviatoric plastic strain, which follows Equations (76)-(77). The residual cohesion and friction for this test are set  $\text{toc}_r = 0.1 \text{ kPa}$  and  $\phi_r = 15$  degrees for the testing purpose, and the softening coefficients for cohesion ( $\eta_c$ ) and friction ( $\eta_\phi$ ) are assumed to be the same and equal to 3. The remaining constitutive parameters are similar to those used in the stability analysis of the slope presented in Fig. 25. It can be seen from Fig. 26 that this softening SPH model could capture well the post-failure response of the slope. The localised deformation developed along the potential failure surface failure predicted earlier by both FEM and SPH methods. Subsequently, the shear strength of the material along this localisation zone reduces and thus triggering the global slope failure. The unique capability of SPH in simulating the entire slope failure process, from the initiation to post-failure, is well demonstrated from the above slope failure test. Further examples on this capability of SPH will be demonstrated in the subsequent sections.

#### 4.2. Progressive failure of granular flows

One of the attractive features of SPH is its capability to simulate large deformation and post-failure behaviours of geomaterials. In this section, the capability of SPH in predicting granular flows is demonstrated by presenting the SPH simulations of the granular column collapse experiments, which were previously achieved by using the MCG-SPH code (Nguyen et al., 2020; Bui et al., 2008a; Nguyen et al., 2017a). First, the 2D collapse and deposit morphologies of granular column collapse tests predicted by SPH simulations are compared with the 2D flow experiments of aluminium bars previously reported in (Nguyen et al., 2015). The granular material is modelled by the general elasto-plastic constitutive model following the Drucker-Prager yielding criterion described in Section 3.2.2. Other details of model settings and material properties required for the SPH simulations were reported in (Nguyen et al., 2020). Fig. 27 shows a comparison between SPH simulations and experiments for the progressive collapse of two granular columns with an initial aspect ratios  $a$  of 0.5 and 1.0 (i.e. the ratio of column high to column width), respectively. The SPH model can predict fairly well the collapse process of both granular columns in the experiments, both in term of the evolution of surface morphology and the run-out distance. To further demonstrate the capability of SPH in predicting the run-out distance of granular flows, a series of SPH simulations of granular column collapse tests were conducted for a range of initial aspect ratios (from 0.25 to 10), and the results are compared with data obtained from the 2D experiments (Nguyen et al., 2015) and the literature, as shown in Fig. 28. The SPH results (red squares) agree well with the experimental counterparts (blue diamonds) for the initial aspect ratio  $a$  ranges from 0.25 to 10 and falling well within a range of experimental and numerical data reported in the literature. This suggests that SPH with the Drucker-Prager elasto-plastic constitutive model can predict well the behaviour of granular flows under the plane-strain condition.

To further demonstrate the capability of SPH in simulating the complex behaviour of granular soils undergoing large deformation and

failure responses, the simulation of granular column collapse tests ( $a = 0.5$ ) were repeated using the critical state soil model for sands (Jin et al., 2017), which was previously tested in Section 3.2.4 and demonstrated to work well in SPH. Fig. 29 shows a comparison between the SPH simulations of granular collapse test for two different initial states of density. The results show a strong dependence of the initial density on the progressive failure response of the granular materials. The collapse of the loose sand appears to be faster than that of the dense sand, with the major failure surface (i.e. the boundary between the mobilised mass and undisturbed material) quickly develops and forms deeper into the body of the granular column. Thereafter, the mobilised granular mass above this failure surface starts flowing out and sliding along this surface (i.e. sliding failure). The failure mode appears to be more diffuse with a wider distribution of localised deformation zone across the mobilised granular mass. On the other hand, the dense sand exhibits more localised failure, with the first clear shear band quickly formed at a steep angle, though still slower than that of the loose sand. The dense state nature of sand makes it harden, more dilative and thus difficult to fail. As a result, a strong dilatative behaviour was observed along the first shear band (i.e. the separation between particles increases), and the material above this shear band fails following the avalanching failure mode, rather than the sliding collapse in the loose sand. Once the first mobilised granular mass detached from the granular column, the second shear band formed at a gentle angle, and the mobilised soil mass above this failure surface starts falling down (i.e. avalanching failure mode). Thereafter, the avalanching failure continues to take place until the final failure surface is reached. Compared to the loose case, the final failure surface for the dense case was found to be steeper than that for the loose case, which reflect the nature of dense sand. However, since the same critical state friction angle was adopted in both SPH simulations, the similar final runout distance and final angle of response were expected.

Finally, the capability of SPH in modelling 3D granular column collapse tests was demonstrated in Fig. 30, where the SPH simulations of a cylindrical granular column collapse experiment are compared with the experimental data reported by Lube et al. (Lube et al., 2004). Here, the same SPH model with the Drucker-Prager elastic-perfectly plastic constitutive model described in Section 3.2.2. was extended to 3D conditions and subsequently used to predict the run-out distance of the 3D cylindrical granular column collapse experiments for two initial

**Table 2**  
Physical properties of sensitive clays.

Parameters	Value
Elastic Young's Modulus ( $E$ )	25 Mpa
Poisson's ratio ( $\nu$ )	0.49
Materials density ( $\rho$ )	2.15 g/cm <sup>3</sup>
Undrained peak cohesion ( $c_p^u$ )	25 kPa
Undrained residual cohesion ( $c_r^u$ )	1.5 kPa
Undrained friction angle ( $\phi_u$ )	0 deg
Softening coefficient ( $\eta_c$ )	5

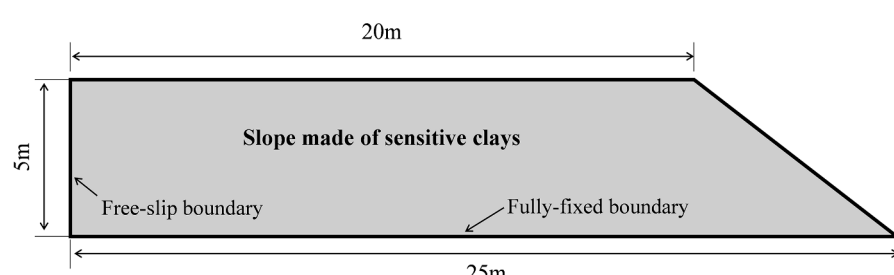


**Fig. 31.** Geometry and boundary conditions of a sensitive clay slope.

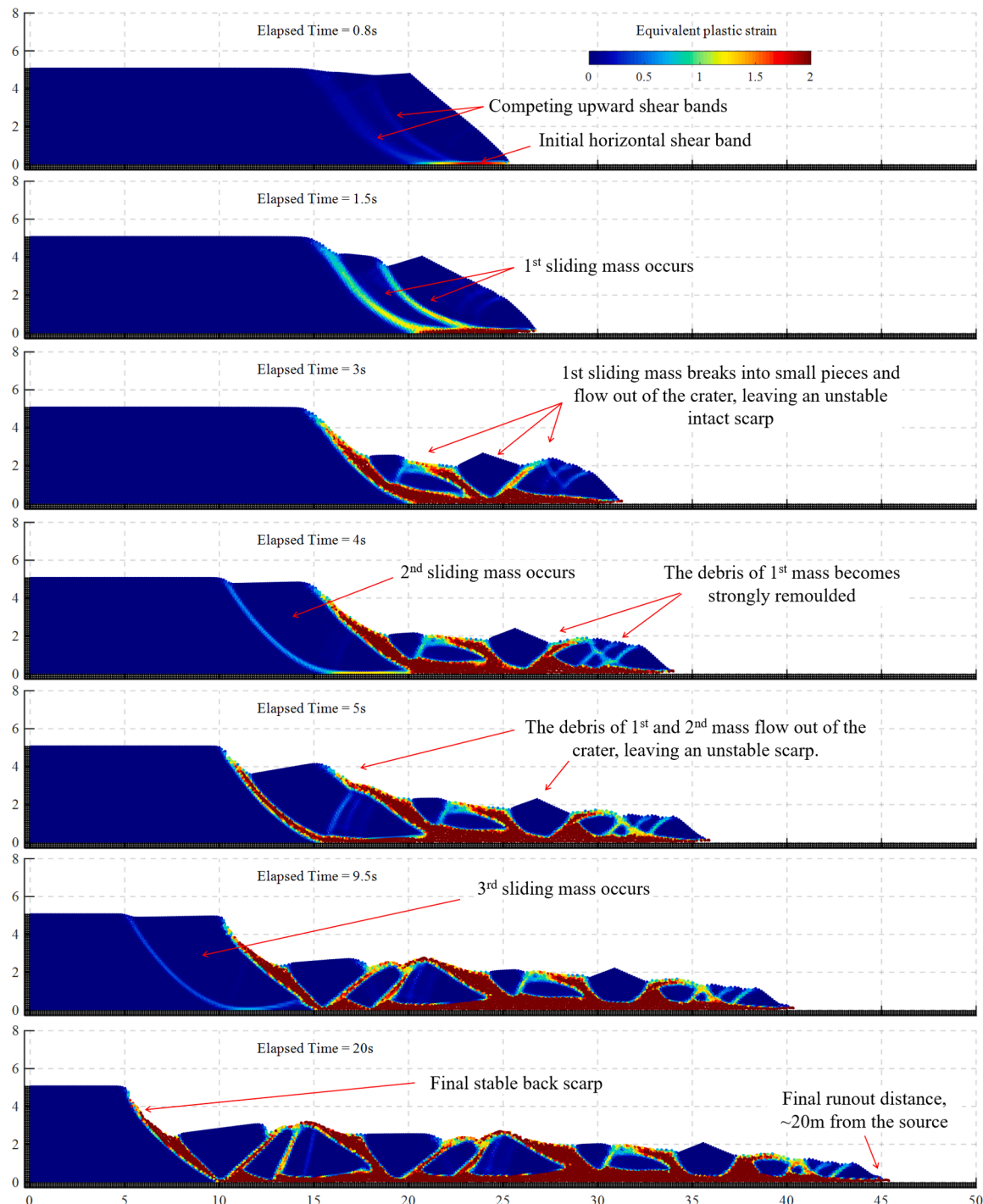


**Fig. 32.** SPH modelling of retrogressive failure of a slope in sensitive clays.

aspect ratios of  $a = 0.55$  and  $a = 0.9$ . The material properties and setting conditions required for the SPH simulations were previously reported (Bui and Nguyen, 2020), some of which were directly taken from the experimental data reported in (Lube et al., 2004). The boundary condition is assumed to be no-slip at the base, and fixed-boundary particles were used to enforce this boundary condition following the method previously reported in (Bui et al., 2008a). Furthermore, to avoid the short-length scale stress noise that appeared in the large shear deformation zone, the stress regularisation technique described in Section 3.3 was adopted. Excellent agreements between the SPH simulation and the experiment are obtained for both the surface

morphology and final run-out distance. The undisturbed zone observed on the top surface of the experiment sample (i.e. for the case of  $a = 0.55$ ) was well captured by the 3D SPH model. Furthermore, smooth distribution of the vertical stress profile across the numerical sample, including the area that underwent large shear deformation, was also achieved, thanks to the stress regularisation technique (Nguyen et al., 2017a).

#### 4.3. Retrogressive failure of slopes in sensitive clays

In this section, the capability of SPH in predicting large deformation

and post-failure of geomaterials is further demonstrated through the modelling of retrogressive failure of slopes in sensitive clays (or quick clays). This type of slope failure frequently occurs in Canada and Scandinavia (Locat et al., 2011), where sensitive clays are commonly found. The modelling and prediction of this type of slope failure is challenging and beyond the capacity of standard numerical methods such as the limit equilibrium methods (LEMs) or FEM. This is because

sensitive clays are well-known for their strain-softening behaviour (i.e. significant reduction of shear resistance with increasing strain from the peak strength). Thus, under undrained conditions, failure in sensitive clays can quickly turn the materials into the semi-liquid or liquid state from their initially very stiff state, causing the materials to travel hundreds of metres away from the initial source (Locat et al., 2011). Furthermore, the retrogressive slope failure in sensitive clays also occurs

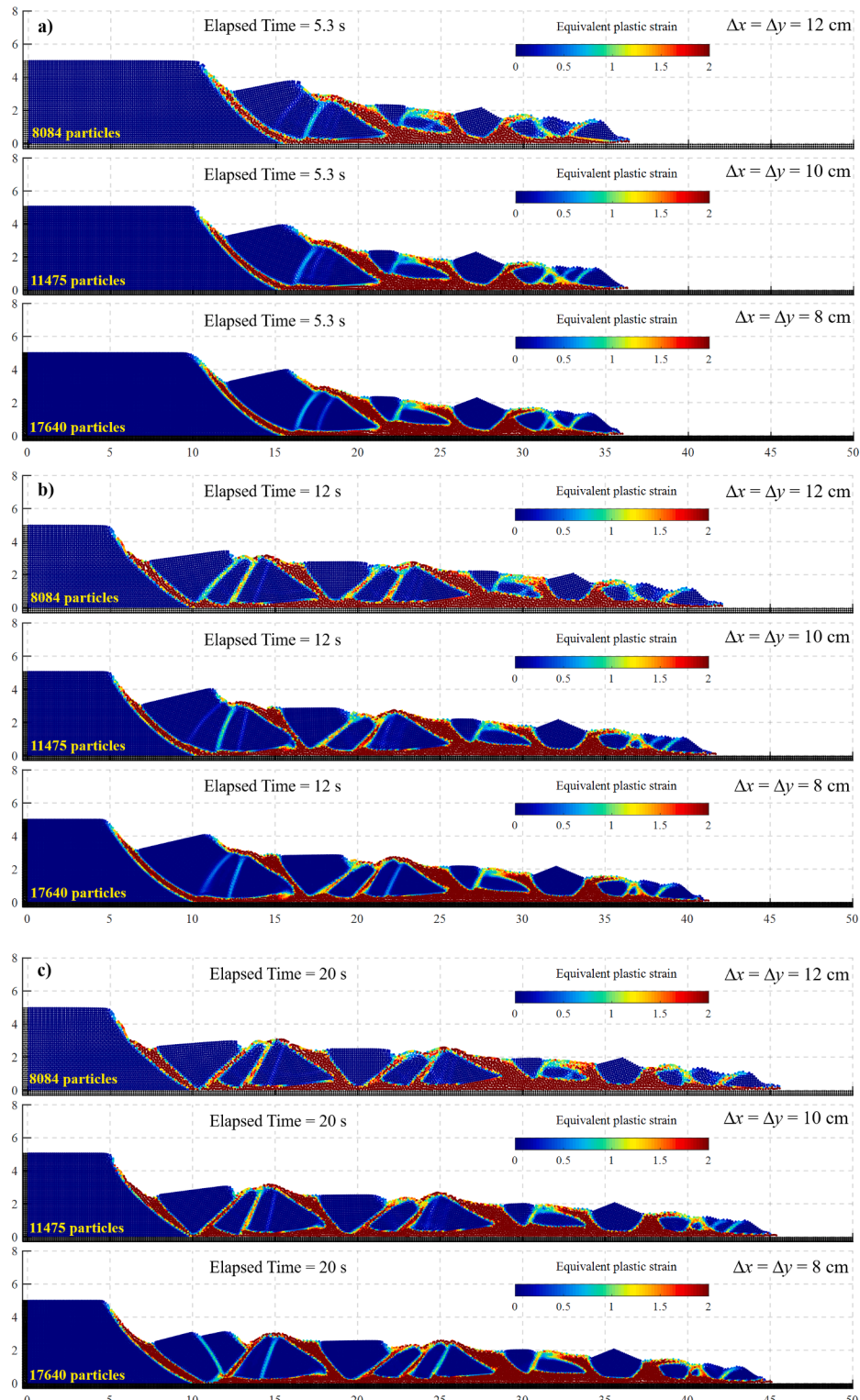


Fig. 33. SPH modelling of retrogressive failure of a slope in sensitive clays.

in a subsequent manner with multiple failure stages, making it impossible to be analysed using mesh-based standard numerical methods. For these reasons, several advanced numerical methods have been applied to analyse this type of slope failure problem with certain successes (Dey et al., 2016, Zhang et al., 2018, Wang et al., 2016a, Jin et al., 2020).

Here, we will demonstrate the capability of SPH in predicting this challenging problem by analysing a hypothesis slope that undergoes retrogressive failure.

The geometry and boundary conditions of the slope is outlined in Fig. 31. The hypothesis slope is 5 m high and 20 m horizontal extent at the base with a slope angle of 45 degrees. The slope is made of a sensitive clay whose material properties are listed in Table 2, which is assumed to be uniformly distributed across the slope for simplicity, although in reality, the undrained shear strength of clay may increase with depth. The simulation is conducted by assuming the undrained condition, which is the common failure condition triggering retrogressive landslides in sensitive clays (Jin et al., 2020). In SPH, the above slope is represented by 11,475 SPH particles (i.e. stress points), which are initially placed in a square lattice with an equidistance of 10 cm. The vertical boundary is modelled using ghost particles, while the horizontal boundary is modelled using fixed-boundary particles (see Section 3.5.1). The free-slip and fully-fixed boundary conditions are enforced following the original method proposed in Bui et al. (Bui et al., 2008a). To model the undrained strength softening behaviour of sensitive clays, the Drucker-Prager constitutive model with strain-softening model described in Section 3.2.2 is adopted, with the undrained friction angle set to be zero ( $\phi_u = 0$ ). This made the Drucker-Prager constitutive model adopted in this section equivalent to the von-Mises model with strength softening behaviour. Furthermore, to achieve the undrained condition, Poisson's ratio is set to 0.49 in this simulation. The simulation was conducted using the Wendland C<sup>2</sup> kernel function, though similar results could be achieved for other kernel functions. The slope is first subjected to the gravitational loading condition to achieve the initial in-situ stress conditions (Bui and Fukagawa, 2013). Subsequently, to reproduce the retrogressive failure mechanism, the slope is brought to collapse by applying a shear strength reduction factor of FOS = 1.65 to the peak strength of the soil slope (Bui et al., 2011), while the residual shear strength is kept unchanged. An alternative approach, which produces similar results and is commonly used in the literature, is to remove a portion of the slope toe, which can be attributed to the internal soil erosion at the slope toe.

The simulation results are illustrated in Fig. 32, demonstrating the capability of SPH in capturing the retrogressive failure of the slope in sensitive clays. This failure process can be briefly described as follows. At first, due to the gravitational load on a highly unstable slope (i.e. FOS = 1.65), the lateral movement of the slope is observed, causing the development of a horizontal shear band at the base of the slope near the slope toe. The horizontal shear band then propagates inward the slope body and up toward the ground surface. Two competing shear bands concurrently develop at this stage and eventually form the first sliding mass causing global failure. At this stage, the strength of the material inside the shear banding zone and at the base of the sliding mass have become strongly remoulded (or significantly reduced) and thus facilitating the movement of the sliding mass. The displacement of the sliding mass further causes localised deformation within it and breaks the sliding mass into smaller pieces with a strongly remoulded strength (i.e. t = 3 s). The debris of the first sliding mass then flows out of the crater and leaving an unstable scarp. Subsequently, the second sliding mass is formed in a way similar to the first sliding mass when the debris of the first sliding mass travel a sufficiently large distance and no longer providing sufficient support to the intact scarp (i.e. t = ~4s). The same failure process was then repeated with the second sliding mass and then the third sliding mass until the final stable scarp is reached. The readers would have noticed that the volumes of the three sliding masses are similar, which can be attributed to the homogenous properties of materials. Also, for this reason, the final stable scarp was reached mainly

because of the debris volume building up at the slope toe of the intact scarp, which provides sufficient support to the intact scarp to prevent it from further collapse. The final runout distance of the soil mass was found to be 20 m from the initial slope toe, which is a significant travelling distance.

At this point, the readers should have noticed that the above SPH simulation adopted the classical strain-softening constitutive model described in Section 3.2.2, which does not contain a material length scale. For this reason, a common question one would ask is: *Could the above SPH model produce the same results for different spatial discretisations of the computational domain (i.e. particle spacing in SPH or mesh-size in FEM)?* In fact, the root to answer this question does not depend on the SPH method, but rather it should reply on the material constitutive model and its capability to accommodate material length scales. It is well-known that, when incorporating with a classical strain-softening constitutive model, FEM suffers from pathological mesh-dependent solutions. Thus, to regularise the mesh dependence of a classical strain softening constitutive model, nonlocal plasticity theory (Pijaudier-Cabot and Bažant, 1987, Chen and Schreyer, 1987, Bažant, 1991) or gradient plasticity theory (Vardoulakis and Aifantis, 1991, Borst and Pamin, 1996) must be used to provide a mean to introduce a length scale to the constitutive model, which enables the material behaviour to correctly scale with the size of the element (or the size of SPH particle). An alternative approach is to replace the classical strain softening constitutive model with the double-scale constitutive framework described in Section 3.2.3, which automatically incorporates a length scale associated with the size of the RVE in the constitutive model, and thus removing all issues associated with the mesh dependence. SPH is not different from FEM (or any other continuum-based numerical method) in the sense that both methods solve the same continuum governing equations (although SPH deals with the strong form while FEM solves the weak form of the governing equations), which incorporate a classical strain softening constitutive model. Accordingly, SPH, in principle, also suffers from pathological spatial discretisation dependences. However, the nature of SPH, which makes use of the kernel interpolation procedure to estimate field quantities required to solve the governing continuum equations (see Section 2.2), automatically introduces a length scale associated with the size of the kernel function into the SPH computational model. In order words, the SPH method itself already possesses a nonlocal feature, which is similar to the nonlocal plasticity theory. Thus, one can make use of this embedded SPH length scale to deal with the mesh-dependent issues when combining with a classical strain softening constitutive model.

To demonstrate the nonlocal feature of SPH, we repeat the above retrogressive slope failure test with different spatial discretisations (i.e. particle spacing). Two additional simulations were conducted using the same classical strain-softening constitutive model, material properties and boundary setting conditions. One simulation with a finer resolution (i.e.  $\Delta x = \Delta y = 8$  cm) contains 17,640 SPH particles, while the other with coarser resolution (i.e.  $\Delta x = \Delta y = 12$  cm) contains 8,084 SPH particles. In all simulations, the Wendland C<sup>2</sup> kernel function is adopted as it has more flexibility in accomodating more neighbouring particles than other kernel functions (see Section 2.3). The particle smoothing length ( $h$ ) is kept unchanged in all three simulations, meaning that  $h$  is set to  $1.2\Delta x$ ,  $1.44\Delta x$  and  $1.8\Delta x$  for the coarse, medium and fine resolutions, respectively. Accordingly, the size of the kernel function or the radius of the supporting domain is fixed at  $R = 43.2$  cm. Here,  $R$  can be interpreted as a length scale inherent with the kernel function used in SPH. Fig. 33 shows a comparison of the SPH simulation of retrogressive slope failure for three different particle resolutions at three different time intervals (5.3 s, 12 s, and 20 s). The readers can immediately see that, even with the classical strain-softening constitutive model, the SPH method produces very similar results with almost identical final runout distances for the three cases at three different time intervals. The number of major shear bands and large broken blocks is also very similar among the three simulations. Nevertheless, there exist some minor

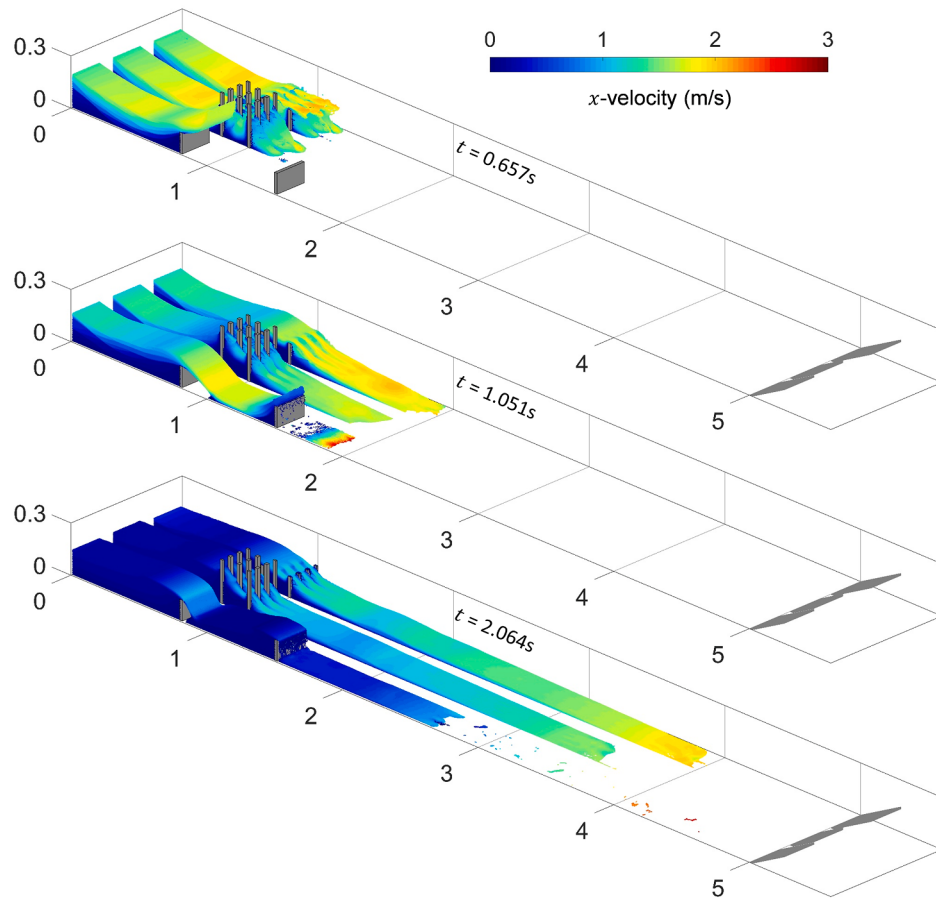


**Fig. 34.** Large-scale SPH simulation of the interaction between debris flows and protective structures, after (Yang et al., 2021) – A comparison among short baffle, tall baffle and check-dams systems.

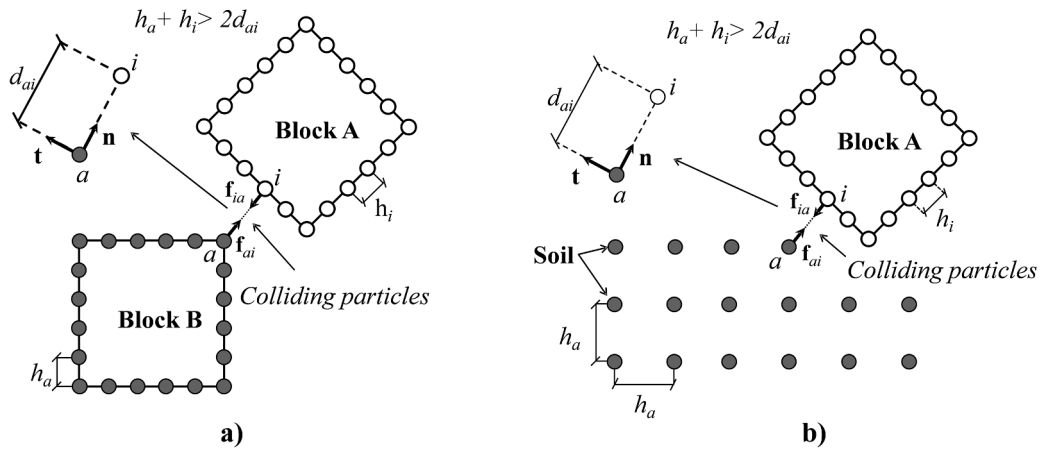


**Fig. 35.** Representation of rigid blocks in SPH and their interactions, after (Bui et al., 2014).

discrepancies among the three cases, particularly toward the end of the sliding process (i.e.  $t = 20$  s, Fig. 33c), where the SPH simulation with the finest resolution appears to be more localised, and thus producing more broken blocks. For example, the largest sliding block located close to the final stable scarp was further split into two smaller pieces in the SPH simulations with 17,640 particles, while this was observed in the SPH simulations (i.e. 8,084 and 11,475 particles). These minor discrepancies are unavoidable for large deformation modelling and can be

attributed to the accumulation of numerical errors associated with the SPH interpolation scheme. Finally, it is noted that, although the above SPH simulations produce qualitatively consistent results for three different particle spacings, these simulations do not properly capture localised failure or shear band development. One obvious reason is that the orientation of the shear band was not described in the constitutive model used and hence anisotropy due to localised failure does not appear at the constitutive level, but at a scale larger than the particle size

governed by the length scale  $R$ . For this reason, to properly capture the localised failure, it is recommended to combine the SPH method with the double-scale constitutive framework described in Section 3.2.3. Some of these works will be demonstrated in the subsequent sections.

#### 4.4. Soil-structure interaction problems

Soil-structure interaction is an interesting and challenging topic that has been extensively investigated in the literature. Given the capability of SPH in predicting large deformation and flow failure of granular materials, as demonstrated in the earlier sections, it is interesting to discuss how SPH can be extended to model soil-structure interactions. First, we will present the application of SPH for large-scale investigations of the interaction between the granular flows and control structures, which were previously reported by the authors in (Yang et al., 2021). In this work, the effectiveness of two control systems, namely baffles and check-dams, in mitigating or slowing down the impact of debris/granular flows was investigated using the high-performance computing MCG-SPH code (Bui et al., 2008a, Yang et al., 2020a). For the details of numerical setting conditions, material properties and validations of this numerical code, we refer the readers to (Yang et al., 2021). Here, several key results are summarised and discussed to highlight the capability of SPH in handling complex soil-structure interaction problems.

Fig. 34 shows the SPH simulation of granular flow impacting against three control systems, namely short-baffles (top), tall-baffles (middle) and check-dams (bottom) (Yang et al., 2021). In the model, the debris flow was modelled using the  $\mu(I)$  rheological constitutive model described in Section 3.2.1, the validation of which was previously reported in (Yang et al., 2021, Yang et al., 2020a) and demonstrated to be suitable for this type of problem. The simulations involve 3.8 million material particles used to generate the granular flow volume and over 800 thousand fixed-boundary particles used to represent the wall boundaries and the control systems. All simulations were run on NCI-Gadi or Pawsey Magnus of the National Computing Infrastructure (NCI), Australia. The readers can immediately see from Fig. 34 that the large-scale SPH model can be effectively used to assess the performance of different control structures without involving substantial costs required to conduct large-scale experiments. For example, the SPH model demonstrates that the tall-baffles system appears to be more effective than the short-baffles system, and there exists a critical height above which the baffle system does not gain more benefit. The check-dams control system appears to be better in slowing down the debris flows. However, if one looks at the total forces acting on the check dams, it is an order of magnitude larger than the individual baffle of the same

height as the dam experiences (Yang et al., 2021).

At this point, the readers would have asked what if we have deformable or moving rigid structures and how one can extend the current SPH model to simulate the interaction between soils and such systems. In fact, these applications of SPH were previously reported in (Bui et al., 2014, Bui et al., 2008b, Wang and Chan, 2014) in 2D conditions and were recently extended to 3D conditions (Zhan et al., 2020, Zhan et al., 2019). Here, we will discuss how SPH can be used to model the interaction between soil and moving rigid structures, as in the segmental (or concrete block) retaining wall system, which is commonly used in practice to reinforce soil slopes due to its capability to tolerate minor ground movement and settlement without causing significant damage to the retaining wall structure. To model this type of problems, one would need to find a way to represent the retaining wall blocks in SPH as well as to describe their rigid body motions in SPH. Such an SPH model was previously reported in Bui et al. (Bui et al., 2014), which can be dated back to the original work by Monaghan (Monaghan et al., 2003), and will be briefly summarised here. In their SPH model, the retaining wall blocks (or rigid structures) are simulated by placing SPH boundary particles on the surface boundary of each wall block, as shown in Fig. 35. The dynamic motions of retaining wall blocks can be then described through the motion of their central mass, which obeys Newton's second law. The translational and rotational motion equations for the centre of mass of a block can be written as follows:

$$M_k \frac{d\mathbf{V}_k}{dt} = \sum_{i \in S_k} \mathbf{f}_i \quad (133)$$

$$I_k \frac{d\Omega_k}{dt} = \sum_{i \in S_k} (\mathbf{r}_i - \mathbf{R}_k) \times \mathbf{f}_i \quad (134)$$

where  $M_k$  and  $\mathbf{V}_k$  are the central mass and vector velocity of block  $k$ ;  $I_k$  and  $\Omega_k$  are the inertial moment and angular vector velocity about the centre of mass of block  $k$ ;  $\mathbf{f}_i$  is the force vector acting on boundary particle  $i$  representing the block; and  $\mathbf{r}_i$  and  $\mathbf{R}_k$  are vector coordinates of boundary particle  $i$  and the centre of mass of block  $k$ , respectively.

The readers could see from the above SPH model that the centre for the description of the rigid body motion of the concrete blocks (or solid structures) is the formulation of a suitable contact force model to compute the interaction force  $\mathbf{f}_i$  between the block-block (Fig. 35a) or soil-block (Fig. 35b). The simplest way to compute this force is to adopt the penalty force approach, in which a spring-dashpot system is used to generate repulsive forces acting on the solid structures or the soil when they approach each other. Bui et al. (Bui et al., 2014) proposed the following contact force model, which accounts for the change in the

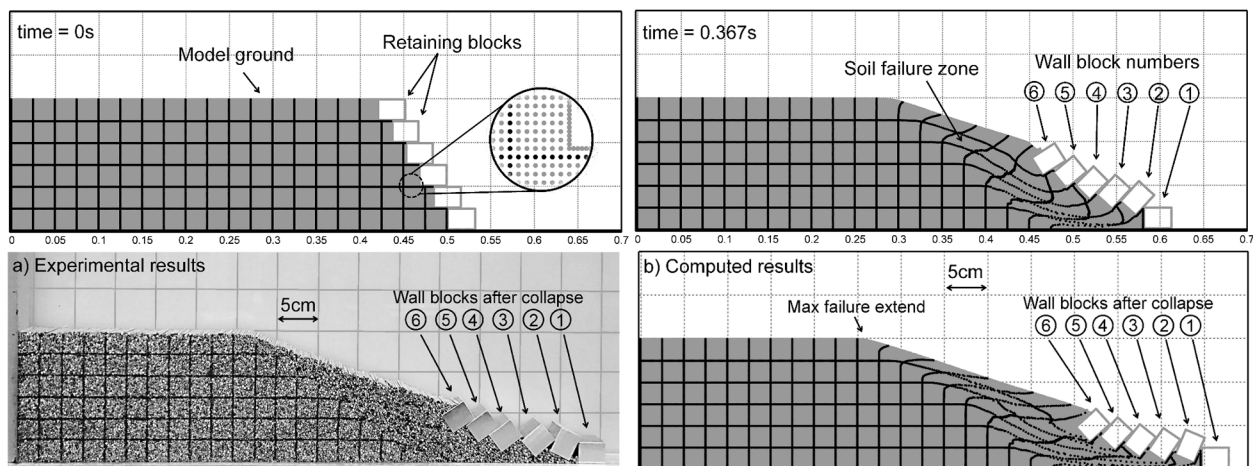
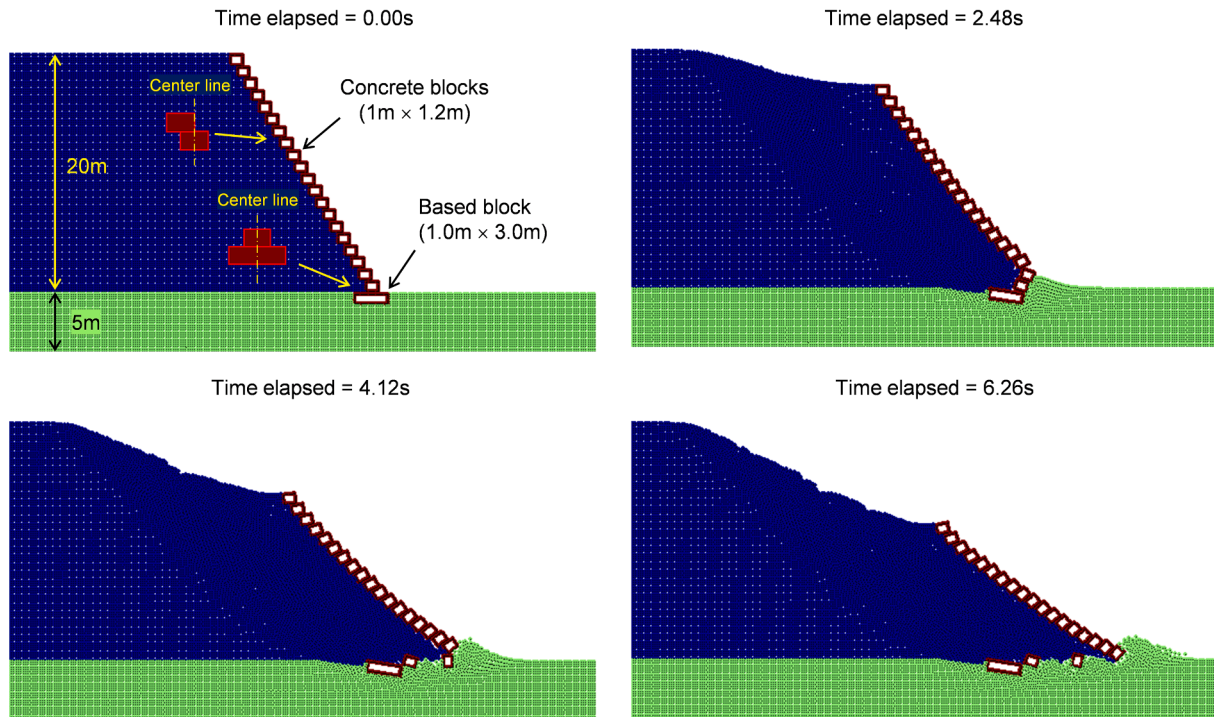


Fig. 36. SPH simulation of the progressive collapse of a retaining wall system consisting of six rigid wall blocks and its comparison against experiment, after (Bui et al., 2014).



**Fig. 37.** SPH simulation of progressive failure of a high retaining system consisting of multiple concrete wall blocks reinforced at the base.

number of SPH boundary particles used to represent the rigid structures:

$$\mathbf{f}_{a \rightarrow i} = \begin{cases} -\frac{K_{ai}\delta_{ai} - c_d v_{ai}}{N_C} & 2d_{ai} < (h_a + h_i) \\ 0 & 2d_{ai} \geq (h_a + h_i) \end{cases} \quad (135)$$

where  $\mathbf{f}_{a \rightarrow i}$  is the contact force vector between particles  $a$  and  $i$ ;  $K_{ai}$  is the contact stiffness, which can be either specified from experiments or estimated by the Hertz's contact theory (Bui et al., 2014);  $\delta$  is the vector of relative displacement between particles  $a$  and  $i$ ;  $c_d$  is the damping coefficient, which is a function of the damping ratio and contact stiffness (Bui et al., 2014);  $d_{ai}$  is the distance between particles  $a$  and  $i$ ;  $h$  is the initial distance between two SPH particles; and  $N_C$  is the number of contact points (or number of boundary particles on the block  $k$ ), for which the contact was detected. The shear or tangential contact force must satisfy Coulomb's friction law, which requires:

$$\mathbf{f}_{a \rightarrow i}^t \leq \mu_w \frac{\delta_{ai}^t}{|\delta_{ai}^t|} |\mathbf{f}_{a \rightarrow i}^n| \quad (136)$$

where  $\mu_w$  is the interface frictional coefficient of the rigid structures, and the indexes  $n$  and  $t$  indicate the radial and tangential vectors between particles  $a$  and  $i$ , as shown in Fig. 35.

Finally, once the contact model is formulated, and the translational and rotational velocities of the central are specified, the motion of boundary particles on each block can be updated as follows:

$$\frac{d\mathbf{r}_i}{dt} = \mathbf{V}_k + \Omega_k \times (\mathbf{r}_i - \mathbf{R}_k) \quad (137)$$

The application of the above SPH framework to model the soil-structure interaction problem involving the progressive collapse of six segmental retaining wall blocks and its comparison against the experiment is shown in Fig. 36, which was previously reported in (Bui et al., 2014). The simulation involves 45,208 SPH particles used to represent the soil, which was modelled using an elastic-perfectly plastic constitutive model following the Drucker-Prager yield criterion. Each retaining wall block is treated as a rigid body with full degrees of motion in 2D and is represented by a set of boundary particles, as outlined in Fig. 35. The distance between these boundary particles was taken to be half of the spacing between real soil particles, although in principle, the more

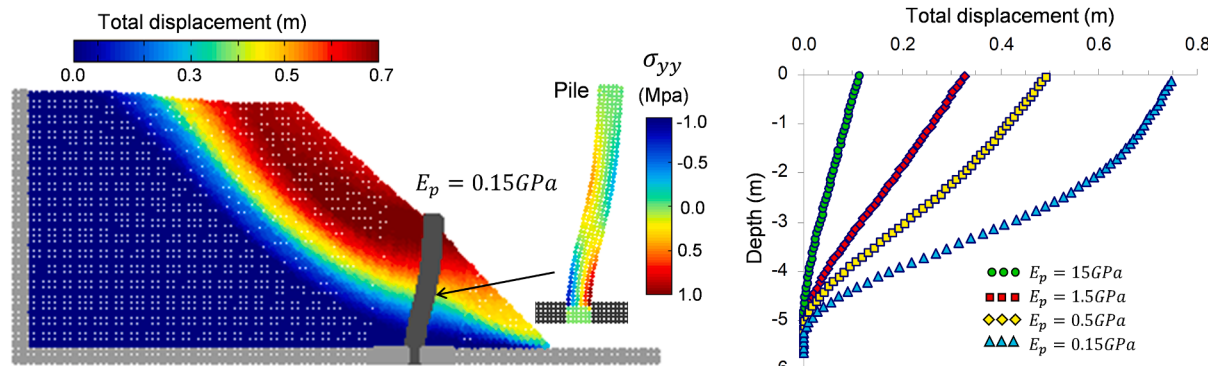


**Fig. 38.** SPH modelling of the soil-pile interaction, after (Bui et al., 2008b).

boundary particles, the better representation of solid boundary. The above contact force model presented in Equation (135) automatically accounts for the changes of the contact number as the number of particles representing the rigid block increases. All material properties and interface friction coefficients required for the simulations were measured from the experiments specifically designed to test this SPH model (Bui et al., 2014). It can be seen that the SPH model can capture well the dynamic movement of each retaining wall block, and very good agreement with the experiment was achieved, suggesting that the SPH method could be straightforwardly extended to model the complex soil-structure interaction problems.

Further application of this SPH model to a high retaining wall structure consisting of multiple rigid blocks is illustrated in Fig. 37, showing the capability of SPH in modelling a highly complex soil-structure interaction system. This type of retaining wall system is commonly found in Japan, where large concrete blocks (of various shapes and sizes) are often used to form a retaining wall system to stabilise slope-cut against frequent earthquake events. In this simulation, the collapse of a retaining wall system formed by large concrete blocks was simulated. The retaining wall system was designed to support a 45-degree sandy slope-cut of the following soil properties: density of 1.6 g/cm<sup>3</sup>, shear modulus of 38.5 MPa, Poisson's ratio of 0.3, and internal friction angle of 25 degrees. The slope-cut was founded on the soil foundation of the following properties: density of 2.0 g/cm<sup>3</sup>, internal friction angle of 35 degrees, cohesion of 10 kPa, and sharing the same elastic properties as the soil slope. The density of the concrete block is 2.4 g/cm<sup>3</sup> and the interface friction is assumed to be 0.5 between the block-block and block-soil, simply taken for the testing purpose. The soil was modelled using the same elastic-perfectly plastic constitutive model following the Drucker-Prager yield criterion. It can be seen from Fig. 37 that, because of the very steep and high slope-cut, the retaining wall system was unable to stabilise the slope, leading to the progressive failure of the entire retaining wall systems. The failure initiated at the slope toe, where the first block slides over the base-block. Subsequently, due to the high interface friction between retaining wall blocks, two blocks at the base start to overturn, causing the unbalance of above concrete blocks and leading to the complete collapse of the retaining

wall system. Three blocks at the bottom were buried inside the soil mass and undergone both translational and rotational motions during the slope collapse process. These complex soil-structure interaction mechanisms could be straightforwardly captured by the above SPH framework, thanks to the truly mesh-free nature of SPH.

Finally, if one wishes to model the interaction between soil and deformable structures, the above SPH framework can be straightforwardly applied by further considering the deformation of the solid structure, which can be either modelled as an elastic or an elasto-plastic materials following the general constitutive framework described in Section 3.2.2. Early application of SPH to model soil-structure interaction was reported in Bui et al. (Bui et al., 2008b), as shown in Fig. 38, in which both soil and pile were modelled using the general SPH framework described Section 3 (i.e. Lagrangian SPH framework), which should be differentiated from the total Lagrangian SPH or updated Lagrangian SPH models (Vignjevic et al., 2006; Vidal et al., 2007). The soil was modelled by the Drucker-Prager elastic-perfectly plastic model, while the pile was treated as an elastic material. A coupling condition that assumes continuous velocity and stress conditions across the soil-structure interface was adopted. Furthermore, a frictionless contact model was adopted to prevent soil particles from penetrating the solid structure. This model was able to well capture the influence of pile stiffness on its response in reinforcing a slope-cut, as shown in Fig. 38, and a smooth contour distribution of stress on the pile was able to achieve, thanks to the coupling conditions. It is worth noting that there exists several alternative approaches in the literature to model the soil-pile interaction problem, or in general, the interaction between soils and deformable structures. For example, one could adopt the total Lagrangian SPH approach (Vignjevic et al., 2006) to model the pile, which is more accurate and robust because it requires less computational costs to update the contact list, and the numerical results are less sensitive to the particle disorder. A coupled SPH-FEM approach, in which SPH is used to model soil while FEM to model the structure, is another option that can explore the advantage of FEM in modelling solid structures undergoing small deformation. These are beyond the content of this review and are subjected to future research.

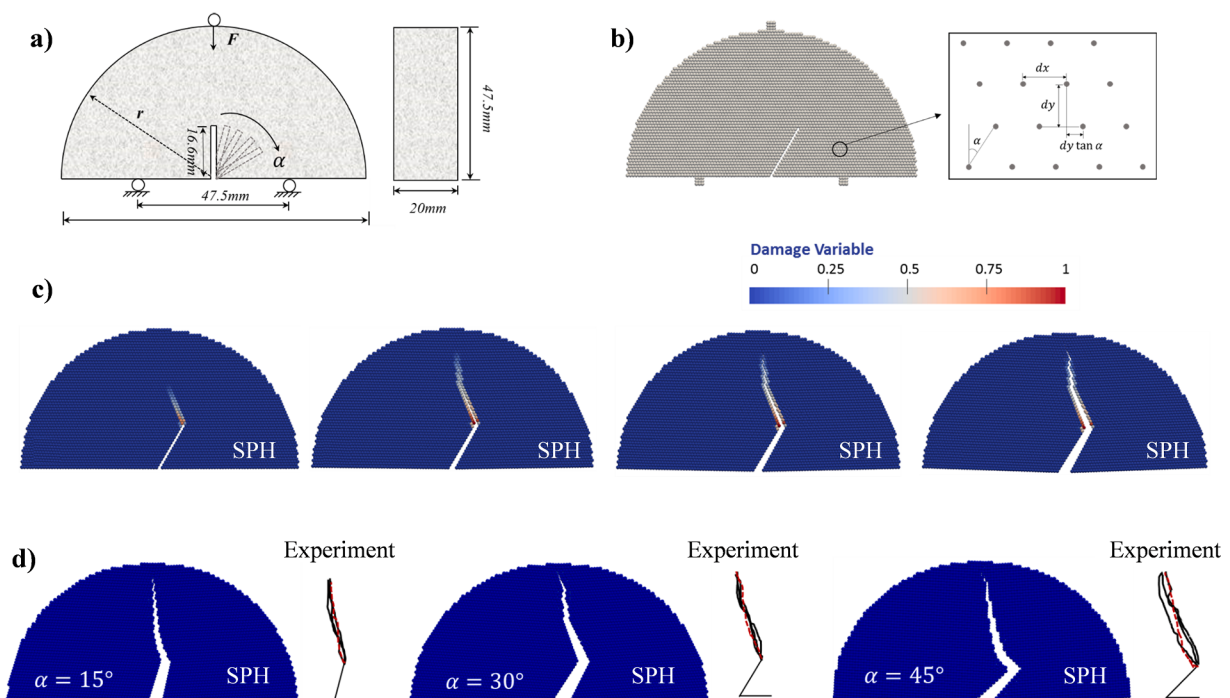


**Fig. 39.** Modelling of fracture development in the semi-circular bending test using the double-scale SPH model, after (Wang et al., 2020).

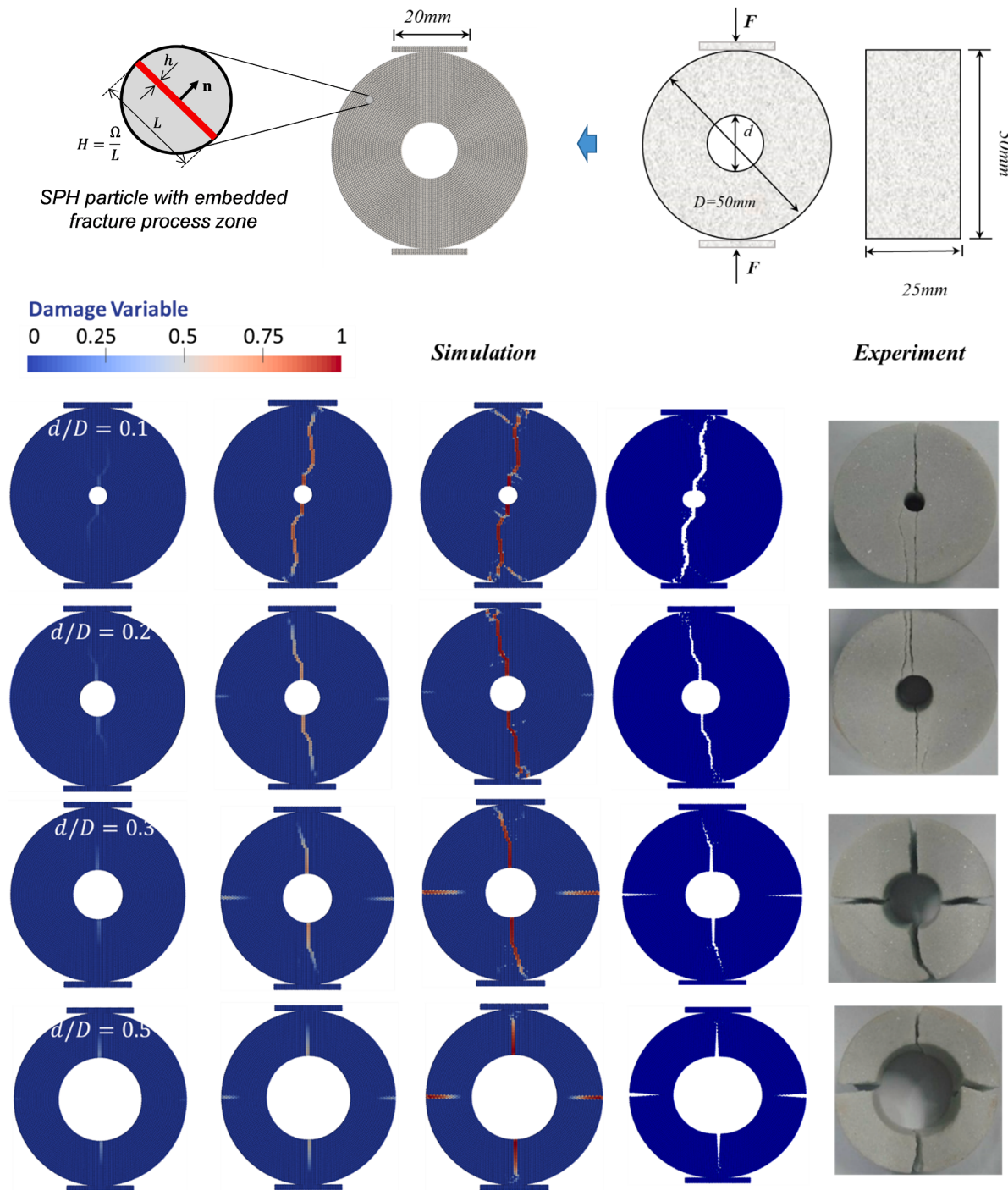


**Fig. 40.** Comparison between SPH simulations and experiments for the final fracture patterns developed in the splitting test of circular rings with different inner-to-outer diameter ratios, after ([Wang et al., 2020](#)).

#### 4.5. SPH applications to fracturing in geomechanics

The capability of SPH in modelling complex fracturing problems in geomechanics is demonstrated in this section. These works were previously reported in ([Wang et al., 2020](#), [Tran et al., 2019](#), [WANG, TRAN, 2019b](#)), which combine the standard SPH framework presented in Section 3.1 and the novel double-scale constitutive model with an embedded fracture process zone (i.e. localised failure zone) described in Section 3.2.3. As demonstrated in earlier works ([Wang et al., 2020](#), [Tran et al., 2019](#)), the key advantage of this double-scale SPH modelling approach over existing continuum-based modelling approaches is its

capability to naturally capture the initiation and propagation of complex fracture patterns without requiring any predefined or explicit representation of fracture topologies and orientations. This was achieved by making use of “cracked” SPH particles, each of which possesses its own fracture process zone whose behaviour is controlled by local stress conditions and material properties. Furthermore, thanks to the characteristic length scale related to the size of the fracture process zone (and controlled by the fracture energies used in the cohesive-frictional model), the double-scale SPH framework is independent from the spatial discretisation of the computational domain.

First, the capability of this SPH model is demonstrated through the

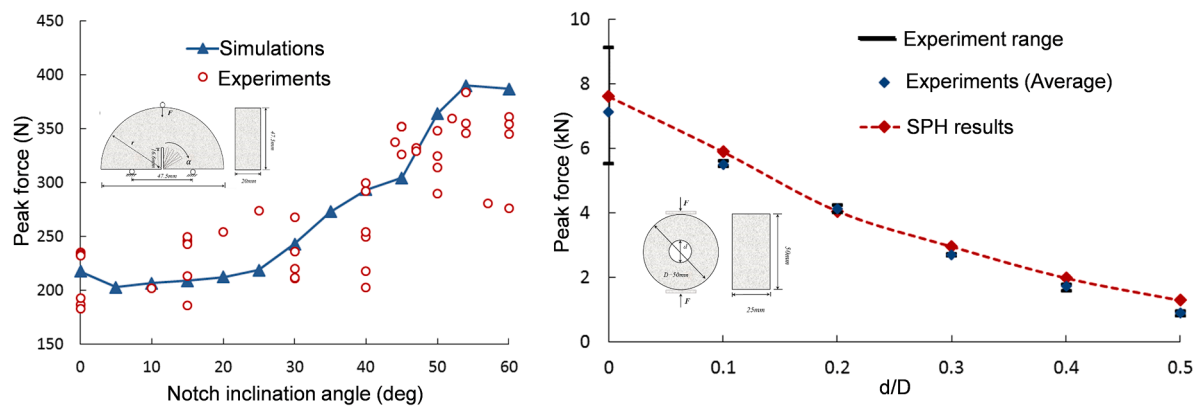


**Fig. 41.** Comparison between SPH and experiment for the predictions of peak force and fracture toughness in the semi-circular bending test and the splitting test of circular rings, after (Wang et al., 2020).

modelling of rock fracture problems involving mixed-mode failure. Fig. 39a shows the geometry and boundary conditions for the semi-circular bending test, which was previously reported in (Wang et al., 2020). The corresponding SPH model is shown in Fig. 39b, which requires approximately 4000 SPH particles placed in such a way to produce accurate notch angles. Each SPH particle is then assigned with fracture properties (see (Wang et al., 2020) for details) and behaves following the double-scale constitutive model described in Section 3.2.3 (i.e. the special case for  $f \rightarrow 0$ ) incorporated with a mixed-mode cohesive fracture law, which was detailed in (Wang et al., 2020) along with its stress return algorithms. The test was then started by vertically loading the numerical specimen by assigning a constant loading velocity of  $-2\text{ mm/s}$  to the top roller, which was modelled by three layers of boundary particles. The numerical results for a semi-circular rock specimen with a notch inclination angle of  $30^\circ$  is illustrated in Fig. 39c, with the damage variable of 1 representing a completely damaged SPH particle. The readers can see that the double-scale SPH model could capture very well the initiation and propagation of fracture developed in the numerical specimen. In particular, the fracture is initiated at several SPH particles located at the notch tip and propagated to other SPH particles toward the loading point (i.e. the top roller). A curvilinear fracture formed by a set of cracked SPH particles was finally formed in the middle of the sample when the fracture propagates and reaches the loading point, at which the numerical specimen was completely broken into two halves. Further tests for different notch angles were also conducted, and the comparison between these SPH simulations and experiments for the prediction of fracture patterns is shown in Fig. 39d. The excellent agreements with experiments demonstrate the capability of the double-scale SPH framework in capturing the fracture development under complex loading conditions. At this point, the readers could have asked if the SPH particles are actually cracked in the current double-scale SPH framework. In fact, the SPH particle itself could not be cracked visually in the current numerical framework and no particle splitting is needed. The “cracked SPH particle” term was only used to indicate the SPH particle undergoes damage process through the fracture process zone embedded on the RVE represented by the SPH particle. As a result, the decrease in the strength of the SPH particle is linked to the development of a damage variable on the fracture process zone carried by the SPH particle itself and each SPH particle has its own damage variable ranging from 0 to 1. The overall effect is the large displacement between two sides of a crack due to underlying cracking inside the fracture process zone embedded in the particles. In other words, splitting at the scale above the particle scale is governed by the particle behaviour with an embedded fracture process zone, and discretisation dependent solutions are guaranteed (see Section 3.2.3).

Another example to further demonstrate the capability of the double-scale SPH framework in predicting fracture pattern under complex

loading conditions is shown in Fig. 40, which were also reported in (Wang et al., 2020) where the double-scale SPH framework was used to predict the fracture development in the splitting test of circular rings. The challenge in predicting this test is that the development of fracture in the circular ring specimens is dependent on the size of the inner ring. In particular, for marble rocks, (Li et al., 2016) reported that a single crack would develop in the experimental specimen along the loading direction (i.e. vertical crack) and split the sample into two fragments when the inner-to-outer diameter ratios ( $d/D$ ) is less than 0.3. On the other hand, two cracks are formed (i.e. vertical and horizontal cracks) and split the specimen into four fragments when the inner-to-outer diameter ratios ( $d/D$ ) is greater or equal to 0.3. It was also reported that the vertical crack develops from the inner ring to the outer ring, while the horizontal crack starts the edge of the outer ring and propagates toward the surface of the inner ring. These observations were consistent with a similar study reported in (Hobbs, 1965). Using the material properties of marble rocks, the SPH simulations of the splitting test of circular ring were conducted for various inner-to-outer diameter ratios. The readers are referred to (Wang et al., 2020) for the details of material properties and numerical setting conditions. It can be seen from Fig. 40 that the double-scale SPH model could predict very well the failure mechanisms of circular rings observed in the experiments. For the inner-to-outer diameter ratio of less than 0.3 (i.e.  $d/D \leq 0.2$ ), the SPH results show a single vertical crack (i.e. primary crack) initiated from the inner ring along the central loading line and propagated toward the loading zones on the top and bottom of the specimen. As the inner-to-outer diameter ratio increases beyond 0.3 (i.e.  $d/D \geq 0.3$ ), both the primary crack and secondary crack (i.e. horizontal crack) were form in the numerical specimens. In contrast to the primary crack, the secondary crack is initiated from the outer ring and propagated toward the inner ring, but always lagging behinds the primary crack. The good agreement between SPH and experiment was not only observed in the failure patterns, but also the predicted peak loads as shown in Fig. 41. For the semi-circular bending tests, the SPH simulations predicted the mean value of the reported data, while very close agreements with the experiments was achieved for the splitting test of circular rings. These differences can be attributed to the quality of experimental data as well as the availability of material properties required for the SPH model reported in those experiments. Overall, the above results show very good agreements between the SPH simulations and experiments, suggesting that the combination of SPH with the two-scale constitutive model with an embedded fracture process zone could capture well the fracture developments in rocks or rock-like materials.

At this point, the readers would have asked if the double-scale SPH framework can handle more complex problems involving multiple cracks or crack branching. To make this happen, the double-scale constitutive model with an embedded fracture process zone (i.e. the

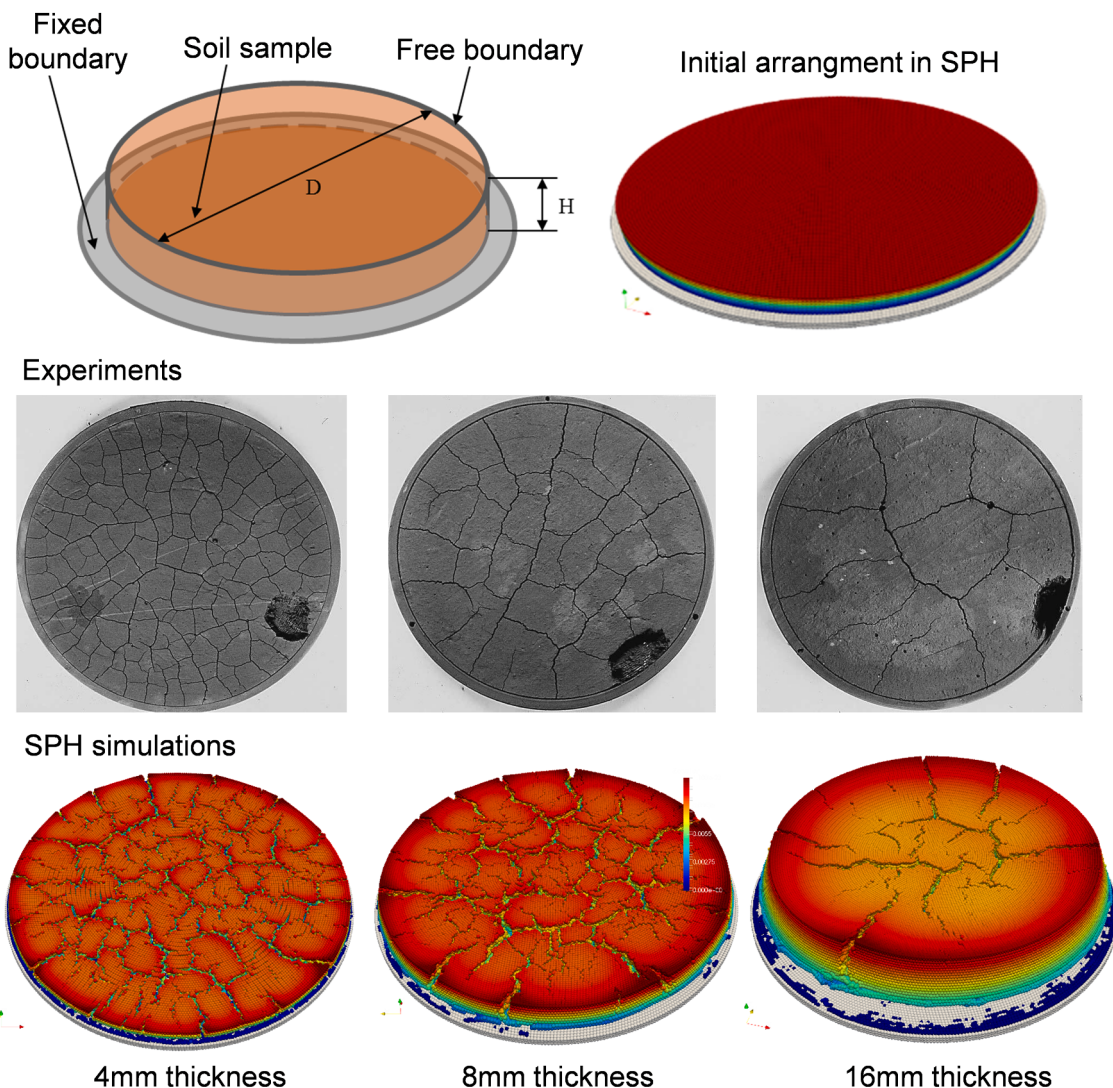


**Fig. 42.** Comparison between the SPH simulation and experiment for the prediction of desiccation induced cracking in clays, after (Rodríguez et al., 2007) and (Tran, 2019b).

special case for  $f \rightarrow 0$ ) described in Section 3.2.3 needs further enhancement. In particular, the double-scale constitutive framework presented in Section 3.2.3 only considers one fracture plane (or one localisation zone) developed in the representative volume element (RVE). In reality, depending on the stress loading conditions acting on the RVE, more than one cracks may develop in the RVE. In this case, it is possible to insert more cracks into the RVE and the proposed general double-scale constitutive framework described in Section 3.2.3 is flexible enough to accommodate more cracks. For example, the extension of the above double-scale constitutive framework to allow two cracks developed in an RVE was presented in (Le et al., 2018) and demonstrated to be able to capture complex stress loading conditions. Although more cracks can be added to the RVE to increase the flexibility of the constitutive model in handling complex stress loading conditions, it has been proven from our own experience that this is not necessary as it significantly increases the complexity of the constitutive model. For practical applications, it is recommended that not more than three cracks should be inserted into the RVE to avoid complication of the constitutive model. Alternatively, if one considers a hypothesis that once the RVE with a single fracture plane is completely damaged and splits into two fragments, each fragment can be then considered as a new intact RVE and can carry the load again, in this case, there is no need to

insert a new fracture plane into the RVE; instead a simpler approach is to reset the damage variable of each RVE when it reaches the full damage state. In particular, in the SPH simulations, damaged SPH particles naturally move to one side of the crack and once cracking is completed (indicated by damage reaching 1), these SPH particles are attached to one side of a crack with a crack opening large enough to stop or at least minimise their interactions across the crack in the SPH framework. Each side of an opening crack can then be considered “intact” again and damage reset to zero to reflect that. Such a hypothesis has been implemented in the SPH method to model the development of complex fracture networks in clays undergoing shrinkage cracking (Tran, 2019b).

Fig. 42 shows the comparison between the SPH simulations and experiments conducted by Rodriguez et al. (Rodríguez et al., 2007). Both experiment and simulation involved three circular slurry clay specimens (metallurgical waste) of thickness 4 mm, 8 mm and 16 mm and a diameter of 64 mm subjected to a drying process. In the experiment, the drying process was caused by supplying a constant heat source on the sample surface, while in the simulation, the drying process was simulated by imposing a volumetric shrinkage strain on all SPH particles instead of modelling the actual moisture evaporation process. The rate of volumetric shrinkage strain applied to SPH particles was assumed to decrease linearly from 2% (at the top layer) to 1% (at the bottom layer),

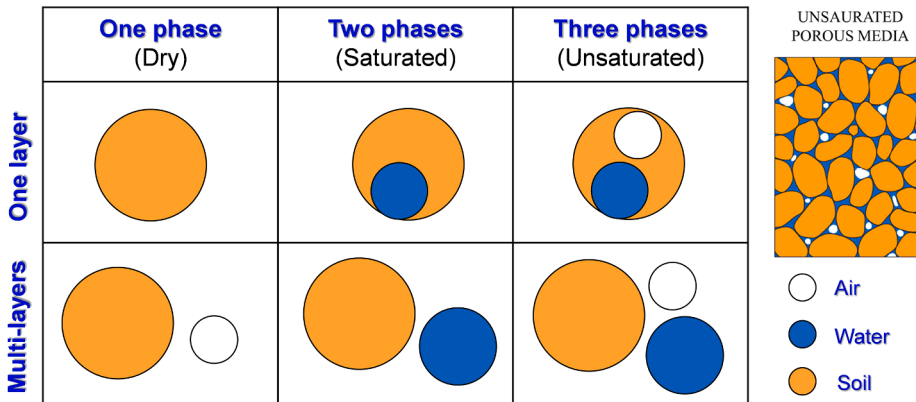


**Fig. 43.** Different strategies to solve multiphase flow problems in SPH.

which was recommended in the previous study (Tran et al., 2020). The double-scale SPH framework presented in Section 3.2.3 was adopted, incorporating the above hypothesis of “intact” particles on one side of a crack. The boundary conditions are set to fully restrained at the bottom boundary while fully-free at all other boundaries. The readers are referred to (Tran, 2019b) for further details of material properties and numerical setting conditions. It could be seen from Fig. 42 that the SPH model with the simplified double-scale constitutive model could predict the multiple fracture networks developed in the numerical specimens, and the simulation results are in qualitatively agreements with those observed from the experiments. In both experiment and simulation, the crack density was found to decrease as the sample thickness increases, suggesting that the soil thickness governs the development of cracks and crack spacing in the soil sample. These results are also consistent with the previous continuum modelling using SPH with different constitutive models (Tran et al., 2019, Bui et al., 2015) and FEM-based mesh fragmentation technique (Sánchez et al., 2014), which requires explicit representation of fracture topologies and orientation through cohesive interface element, or discontinued modelling approaches (Gui et al., 2016, Sima et al., 2014).

#### 4.6. Modelling flows through porous media and coupled flow-deformation in geomechanics

In this final section, we will demonstrate the capability of SPH in modelling multi-phase/multi-physical problems associated with the passage of fluid flows through deformable porous media. To achieve this goal, the SPH governing equations described in Section 3.1 will be generalised to accommodate the interaction among phases in the porous media. In general, the governing equations of a multiphase mixture (assuming an isothermal system) consists of the mass and momentum balance equations, which can be written as follows (Bui and Nguyen, 2017):

$$\frac{d^a \bar{\rho}_a}{dt} + \bar{\rho}_a \nabla \cdot \mathbf{v}_a = \hat{m}_a \quad (138)$$

$$\bar{\rho}_a \frac{d^a \mathbf{v}_a}{dt} = \nabla \cdot \bar{\sigma}_a + \bar{\rho}_a \mathbf{b} - \sum R^{a\beta} \quad (139)$$

where  $\mathbf{v}_a$  is the velocity vectors of phase  $a$  in the mixture;  $\bar{\rho}_a = n_a \rho_a$  is the partial density of phase components in the mixture corresponding to the volume fraction  $n_a$ ;  $\hat{m}_a$  is the mass exchange rate per unit volume;  $\bar{\sigma}_a = n_a \sigma_a$  is the partial stress of each phase  $a$  in the mixture; and  $(d^a/dt)$  denotes the material derivative of a field quantity ( $\pi$ ) on phase  $a$ , which can be written in a general form as follows:

$$\frac{d^a \pi}{dt} = \frac{\partial \pi}{\partial t} + \mathbf{v}_a \cdot \nabla \pi \quad (140)$$

The above governing equations for a multiphase mixture are general and can be further extended or simplified to specific applications such as fluid-saturated porous media, unsaturated porous media or internal erosions. The central to these applications is to find a robust way to approximate the partial differential operators or to convert the partial differential governing equations into the ordinary differential governing equations, which are solvable, and different numerical methods have different ways to achieve this goal. To solve the above governing equations by SPH, one needs to discretise these equations onto SPH particles using suitable SPH operators, as discussed in Section 2. This forms the basics of two existing SPH approaches to solve multiphase flow problems in geomechanics, as outlined in Fig. 43. In the first approach (i.e. single-layer approach), a single set of SPH particles is used to represent the multiphase porous media, which in general consists of air, water and solid. Each SPH particle then carries the information of three phases, and the fully coupled governing equations of these phases are solved in this single set of SPH particles (Bui and Fukagawa, 2009, Pastor et al., 2009). In the second approach (i.e. multiple-layers approach), two or three sets of SPH particles are used to represent the porous media (Bui et al., 2005, Bui and Nguyen, 2017, Bui et al., 2007, Bui et al., 2006a, Maeda et al., 2006). The governing equations of each phase are then solved separately on each set of SPH particles, and the interactions among phases are considered through several coupled physical processes (Bui and Nguyen, 2017, Bui et al., 2005, Bui et al., 2007, Maeda et al., 2006).

Here, we will present the general two-phases multi-layers SPH approach for solving coupled fluid-solid problems in the fully saturated porous media. In our view, this is one of the most rigorous multi-layers SPH models for multiphase flow through deformable porous media, considering the fully coupled hydro-mechanical processes. The simplified version of this framework for a constant spatial distribution of porosity was previously reported in Bui and Nguyen (Bui and Nguyen, 2017), which can be dated back to the earlier works reported in (Bui et al., 2005, Bui et al., 2007, Maeda et al., 2006). The governing equations for water (i.e. assuming a non-viscous fluid) and solid phases in a fully saturated porous system (i.e. assuming no mass loss) can be derived from the above general mixture theory. For the water phase, the following governing equations hold:

$$n_w \frac{d^w (\rho_w)}{dt} = -\rho_w \nabla \cdot (n_s \mathbf{v}_s + n_w \mathbf{v}_w) \quad (141)$$

$$\bar{\rho}_w \frac{d^w (\mathbf{v}_w)}{dt} = -\nabla (n_w p_w) + \bar{\rho}_w \mathbf{g} + \mathbf{R}^{ws} \quad (142)$$

and the governing equations for the solid phase are:

$$\frac{d^s n_s}{dt} = -n_s (\nabla \cdot \mathbf{v}_s) \quad (143)$$

$$\frac{d^s(\mathbf{v}_s)}{dt} = \nabla \cdot (\boldsymbol{\sigma}' - n_s p_w \mathbf{I}) + \bar{\rho}_s \mathbf{g} - \mathbf{R}^{ws} \quad (144)$$

where the superscript  $w$  and  $s$  represent the water and solid phases, respectively;  $\boldsymbol{\sigma}'$  is the effective solid stress;  $p_w$  is the pore-water pressure; and  $\mathbf{R}^{ws}$  is the interaction seepage force between the water and solid phases, which is defined by:

$$\mathbf{R}^{ws} = -\frac{\gamma_w n_w^2}{k_w} (\mathbf{v}_w - \mathbf{v}_s) + p_w \nabla n_w \quad (145)$$

where  $\gamma_w$  is the specific unit weight of the water; and  $k_w$  is the water permeability coefficient, which can be estimated from the porosity following the Kozeny-Carman equation (Bui and Nguyen, 2017). It is noted here that if the spatial variation of the porosity distribution is assumed to be very small and negligible (i.e.  $\nabla n_w = 0$ ), the above governing equations can be simplified to the two-phase flow SPH framework previously reported in Bui and Nguyen (Bui and Nguyen, 2017).

Next, to solve the above governing equations, one would need to adopt appropriate time integration schemes. Bui and Nguyen (Bui and Nguyen, 2017) suggested that the governing equations for the solid phase can be solved following the standard leapfrog (LF) time integration scheme described in Section 3.6 after being fully discretised using appropriate SPH operators as discussed in Section 2. On the other hand, the governing equations for the water phase should be solved using the predictor–corrector scheme, which was originally proposed by Shao and Lo (Shao and Lo, 2003) to model incompressible fluid in SPH. On the one

hand, this predictor–corrector scheme allows to model the water phase as an incompressible fluid, which enables achieving a stable pore-water pressure profile in SPH by solving the pressure Poisson's equation (Bui and Nguyen, 2017). The other key reason is that this approach offers great flexibility to couple solid deformation with the water flow. To demonstrate this flexibility, let's us briefly revisit the application of the predictor–corrector scheme to solve the above governing equations for the water phase. In the first prediction step, an intermediate temporal velocity of the water phase ( $\mathbf{v}_w^*$ ) is estimated by solving the momentum equation of the water phase, i.e. Equation (142), without considering the pore-water pressure gradient:

$$\mathbf{v}_w^* = \mathbf{v}_w^t + \left[ \mathbf{g} - \frac{\gamma_w n_w^2}{k_w} (\mathbf{v}_w - \mathbf{v}_s) \right] \Delta t \quad (146)$$

where  $\mathbf{v}_w^t$  is the vector velocity at time  $t$  and  $\Delta t$  is the incremental time. The temporal velocity ( $\mathbf{v}_w^*$ ) is then used to estimate the temporal density of the water phase by solving Equation (141):

$$\rho_w^* = \rho_w^t - \frac{\rho_w^t \nabla \cdot (n_s \mathbf{v}_s + n_w \mathbf{v}_w^*)}{n_w} \Delta t \quad (147)$$

Here, the change in water density was influenced by the deformation of the solid phase, which indicates the coupling effect at the intermediate stage. Next, the correction step is required as the influence of the pore-water pressure gradient was not considered in the first prediction step. The corrected water velocity can be obtained by further considering the contribution of the water pressure gradient:

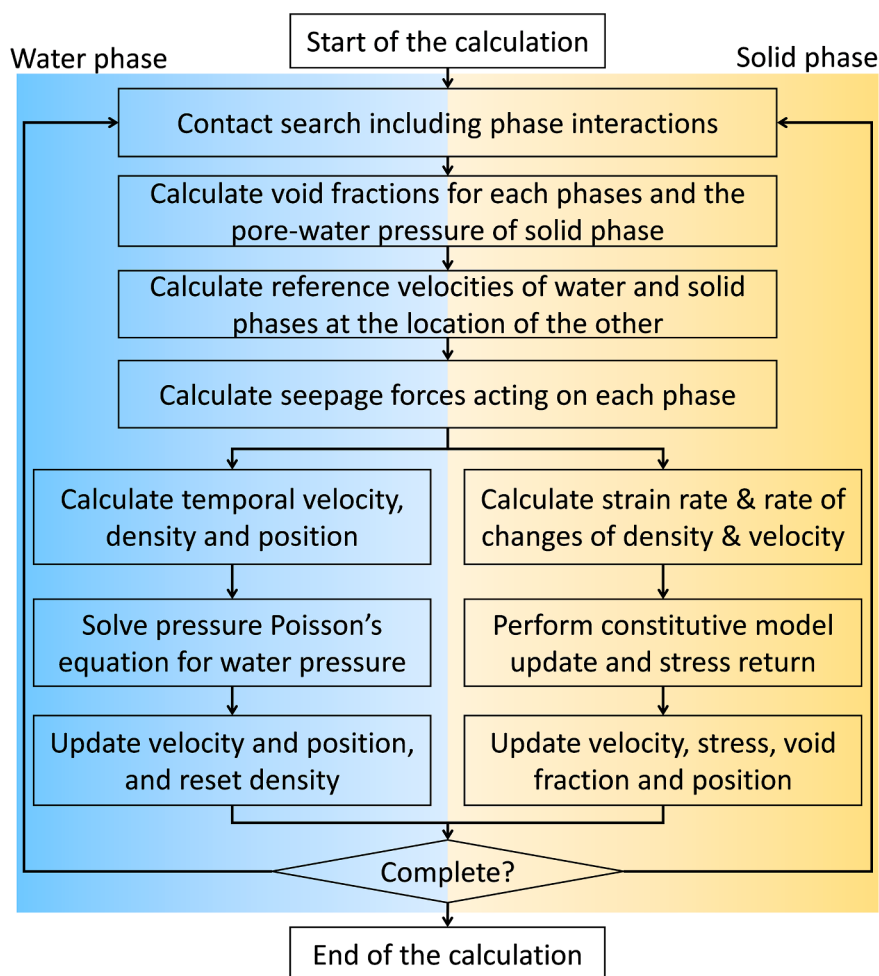


Fig. 44. SPH algorithm for solving coupled fluid–solid problems in the two-phases multi-layers SPH framework, after (Bui and Nguyen, 2017).

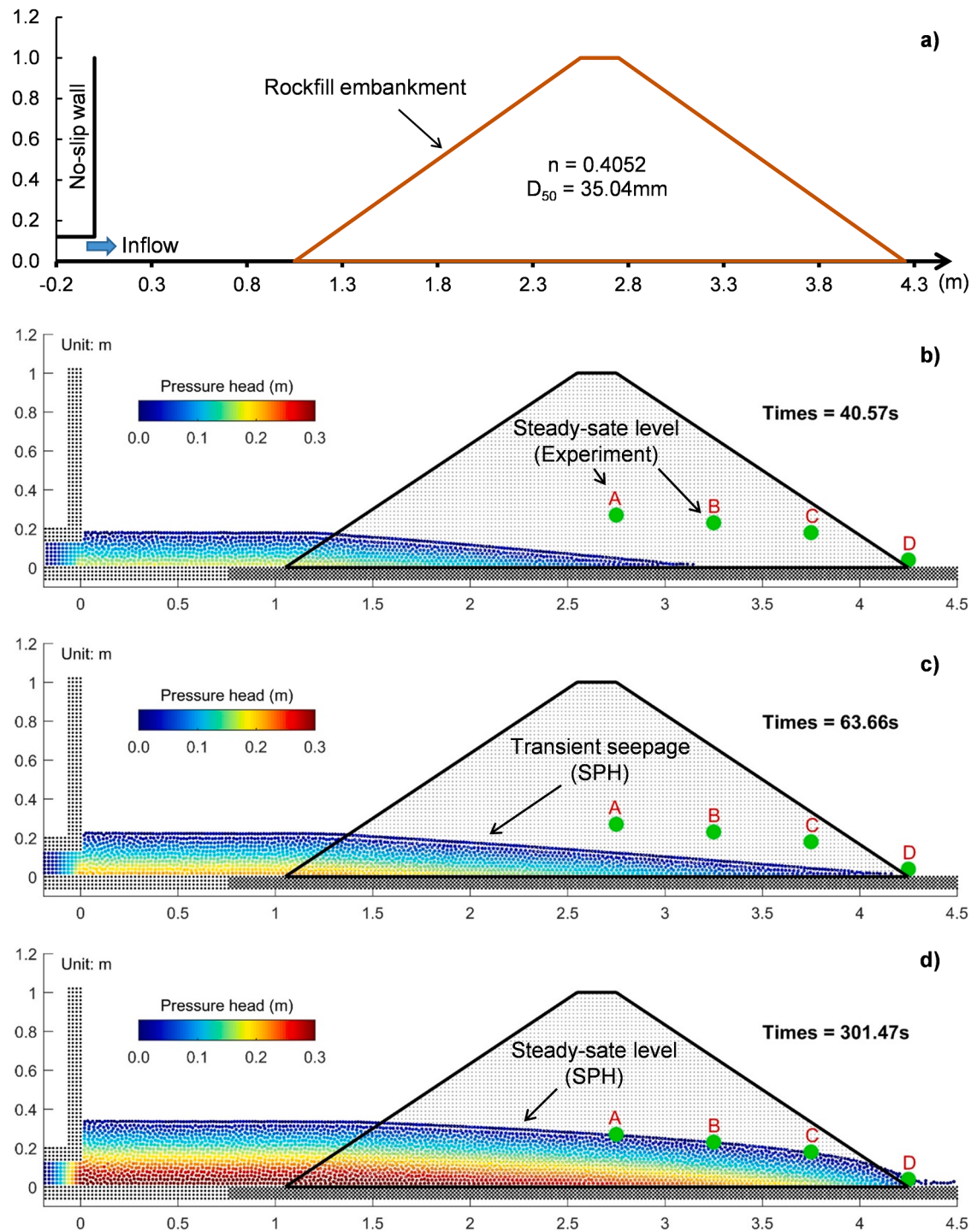


Fig. 45. Modelling of seepage flow through rock-filled dam using the two-phases multi-layers SPH framework, after (Bui and Nguyen, 2017).

$$\mathbf{v}_w^{t+1} = \mathbf{v}_w^* + \left( \frac{1}{\rho_w^*} \nabla p_w^{t+1} \right) \Delta t \quad (148)$$

where  $\mathbf{v}_w^{t+1}$  and  $p_w^{t+1}$  are the corrected water velocity and pressure at time  $(t + 1)$ , respectively. To complete this expression, one would need to estimate the water pressure  $p_w^{t+1}$  and this can be achieved by enforcing the incompressibility condition for the water phase, that is  $\nabla \cdot \mathbf{v}_w^{t+1} = 0$ . By substituting this condition to Equation (148), the following equation can be obtained:

$$\nabla \cdot \left( \frac{1}{\rho_w^*} \nabla p_w^{t+1} \right) = \frac{1}{\Delta t} \nabla \cdot \mathbf{v}_w^* \quad (149)$$

This equation is commonly known as the pressure Poisson's equation, whose source term is dependent on the divergence of temporal velocity ( $\mathbf{v}_w^*$ ). Furthermore, since the temporal velocity is also dependent on the water-solid relative velocity, as seen in Equation (146), the coupling effect of solid deformation on the pore-water pressure is automatically achieved through Equation (149). An alternative form of the pressure Poisson's equation can also be derived by calculating  $(\nabla \cdot \mathbf{v}_w^*)$

from Equation (147) and substituting this term back to Equation (149), giving:

$$\nabla \cdot \left( \frac{1}{\rho_w^*} \nabla p_w^{t+1} \right) = \frac{\rho_w^0 - \rho_w^*}{\rho_w^t \Delta t^2} - \frac{(1 - n_w)}{n_w \Delta t} \nabla \cdot \mathbf{v}_s + \frac{(\mathbf{v}_s - \mathbf{v}_w^*)}{n_w \Delta t} \nabla n_w \quad (150)$$

The readers should have immediately noticed that the source term of this pressure Poisson's equation now involves both solid-water relative velocity ( $\mathbf{v}_s - \mathbf{v}_w^*$ ) and the volumetric deformation of the solid matrix ( $\nabla \cdot \mathbf{v}_s$ ), both of which produce the coupling effect of solid deformation on the pore-water pressure of the water flow. Again, it is noted here that if the spatial variation of the porosity distribution is assumed to be very small and negligible (i.e.  $\nabla n_w = 0$ ), Equation (150) can be simplified to the following equation, which was previously reported in Bui and Nguyen (Bui and Nguyen, 2017):

$$\nabla \cdot \left( \frac{1}{\rho_w^*} \nabla p_w^{t+1} \right) = \frac{\rho_w^0 - \rho_w^*}{\rho_w^t \Delta t^2} - \frac{(1 - n_w)}{n_w \Delta t} \nabla \cdot \mathbf{v}_s \quad (151)$$

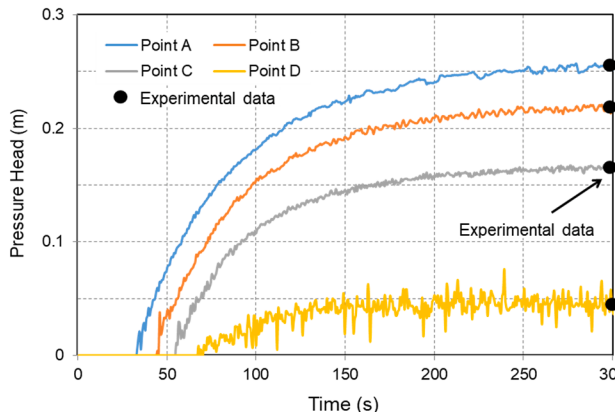
To solve the above pressure Poisson's equation using SPH, one needs to discretise this equation onto SPH particles using suitable SPH operators, as discussed in Section 2. The traditional SPH approach to solve this equation follows the incompressible SPH (ISPH) model proposed by Shao and Lo (Shao and Lo, 2003), in which the above pressure Poisson's equation was first converted into the SPH approximation equation. This results in a large sparse system of linear equations for the water pressure, which requires an effective solver to obtain the pore water pressure, and this is not a straightforward task for large-scale applications or problems involving a large number of SPH particles. A more straightforward and robust approach is to follow the method suggested by Bui and Nguyen (Bui and Nguyen, 2017), which can be dated back to the original works proposed in (Daly et al., 2016, Hosseini et al., 2007). In this approach, a fully explicit time integration scheme (E-ISPH) is adopted to solve the above pressure Poisson's equation. Accordingly, Equation (151) can be converted into the following equation for the pore-water pressure (Bui and Nguyen, 2017):

$$p_a^{t+1} = \frac{B_a + \sum_{b=1}^N A_{ab} p_b^t}{\sum_{j=1}^N A_{ab}} \quad (152)$$

where the subscripts  $a$  and  $b$  are used to indicate water particles, while the subscripts  $i$  and  $j$  indicate the solid particles;  $A_{ab}$  and  $B_a$  are computed as follows:

$$A_{ab} = \sum_{b \neq a}^N \frac{\bar{m}_b}{n_b} \frac{8}{(\rho_a^* + \rho_b^*)^2} \frac{\mathbf{r}_{ab} \cdot \nabla_a W_{ab}}{(\mathbf{r}_{ab}^2 + \eta^2)} \quad (153)$$

$$B_a = \frac{\rho_a^0 - \rho_a^*}{\rho_a^t \Delta t^2} + \frac{(1 - n_a)}{n_a \Delta t} \sum_{j=1}^M \frac{\bar{m}_j}{\bar{\rho}_j} (\mathbf{v}_{ia} - \mathbf{v}_{ja}) \cdot \nabla_a W_{ab} \quad (154)$$



At this point, we have completed the mathematical descriptions for the two-phases multi-layers SPH framework. It can be seen from these governing equations that information between the fluid and solid phases needs to be exchanged during the computational process. This can be achieved by adopting the coupled algorithm for the fluid–solid mixture proposed by Bui and Nguyen (Bui and Nguyen, 2017), which is outlined in Fig. 44. Furthermore, a special boundary treatment complied with the above predictor–corrector time integration scheme for the water phase is also required. The readers are referred to our previous work in (Bui and Nguyen, 2017) for further detailed descriptions of this boundary condition as well as the coupling procedure. The capability of the above two-phases multi-layers SPH framework was demonstrated in our previous work (Bui and Nguyen, 2017) and will be briefly summarised here. First, the computational model was applied to analyse the seepage flow through a rockfill dam, which was previously reported in (Larese, 2012). The geometry and boundary setting conditions of the rockfill dam is shown in Fig. 45a. The rockfill dam is 1 m high and 3.2 m wide, with both upstream and downstream slopes being 1.5:1.0. The properties of the rockfill material used to construct the embankment were detailed in (Larese, 2012). In the experiment, a constant water flow rate of  $Q = 24.46 \text{ L/s}$  was supplied on the upstream slope to achieve the steady-state seepage flow inside the rockfill embankment. Pressure sensors were installed at several locations on the embankment floor (i.e. Points A-D) to measure the pore-water pressure and thus the phreatic level inside the embankment. In the SPH simulations, the embankment is modelled by solid particles, which is modelled as a homogenous elastic material, while the water flow is modelled using the E-SPH model described above.

To properly account for the viscous resistance force produced by the rockfill material on the water flow, the following quadratic Darcy-Forchheimer's seepage force model (Bui and Nguyen, 2017) was adopted, instead of the seepage force presented in Equation (145), which is more suitable for sandy materials:

$$\mathbf{R}^{ws} = - \left( \frac{n_w \mu_w}{k} \mathbf{v}_{ws} + \frac{1.75}{\sqrt{150}} \frac{\rho_w n_w}{\sqrt{k} n_w^{3/2}} \mathbf{v}_{ws} |\mathbf{v}_{ws}| \right) + p_w \nabla n_w \quad (155)$$

where  $k$  is the water permeability coefficient, which can be estimated from the average diameter of granular materials and its porosity (Bui and Nguyen, 2017);  $\mathbf{v}_{ws}$  is the relative velocity between the water and solid phase; and  $|\mathbf{v}_{ws}|$  is the norm of the relative velocity. The readers are referred to our previous work in (Bui and Nguyen, 2017) for all detailed descriptions of these parameters, as well as other parameters and boundary treatments required for the SPH simulations.

It can be seen from Fig. 45 (b-d) that the current two-phases multi-layers SPH framework could simulate well the progressive development of seepage flow through the rockfill embankment. As the water flow enters the embankment, the seepage drag force starts to activate and

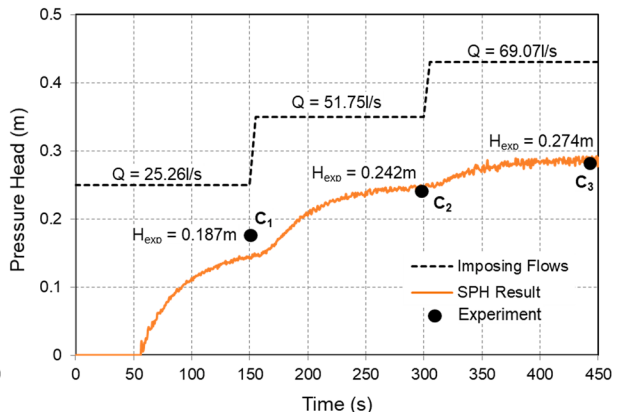


**Fig. 46.** Prediction of pressure head (or pore-water pressure) developments using the two-phases multi-layers SPH framework, after (Bui and Nguyen, 2017).

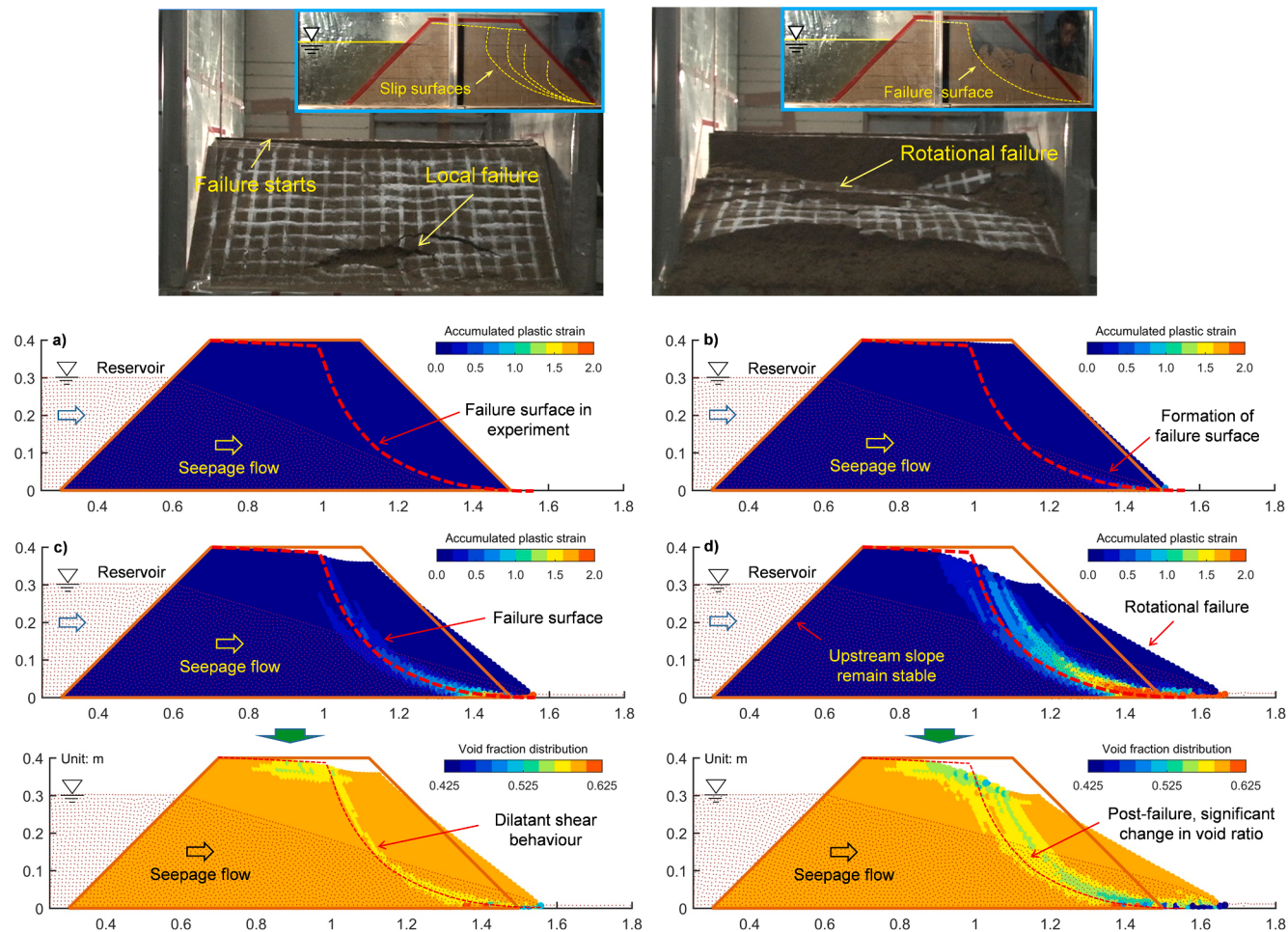


**Fig. 47.** Modelling of progressive failure of sandy embankment by the two-phases multi-layers SPH framework, after Bui and Nguyen (Bui and Nguyen, 2017).

slowdowns the water flow, causing a change in the water velocity and the pore-pressure gradient. The phreatic surface subsequently raises and remains unchanged when the water flow inside the embankment reaches its steady-state condition. The SPH model could capture well the steady-state phreatic surface of the seepage flow and the pore-water pressure measured in the experiment (Larese De Totto and Rossi, 2012), as shown in Fig. 45d and Fig. 46a. Furthermore, the current SPH model could capture a very smooth and stable pressure profile of the water flow for a very long physical time of testing (i.e. >300 s), which is not a straightforward task for many existing SPH codes. This suggests that the current SPH model is very stable and could be applied to investigate experiments involved long physical time. To further demonstrate the capability of the current SPH model, the above simulation was repeated with the transient incoming flow discharges, i.e.  $Q = 25.6 \text{ L/s}$ ,  $Q = 51.75 \text{ L/s}$  and  $Q = 69.07 \text{ L/s}$ . The pore-water pressure at a position of 2.7 m from the upstream slope toe on the embankment floor (i.e. Point C) was then measured and compared with the experiment (Larese De Totto and Rossi, 2012). The results are illustrated in Fig. 46b, showing a good agreement between the SPH simulation and experiment. This suggests that the current two-phases multi-layers SPH framework could capture well the development of seepage flow inside a saturated porous medium.

The final example to demonstrate the capability of the two-phases multi-layers SPH framework in capturing the complex coupled flow-deformation behaviour of geomaterials is shown in Fig. 47, which was previously reported in (Bui and Nguyen, 2017). In this demonstration, the above SPH framework was applied to simulate the seepage flow-induced sandy embankment failure experiment conducted by the authors. The readers are referred to our previous work in (Bui and Nguyen,

2017) for the detail descriptions of the experiment as well as the numerical setting and boundary conditions required for the SPH simulation. Here, the same SPH model used to analyse the rockfill dam experiment was adopted, except that the seepage force is now replaced by the standard seepage force form of Equation (145), which is more suitable for sandy materials. Furthermore, to describe the progressive failure process of the embankment, the embankment material is now modelled by an elastic-plastic constitutive model accounting for the strength reduction due to the seepage flow (Bui and Nguyen, 2017). As could be seen from Fig. 47 (a-d), the SPH model could capture the overall failure mechanism of the embankment and qualitatively predict the failure surface observed in the experiment. The coupled flow-deformation involving large deformation and post-failure response of embankment materials could be well simulated. Nevertheless, because of the relatively simple material constitutive model adopted in (Bui and Nguyen, 2017) and the lack of considering the unsaturated seepage flow and internal erosion process, the current SPH model failed to capture several key failure mechanisms observed from the experiment, including the local failure at the slope toe (or piping due to erosion) and progressive failure involving multiple failure surfaces. For this reason, further works are still required to provide the two-phases multi-layers SPH better capabilities to capture complex coupled flow-deformation problems, and these works will be reported in the near future.

## 5. Conclusions

In this paper, fundamentals and state-of-the-art applications of SPH have been presented with sufficient details covering a range of problems in geomechanics. A new and robust SPH approximation formulation for

the Laplacian, which involves the second-order derivatives of a field quantity, has been proposed and proven to outperform existing SPH formulations. Common misconceptions on the tensile instability and challenges inherent to the method (such as numerical accuracy, pairing instability and stress boundary conditions) have been addressed and solutions discussed to provide readers insights into SPH, in addition to the fundamentals and applications. Other issues that are not intrinsic to SPH, but are essential for the applications of the method have also been given attention. They include parallelisation to tackle field-scale applications and material constitutive models for SPH. The latter is central to geomechanics applications and provides the readers with a range of constitutive models suitable for different applications involving solid deformation, localised failure, fracturing and flow of both fluid and granular materials. Along this line, of interest is our recent developments of a double-scale approach to tackle material instability issues related to softening and localisation that is particularly suitable for SPH applications in geomechanics, thanks to the truly meshfree nature of the method. The presented examples provide a wide spectrum of problems in geomechanics, illustrating great capacity, versatility and potential of the method for geomechanics applications.

## CRediT authorship contribution statement

**Ha H. Bui:** Conceptualization, Methodology, Software, Data curation, Visualization, Investigation, Validation, Resources, Funding acquisition, Project administration. **Giang D. Nguyen:** Conceptualization, Methodology, Software, Data curation, Visualization, Investigation, Validation, Resources, Funding acquisition, Project administration.

## Declaration of Competing Interest

The authors declare that they have no known competing financial interests or personal relationships that could have appeared to influence the work reported in this paper.

## Acknowledgements

The authors gratefully acknowledge support from the Australian Research Council via Discovery Projects DP170103793 (Nguyen & Bui) and DP190102779 (Bui & Nguyen), Future Fellowships FT200100884 (Bui) and FT140100408 (Nguyen). Contributions from Yanjian Lian and other postgraduate students at MCG Lab to this review are also acknowledged. Part of this research was undertaken with the assistance of resources and services from the National Computational Infrastructure (NCI), which is supported by the Australian Government.

## References

- Bažant, Z.P., 1991. Why continuum damage is nonlocal: micromechanics arguments. *J. Eng. Mech.* 117 (5), 1070–1087.
- Benz, W., 1990. Smooth particle hydrodynamics: a review. The numerical modelling of nonlinear stellar pulsations 269–288.
- Beuth, L., Więckowski, Z., Vermeer, P., 2011. Solution of quasi-static large-strain problems by the material point method. *Int. J. Numer. Anal. Meth. Geomech.* 35 (13), 1451–1465.
- Blanc, T., Pastor, M., 2012. A stabilized Fractional Step, Runge-Kutta Taylor SPH algorithm for coupled problems in geomechanics. *Comput. Methods Appl. Mech. Eng.* 221, 41–53.
- Blanc, T., Pastor, M., 2013. A stabilized Smoothed Particle Hydrodynamics, Taylor-Galerkin algorithm for soil dynamics problems. *Int. J. Numer. Anal. Meth. Geomech.* 37 (1), 1–30.
- Bolton, M.D., 1986. Strength and dilatancy of sands. *Géotechnique* 36 (1), 65–78.
- Borja, R.I., 2013. Plasticity: Modeling & Computation. Springer Science & Business Media.
- Borst, R.D., Pamin, J., 1996. Gradient plasticity in numerical simulation of concrete cracking. *Eur. J. Mech. A. Solids* 15 (2), 295–320.
- Brookshaw, L., 1985. A method of calculating radiative heat diffusion in particle simulations. In: Proceedings of the Astronomical society of Australia, vol. 6, pp. 207–210.
- Bui, H., Nguyen, G.D., 2020. Numerical predictions of post-flow behaviour of granular materials using an improved SPH model. In: CIGOS 2019, Innovation for Sustainable Infrastructure. Springer, pp. 895–900.
- Bui, H.H., 2007. Lagrangian mesh-free particle method (SPH) for large deformation and post-failure of geomaterial using elasto-plastic constitutive models.  $\square\square\square\square\square$ .
- Bui, H.H., Fukagawa, R., 2005. Smoothed Particle Hydrodynamics (SPH) for Soil Mechanics: treatment of frictional boundary condition. *Japanese Terramech.* 25, 50–57.
- Bui, H.H., Fukagawa, R., 2009. A first attempt to solve soil-water coupled problem by SPH. *Japanese Terramech.* 29, 33–38.
- Bui, H.H., Fukagawa, R., 2013. An improved SPH method for saturated soils and its application to investigate the mechanisms of embankment failure: case of hydrostatic pore-water pressure. *Int. J. Numer. Anal. Meth. Geomech.* 37 (1), 31–50.
- Bui, H.H., Fukagawa, R., Sako, K., 2006. Smoothed particle hydrodynamics for soil mechanics. In: Proceedings of the 6th European Conference on Numerical Methods in Geotechnical Engineering - Numerical Methods in Geotechnical Engineering, pp. 278–281.
- Bui, H.H., Fukagawa, R., Sako, K., Ohno, S., 2008a. Lagrangian meshfree particles method (SPH) for large deformation and failure flows of geomaterial using elasto-plastic soil constitutive model. *Int. J. Numer. Anal. Meth. Geomech.* 32 (12), 1537–1570.
- Bui, H.H., Fukagawa, R., Sako, K., Wells, J.C., 2009. Numerical simulation of granular materials based on smoothed particle hydrodynamics (SPH). In: AIP Conference Proceedings. American Institute of Physics, vol. 1145, pp. 575–578.
- Bui, H.H., Fukagawa, R., Sako, K., Wells, J.C., 2011. Slope stability analysis and discontinuous slope failure simulation by elasto-plastic smoothed particle hydrodynamics (SPH). *Geotechnique* 61 (7), 565–574.
- Bui, H.H., Khoa, H.D.V., 2011. Bearing capacity of shallow foundation by Smoothed Particle Hydrodynamics (SPH) analysis. In: Computational Geomechanics, COMGEO II - Proceedings of the 2nd International Symposium on Computational Geomechanics, pp. 457–468.
- Bui, H.H., Kodikara, J.K., Bouazza, A., Haque, A., Ranjith, P.G., 2014. A novel computational approach for large deformation and post-failure analyses of segmented retaining wall systems. *Int. J. Numer. Anal. Meth. Geomech.* 38 (13), 1321–1340.
- Bui, H.H., Nguyen, G.D., 2017. A coupled fluid-solid SPH approach to modelling flow through deformable porous media. *Int. J. Solids Struct.* 125, 244–264.
- Bui, H.H., Nguyen, G.D., Kodikara, J., Sanchez, M., 2015. Soil cracking modelling using the mesh-free SPH method. arXiv preprint arXiv:1503.01172.
- Bui, H.H., Sako, K., Fukagawa, R., 2005. Numerical simulation of soil-water interaction using smoothed particle hydrodynamics (SPH) method. In: 15th International Conference of the International Society for Terrain Vehicle Systems 2005, ISTVS 2005, pp. 126–140.
- Bui, H.H., Sako, K., Fukagawa, R., 2006b. Non-cohesive material flows in rotating drum: Smoothed Particle Hydrodynamics (SPH) and Discrete Element Method (DEM). In: Proceedings of The 41st Japan National Conference on Geotechnical Engineering (JGS). JGS vol. 41, pp. 1–2.
- Bui, H.H., Sako, K., Fukagawa, R., 2007. Numerical simulation of soil-water interaction using smoothed particle hydrodynamics (SPH) method. *J. Terramech.* 44 (5), 339–346.
- Bui, H.H., Sako, K., Fukagawa, R., Wells, J., 2008c. SPH-based numerical simulations for large deformation of geomaterial considering soil-structure interaction. In: The 12th International Conference of International Association for Computer Methods and Advances in Geomechanics (IACMAG)., vol. 1, pp. 570–578.
- Cedolin, L., Bazant, Z.P., 1980. Effect of finite element choice in blunt crack band analysis. *Comput. Methods Appl. Mech. Eng.* 24 (3), 305–316.
- Chen, D., Huang, W., Lyamin, A., 2020. Finite particle method for static deformation problems solved using JFNK method. *Comput. Geotech.* 122, 103502.
- Chen, J., Beraun, J., 2000. A generalized smoothed particle hydrodynamics method for nonlinear dynamic problems. *Comput. Methods Appl. Mech. Eng.* 190 (1–2), 225–239.
- Chen, J.K., Beraun, J.E., Carney, T.C., 1999. A corrective smoothed particle method for boundary value problems in heat conduction. *Int. J. Numer. Meth. Eng.* 46 (2), 231–252.
- Chen, W., Qiu, T., 2012. Numerical simulations for large deformation of granular materials using smoothed particle hydrodynamics method. *Int. J. Geomech.* 12 (2), 127–135.
- Chen, Z., Schreyer, H.L., 1987. Simulation of soil-concrete interfaces with nonlocal constitutive models. *J. Eng. Mech.* 113 (11), 1665–1677.
- Crook, A., Willson, S., Yu, J., Owen, D., 2006. Predictive modelling of structure evolution in sandbox experiments. *J. Struct. Geol.* 28 (5), 729–744.
- Cuomo, S., Prime, N., Iannone, A., Dufour, F., Cascini, L., Darve, F., 2013. Large deformation FEMLIP drained analysis of a vertical cut. *Acta Geotech.* 8 (2), 125–136.
- Dafalias, Y.F., Manzari, M.T., 2004. Simple plasticity sand model accounting for fabric change effects. *J. Eng. Mech.* 130 (6), 622–634.
- Daly, E., Grimaldi, S., Bui, H.H., 2016. Explicit incompressible SPH algorithm for free-surface flow modelling: a comparison with weakly compressible schemes. *Adv. Water Resour.* 97, 156–167.
- De Borst, R., Crisfield, M.A., Remmers, J.J., Verhoosel, C.V., 2012. Nonlinear Finite Element Analysis of Solids and Structures. John Wiley & Sons.
- Dehnen, W., Aly, H., 2012. Improving convergence in smoothed particle hydrodynamics simulations without pairing instability. *MNRAS* 425 (2), 1068–1082.
- Dey, R., Hawlader, B., Phillips, R., Soga, K., 2016. Numerical modeling of combined effects of upward and downward propagation of shear bands on stability of slopes with sensitive clay. *Int. J. Numer. Anal. Meth. Geomech.* 40 (15), 2076–2099.

- Douillet-Grellier, T., Jones, B.D., Pramanik, R., Pan, K., Albaiz, A., Williams, J.R., 2016. Mixed-mode fracture modeling with smoothed particle hydrodynamics. *Comput. Geotech.* 79, 73–85.
- Dyka, C., Randles, P., Ingel, R., 1997. Stress points for tension instability in SPH. *Int. J. Numer. Meth. Eng.* 40 (13), 2325–2341.
- Fávero Neto, A.H., Borja, R.I., 2018. Continuum hydrodynamics of dry granular flows employing multiplicative elastoplasticity. *Acta Geotech.* 13 (5), 1027–1040.
- Gingold, R.A., Monaghan, J.J., 1977. Smoothed Particle Hydrodynamics - Theory and Application to Non-Spherical Stars. *MNRAS* 181 (2), 375–389.
- Gray, J.P., Monaghan, J.J., Swift, R.P., 2001. SPH elastic dynamics. *Comput. Methods Appl. Mech. Eng.* 190 (49–50), 6641–6662.
- Gui, Y., Zhao, Z., Kodikara, J., Bui, H.H., Yang, S.Q., 2016. Numerical modelling of laboratory soil desiccation cracking using UDEC with a mix-mode cohesive fracture model. *Eng. Geol.* 202, 14–23.
- Hernquist, L., Katz, N., 1989. TREESPH-A unification of SPH with the hierarchical tree method. *Astrophys. J. Suppl. Ser.* 70, 419–446.
- Hiraoka, N., Oya, A., Bui, H.H., Rajeev, P., Fukagawa, R., 2013. Seismic slope failure modelling using the mesh-free SPH method. *Int. J. Geomate* 5 (1), 660–665.
- Hobbs, D., 1965. An assessment of a technique for determining the tensile strength of rock. *Br. J. Appl. Phys.* 16 (2), 259.
- Hosseini, S., Manzari, M., Hannani, S., 2007. A fully explicit three-step SPH algorithm for simulation of non-Newtonian fluid flow. *Int. J. Numer. Meth. Heat Fluid Flow*.
- Hu, X.Y., Adams, N.A., 2006. A multi-phase SPH method for macroscopic and mesoscopic flows. *J. Comput. Phys.* 213 (2), 844–861.
- Hu, X.Y., Adams, N.A., 2007. An incompressible multi-phase SPH method. *J. Comput. Phys.* 227 (1), 264–278.
- Hurley, R.C., Andrade, J.E., 2017. Continuum modeling of rate-dependent granular flows in SPH. *Comput. Part. Mech.* 4 (1), 119–130.
- Jefferies, M., 1993. Nor-Sand: a simple critical state model for sand. *Geotechnique* 43 (1), 91–103.
- Jin, Y.-F., Wu, Z.-X., Yin, Z.-Y., Shen, J.S., 2017. Estimation of critical state-related formula in advanced constitutive modeling of granular material. *Acta Geotech.* 12 (6), 1329–1351.
- Jin, Y.-F., Yin, Z.-Y., Yuan, W.-H., 2020. Simulating retrogressive slope failure using two different smoothed particle finite element methods: a comparative study. *Eng. Geol.* 279, 105870.
- Jop, P., Forterre, Y., Pouliquen, O., 2006a. A constitutive law for dense granular flows. *Nature* 441, 727.
- Jop, P., Forterre, Y., Pouliquen, O., 2006b. A constitutive law for dense granular flows. *Nature* 441 (7094), 727–730.
- Koshizuka, S., Oka, Y., 1996. Moving-particle semi-implicit method for fragmentation of incompressible fluid. *Nucl. Sci. Eng.* 123 (3), 421–434.
- Larese, A., 2012. A coupled Eulerian-PFEM model for the simulation of overtopping in rockfill dams. UPC BarcelonaTech, Barcelona, Spain, vol. Ph.D., pp. 258.
- Larese De Tettis, A., Rossi, R., 2012. A coupled Eulerian-PFEM model for the simulation of overtopping in rockfill dams. Centre Internacional de Mètodes Numèrics en Enginyeria (CIMNE).
- Le, L.A., Nguyen, G.D., Bui, H.H., Andrade, J.E., 2020. Localised failure of geomaterials: how to extract localisation band behaviour from macro test data. *Geotechnique* 1–52.
- Le, L.A., Nguyen, G.D., Bui, H.H., Sheikh, A.H., Kotousov, A., 2018. Localised failure mechanism as the basis for constitutive modelling of geomaterials. *Int. J. Eng. Sci.* 133, 284–310.
- Le, L.A., Nguyen, G.D., Bui, H.H., Sheikh, A.H., Kotousov, A., 2019. Incorporation of micro-cracking and fibre bridging mechanisms in constitutive modelling of fibre reinforced concrete. *J. Mech. Phys. Solids* 133, 103732.
- Le, L.A., Nguyen, G.D., Bui, H.H., Sheikh, A.H., Kotousov, A., Khanna, A., 2017. Modelling jointed rock mass as a continuum with an embedded cohesive-frictional model. *Eng. Geol.* 228, 107–120.
- Li, D.-Y., Tao, W., Cheng, T.-J., Sun, X.-L., 2016. Static and dynamic tensile failure characteristics of rock based on splitting test of circular ring. *Trans. Nonferr. Met. Soc. China* 26 (7), 1912–1918.
- Liberky, L., Petschek, A.G., 1991. Smooth particle hydrodynamics with strength of materials. In: Trease, H., Fritts, M., Crowley, W.P. (Eds.), *Advances in the Free-Lagrange Method Including Contributions on Adaptive Gridding and the Smooth Particle Hydrodynamics Method*, vol. 395. Springer Berlin Heidelberg, pp. 248–257.
- Liberky, L.D., Petschek, A.G., Carney, T.C., Hipp, J.R., Allahdadi, F.A., 1993. High-Strain Lagrangian Hydrodynamics - a 3-Dimensional Sph Code for Dynamic Material Response. *J. Comput. Phys.* 109 (1), 67–75.
- Liu, M., Liu, G., 2010. Smoothed particle hydrodynamics (SPH): an overview and recent developments. *Arch. Comput. Methods Eng.* 17 (1), 25–76.
- Liu, M., Xie, W., Liu, G., 2005. Modeling incompressible flows using a finite particle method. *Appl. Math. Model.* 29 (12), 1252–1270.
- Locat, A., Leroueil, S., Bernander, S., Demers, D., Jostad, H.P., Ouehb, L., 2011. Progressive failures in eastern Canadian and Scandinavian sensitive clays. *Can. Geotech. J.* 48 (11), 1696–1712.
- Lube, G., Huppert, H.E., Sparks, R.S.J., Hallworth, M.A., 2004. Axisymmetric collapses of granular columns. *J. Fluid Mech.* 508, 175.
- Lucy, L.B., 1977. Numerical approach to testing of fission hypothesis. *Astron. J.* 82 (12), 1013–1024.
- Maeda, K., Sakai, H., Sakai, M., 2006. Development of seepage failure analysis method of ground with smoothed particle hydrodynamics. *Struct. Eng./Earthquake Eng.* 23 (2), 307s–319s.
- Minatti, L., Paris, E., 2015. A SPH model for the simulation of free surface granular flows in a dense regime. *Appl. Math. Model.* 39 (1), 363–382.
- Monaghan, J.J., 1992. Smoothed particle hydrodynamics. *Ann. Rev. Astron. Astrophys.* 30 (1), 543–574.
- Monaghan, J.J., 1994. Simulating Free-Surface Flows with Sph. *J. Comput. Phys.* 110 (2), 399–406.
- Monaghan, J.J., 2000. SPH without a tensile instability. *J. Comput. Phys.* 159 (2), 290–311.
- Monaghan, J.J., 2005a. Smoothed particle hydrodynamics. *Rep. Prog. Phys.* 68 (8), 1703–1759.
- Monaghan, J.J., 2005b. Theory and applications of smoothed particle hydrodynamics. *Front. Numeric. Anal.* 143–194.
- Monaghan, J.J., 2012. Smoothed particle hydrodynamics and its diverse applications. *Annu. Rev. Fluid Mech.* 44 (44), 323–346.
- Monaghan, J.J., Gingold, R.A., 1983. Shock simulation by the particle method Sph. *J. Comput. Phys.* 52 (2), 374–389.
- Monaghan, J.J., Kos, A., Issa, N., 2003. Fluid motion generated by impact. *J. Waterway Port Coastal Ocean Eng.-Asce* 129 (6), 250–259.
- Monaghan, J.J., Lattanzio, J.C., 1991. A simulation of the collapse and fragmentation of cooling molecular clouds. *Astrophys. J.* 375 (1), 177–189.
- Monaghan, J.J., Price, D.J., 2001. Variational principles for relativistic smoothed particle hydrodynamics. *MNRAS* 328 (2), 381–392.
- Monforte, L., Arroyo, M., Carbonell, J.M., Gens, A., 2017. Numerical simulation of undrained insertion problems in geotechnical engineering with the particle finite element method (PFEM). *Comput. Geotech.* 82, 144–156.
- Moresi, L., Dufour, F., Mühlhaus, H.-B., 2003. A Lagrangian integration point finite element method for large deformation modeling of viscoelastic geomaterials. *J. Comput. Phys.* 184 (2), 476–497.
- Morris, J.P., Fox, P.J., Zhu, Y., 1997. Modeling low Reynolds number incompressible flows using SPH. *J. Comput. Phys.* 136 (1), 214–226.
- Nazem, M., Carter, J.P., Airey, D.W., 2009. Arbitrary Lagrangian-Eulerian method for dynamic analysis of geotechnical problems. *Comput. Geotech.* 36 (4), 549–557.
- Neilsen, M., Schreyer, H., 1993. Bifurcations in elastic-plastic materials. *Int. J. Solids Struct.* 30 (4), 521–544.
- Neto, A.H.F., Borja, R.I., 2018. Continuum hydrodynamics of dry granular flows employing multiplicative elastoplasticity. *Acta Geotech.* 13 (5), 1027–1040.
- Nguyen, C.T., Bui, H.H., Fukagawa, R., 2013. Two-dimensional numerical modelling of modular-block soil retaining walls collapse using meshfree method. *Int. J. Geomate*. 5 (1), 647–652.
- Nguyen, C.T., Bui, H.H., Fukagawa, R., 2015. Failure mechanism of true 2D granular flows. *J. Chem. Eng. Jpn.* 48 (6), 395–402.
- Nguyen, C.T., Nguyen, C.T., Bui, H.H., Nguyen, G.D., Fukagawa, R., 2017a. A new SPH-based approach to simulation of granular flows using viscous damping and stress regularisation. *Landslides* 14 (1), 69–81.
- Nguyen, C.T., Nguyen, G.D., Das, A., Bui, H.H., 2017b. Constitutive modelling of progressive localised failure in porous sandstones under shearing at high confining pressures. *Int. J. Rock Mech. Min. Sci.* 93, 179–195.
- Nguyen, G.D., 2014. An enriched constitutive model for fracture propagation analysis using the material point method. *Appl. Mech. Mater. Trans Tech Publ* 553, 731–736.
- Nguyen, G.D., Bui, H.H., 2020. A thermodynamics- and mechanism-based framework for constitutive models with evolving thickness of localisation band. *Int. J. Solids Struct.* 187, 100–120.
- Nguyen, G.D., Einav, I., Korsunsky, A.M., 2012. How to connect two scales of behaviour in constitutive modelling of geomaterials. *Geotech. Lett.* 2, 129–134.
- Nguyen, G.D., Housby, G.T., 2008. A coupled damage–plasticity model for concrete based on thermodynamic principles: Part I: model formulation and parameter identification. *Int. J. Numer. Anal. Meth. Geomech.* 32 (4), 353–389.
- Nguyen, G.D., Korsunsky, A.M., Einav, I., 2014. A constitutive modelling framework featuring two scales of behaviour: fundamentals and applications to quasi-brittle failure. *Eng. Fract. Mech.* 115, 221–240.
- Nguyen, G.D., Nguyen, C.T., Nguyen, V.P., Bui, H.H., Shen, L., 2016. A size-dependent constitutive modelling framework for localised failure analysis. *Comput. Mech.* 58 (2), 257–280.
- Nguyen, N.H., Bui, H.H., Nguyen, G.D., 2020. Effects of material properties on the mobility of granular flow. *Granular Matter* 22, 1–17.
- Nonoyama, H., Moriguchi, S., Sawada, K., Yashima, A., 2015. Slope stability analysis using smoothed particle hydrodynamics (SPH) method. *Soils Found.* 55 (2), 458–470.
- Oger, G., Le Touzé, D., Guibert, D., De Leffe, M., Biddiscombe, J., Soumagne, J., Piccinni, J.-G., 2016. On distributed memory MPI-based parallelization of SPH codes in massive HPC context. *Comput. Phys. Commun.* 200, 1–14.
- Onate, E., Idelsohn, S.R., Celigueta, M.A., Rossi, R., 2008. Advances in the particle finite element method for the analysis of fluid–multibody interaction and bed erosion in free surface flows. *Comput. Methods Appl. Mech. Eng.* 197 (19–20), 1777–1800.
- Pastor, M., Haddad, B., Sorbino, G., Cuomo, S., Drempetic, V., 2009. A depth-integrated, coupled SPH model for flow-like landslides and related phenomena. *Int. J. Numer. Anal. Meth. Geomech.* 33 (2), 143–172.
- Peng, C., Wu, W., Yu, H.-S., Wang, C., 2015. A SPH approach for large deformation analysis with hypoplastic constitutive model. *Acta Geotech.* 10 (6), 703–717.
- Pietruszczak, S., 2010. Fundamentals of plasticity in geomechanics. Crc Press, Boca Raton, FL.
- Pijaudier-Cabot, G., Bažant, Z.P., 1987. Nonlocal damage theory. *J. Eng. Mech.* 113 (10), 1512–1533.
- Price, D.J., 2012. Smoothed particle hydrodynamics and magnetohydrodynamics. *J. Comput. Phys.* 231 (3), 759–794.
- Qiu, G., Henke, S., Grabe, J., 2011. Application of a Coupled Eulerian-Lagrangian approach on geomechanical problems involving large deformations. *Comput. Geotech.* 38 (1), 30–39.

- Randles, P.W., Carney, T.C., Libersky, L.D., Renick, J.D., Petschek, A.G., 1995. Calculation of oblique impact and fracture of tungsten cubes using smoothed particle hydrodynamics. *Int. J. Impact Eng.* 17 (4–6), 661–672.
- Randles, P.W., Libersky, L.D., 1996. Smoothed particle hydrodynamics: Some recent improvements and applications. *Comput. Methods Appl. Mech. Eng.* 139 (1–4), 375–408.
- Randles, P.W., Libersky, L.D., 2007. Normalized SPH with stress points. *Int. J. Numer. Meth. Eng.* 48 (10), 1445.
- Rodríguez, R., Sanchez, M., Ledesma, A., Lloret, A., 2007. Experimental and numerical analysis of desiccation of a mining waste. *Can. Geotech. J.* 44 (6), 644–658.
- Sánchez, M., Manzoli, O.L., Guimaraes, L.J., 2014. Modeling 3-D desiccation soil crack networks using a mesh fragmentation technique. *Comput. Geotech.* 62, 27–39.
- Shao, S.D., Lo, E.Y.M., 2003. Incompressible SPH method for simulating Newtonian and non-Newtonian flows with a free surface. *Adv. Water Resour.* 26 (7), 787–800.
- Sheikh, B., Qiu, T., Ahmadipur, A., 2020. Comparison of SPH boundary approaches in simulating frictional soil–structure interaction. *Acta Geotech.* 1–20.
- Silling, S.A., 2000. Reformulation of elasticity theory for discontinuities and long-range forces. *J. Mech. Phys. Solids* 48 (1), 175–209.
- Sima, J., Jiang, M., Zhou, C., 2014. Numerical simulation of desiccation cracking in a thin clay layer using 3D discrete element modeling. *Comput. Geotech.* 56, 168–180.
- Simo, J.C., Hughes, T.J., 2006. Computational Inelasticity. Springer Science & Business Media.
- Soga, K., Alonso, E., Yerro, A., Kumar, K., Bandara, S., 2016. Trends in large-deformation analysis of landslide mass movements with particular emphasis on the material point method. *Geotechnique* 66 (3), 248–273.
- Sulsky, D., Chen, Z., Schreyer, H.L., 1994. A particle method for history-dependent materials. *Comput. Methods Appl. Mech. Eng.* 118 (1–2), 179–196.
- Swegle, J., Hicks, D., Attaway, S., 1995. Smoothed particle hydrodynamics stability analysis. *J. Comput. Phys.* 116 (1), 123–134.
- Takeda, H., Miyama, S.M., Sekiya, M., 1994. Numerical simulation of viscous-flow by smoothed particle hydrodynamics. *Prog. Theoret. Phys.* 92 (5), 939–960.
- Tran, H.T., Bui, H.H., Nguyen, G.D., Kodikara, J., Sanchez, M., 2017. A continuum based approach to modelling tensile cracks in soils. *Poromechanics VI*. 337–344.
- Tran, H.T., Wang, Y., Nguyen, G.D., Kodikara, J., Sanchez, M., Bui, H.H., 2019. Modelling 3D desiccation cracking in clayey soils using a size-dependent SPH computational approach. *Comput. Geotech.* 116, 103209.
- Tran, K.M., Bui, H.H., Kodikara, J., Sánchez, M., 2020. Soil curling process and its influencing factors. *Can. Geotech. J.* 57 (3), 408–422.
- Tran, T.-H., 2019. A coupled hydro-mechanical SPH framework to model desiccation cracking in clay soils. PhD Thesis. Monash University.
- Valdez-Balderas, D., Domínguez, J.M., Rogers, B.D., Crespo, A.J., 2013. Towards accelerating smoothed particle hydrodynamics simulations for free-surface flows on multi-GPU clusters. *J. Parallel Distrib. Comput.* 73 (11), 1483–1493.
- Vardoulakis, I., Aifantis, E.C., 1991. A gradient flow theory of plasticity for granular materials. *Acta Mech.* 87 (3), 197–217.
- Vidal, Y., Bonet, J., Huerta, A., 2007. Stabilized updated Lagrangian corrected SPH for explicit dynamic problems. *Int. J. Numer. Meth. Eng.* 69 (13), 2687–2710.
- Vignjevic, R., Reveles, J.R., Campbell, J., 2006. SPH in a total Lagrangian formalism.
- Wang, B., Vardon, P., Hicks, M., 2016a. Investigation of retrogressive and progressive slope failure mechanisms using the material point method. *Comput. Geotech.* 78, 88–98.
- Wang, B., Vardon, P.J., Hicks, M.A., Chen, Z., 2016b. Development of an implicit material point method for geotechnical applications. *Comput. Geotech.* 71, 159–167.
- Wang, J., Chan, D., 2014. Frictional contact algorithms in SPH for the simulation of soil–structure interaction. *Int. J. Numer. Anal. Meth. Geomech.* 38 (7), 747–770.
- Wang, Y. Modelling rock fractures using SPH with an embedded fracture process zone. PhD Thesis, Monash University.
- Wang, Y., Bui, H.H., Nguyen, G.D., Ranjith, P., 2017. A mesh-free continuum based computational approach to modelling rock fracture. *Poromechanics VI*. 2041–2048.
- Wang, Y., Bui, H.H., Nguyen, G.D., Ranjith, P., 2019. A new SPH-based continuum framework with an embedded fracture process zone for modelling rock fracture. *Int. J. Solids Struct.* 159, 40–57.
- Wang, Y., Tran, H.T., Nguyen, G.D., Ranjith, P.G., Bui, H.H., 2020. Simulation of mixed-mode fracture using SPH particles with an embedded fracture process zone. *Int. J. Numer. Anal. Meth. Geomech.* 40 (10), 1417–1445.
- Xu, X., Deng, X.-L., 2016. An improved weakly compressible SPH method for simulating free surface flows of viscous and viscoelastic fluids. *Comput. Phys. Commun.* 201, 43–62.
- Yang, E., Bui, H.H., De Sterck, H., Nguyen, G.D., Bouazza, A., 2020a. A scalable parallel computing SPH framework for predictions of geophysical granular flows. *Comput. Geotech.* 121, 103474.
- Yang, E., Bui, H.H., Nguyen, G.D., Choi, C.E., Ng, C.W., De Sterck, H., Bouazza, A., 2021. Numerical investigation of the mechanism of granular flow impact on rigid control structures. *Acta Geotech.* 1–23.
- Yang, Z., Yang, S.-Q., Chen, M., 2020b. Peridynamic simulation on fracture mechanical behavior of granite containing a single fissure after thermal cycling treatment. *Comput. Geotech.* 120, 103414.
- Yu, L., Liu, J., Kong, X., Hu, Y., 2008. Three-dimensional RITSS large displacement finite element method for penetration of foundations into soil. *Comput. Geotech.* 35 (3), 372–382.
- Zabala, F., Alonso, E., 2011. Progressive failure of Aznalcóllar dam using the material point method. *Geotechnique* 61 (9), 795–808.
- Zhan, L., Peng, C., Zhang, B., Wu, W., 2019. Three-dimensional modeling of granular flow impact on rigid and deformable structures. *Comput. Geotech.* 112, 257–271.
- Zhan, L., Peng, C., Zhang, B., Wu, W., 2020. A SPH framework for dynamic interaction between soil and rigid body system with hybrid contact method. *Int. J. Numer. Anal. Meth. Geomech.* 44 (10), 1446–1471.
- Zhang, X., Krabbenhoft, K., Pedroso, D., Lyamin, A., Sheng, D., Da Silva, M.V., Wang, D., 2013. Particle finite element analysis of large deformation and granular flow problems. *Comput. Geotech.* 54, 133–142.
- Zhang, X., Sloan, S.W., Onate, E., 2018. Dynamic modelling of retrogressive landslides with emphasis on the role of clay sensitivity. *Int. J. Numer. Anal. Meth. Geomech.* 42 (15), 1806–1822.
- Zhao, S., Bui, H.H., Lemial, V., Nguyen, G.D., 2017. SPH simulation of strain localisation in geomaterials using a visco-plastic constitutive model. In: *Poromechanics VI*.
- Zhao, S., Bui, H.H., Lemiale, V., Nguyen, G.D., Darve, F., 2019. A generic approach to modelling flexible confined boundary conditions in SPH and its application. *Int. J. Numer. Anal. Meth. Geomech.* 43 (5), 1005–1031.
- Zhu, F., Zhao, J., 2021. Peridynamic modelling of blasting induced rock fractures. *J. Mech. Phys. Solids* 104469.